ABSTRACT

A Low-Cost Embedded Network Analyzer for the Measurement of Material Properties

Brandon J. Herrera, Ph.D.

Mentor: B. Randall Jean, Ph.D.

Many industrial processes involve the production of complex composite mixtures of multiple constituents that must be combined according to carefully controlled ratios. Inaccuracies in the control of the production processes can lead to out-of-specification mixtures with large variation in quality and properties and possibly an unusable end product. There is a persistent need for a measurement methodology and corresponding practical implementation that is sensitive to the changing constituent ratios having high accuracy and precision that can be used to provide the feedback information required for robust process control. However, the ratios of the individual components in some mixtures can be difficult to measure non-destructively with good accuracy and precision in a real-time, in-line industrial environment. Electromagnetic sensors that provide interrogation of the mixtures over the microwave frequency range have been put forward as a technology class that can meet the in-situ instrumentation requirements for a broad class of scientific and industrial applications. Vector Network Analyzers conveniently make these types of measurements in the scientific laboratory, but their costs are economically prohibitive for industrial applications. To lower instrument costs to a

viable price point, a time domain system called a Pulse Dispersion Network Analyzer has been developed for embedded industrial process control of material properties. Several industrial applications are also presented.

A Low-Cost Embedded Network Analyzer for the Measurement of Material Properties

by

Brandon J. Herrera, B.S.E.C.E., M.S.E.C.E.

A Dissertation

Approved by the Department of Electrical and Computer Engineering

_____
Kwang Y. Lee, Ph.D., Chairperson

Submitted to the Graduate Faculty of
Baylor University in Partial Fulfillment of the
Requirements for the Degree
of

Doctor of Philosophy

Approved by the Dissertation Committee:

_____
B. Randall Jean, Ph.D., Chairperson

_____
Charles Baylis, Ph.D.

_____
Yang Li, Ph.D.

_____
Robert Marks, Ph.D.

_____
Stephen McClain, Ph.D.

Accepted by the Graduate School
May 2015

_____
J. Larry Lyon, Ph.D., Dean

Page bearing signatures is kept on file in the Graduate School.

TABLE OF CONTENTS

LIST OF FIGURES

LIST OF TABLES

LIST OF ABBREVIATIONS

80/20 – Eighty percent to twenty percent

AC – Alternating Current

ADC – Analog to digital converter

ADS – Advanced Design System

API – Application Program Interface

ASIC – Application Specific Integrated Circuit

BJT – Bipolar Junction Transistor

BOM – Bill of Materials

CAD – Computer Aided Design

CDC – Communications Device Class

CSV – Comma-separated values

DAC – Digital to analog converter

DC – Direct Current

DDS – Direct Digital Synthesis

DFT – Discrete Fourier Transform

DLL – Dynamic-Link Library

DMA – Direct Memory Access

DSA – Digitally Stepped Attenuator

DSP – Digital Signal Processing

ECL – Emitter-Coupled Logic

ETF – Extended Time Factor

ETS – Equivalent Time Sampling

FFT – Fast Fourier Transform

GCC – GNU Compiler Collection

GMS – Guided Microwave Spectrometry

GPIO – General Purpose Input Output

GUI – Graphical User Interface

HART – Highway Addressable Remote Transducer

I^2C – Inter-Integrated Circuit

IC – Integrated Circuit

IF – Intermediate Frequency

LF – Low Frequency

LNA – Low Noise Amplifier

MCR – MATLAB Compiler Runtime

MPU – Microprocessor Unit

MUT – Material Under Test

OPP – Operational Performance Point

PCB – Printed Circuit Board

PCU-ICSS – Programmable Real-Time Unit and Industrial Communication Subsystem

PDNA – Pulse Dispersion Network Analyzer

Pot – Potentiometer

PLL – Phase-Locked Loop

PMIC – Power Management Integrated Circuit

PTH – Plated Through Hole

RAM – Random Access Memory

RF – Radio Frequency

ROM – Read Only Memory

SATA – Serial ATA

SD – Secure Digital

SiGe – Silicon Germanium

SIMD – Single Instruction Multiple Data

SMA – Subminiature version A

SMT – Surface Mount Technology

SNA – Scalar Network Analyzer

SNR – Signal-to-Noise Ratio

SOM – System on a Module

SPI – Serial Peripheral Interface Bus

SRD – Step Recovery Diode

SVD – Singular Value Decomposition

TTT –Transit Time Tomography

USB – Universal Serial Bus

UART – Universal Asynchronous Receiver Transmitter

UMC – Ultraminiature Coaxial

UWB – Ultra-Wide Band

VGA – Variable Gain Amplifier

VFP – Vector Floating Point

VNA – Vector Network Analyzer

ACKNOWLEDGMENTS

First, I would like to express my deepest and most sincere gratitude for Dr. Randall Jean: my advisor, mentor, friend, and partner as well as my parents and extended family for their continuing wisdom and guidance. I need to acknowledge the hard work of past graduates from the Microwave Applied Metrology Lab: Chris Faulkner, Adam Parks, Stuart Gibbs, and Josh Daniliuc, who contributed in some fashion to this work. I also would like to thank my dissertation committee: Dr. Baylis, Dr. Li and Dr. Marks, and Dr. McClain along with Dr. Thompson, my graduate director. I am grateful for Mr. Orr, Mr. Hromadka, Mr. Hynan, and Mrs. Kerr for their assistance and especially patience. This work was funded in part by Rhino Analytics, GE Global Research, and Agilent Technologies.

Finally, thank you to everyone who tolerated my endless rants about this project for the past seven years. That was quite helpful.

To my mother and father,

for their unwavering support

CHAPTER ONE

Introduction and Background Information

The field of industrial microwave sensing can be addressed in terms of four main categories of study: material properties, geometric structures, robust signal processing, and implementation. Currently, it is the economics of the implementation category that is restricting the development and deployment of microwave sensors to a number of important industrial applications. The work of this dissertation has been to advance the state-of-the-art in microwave industrial sensing technology from the category of mere "implementation" to that of low-cost implementation in order to facilitate ubiquitous microwave sensing in a wide range of industrial environments. The developed system has been named a Pulse Dispersion Network Analyzer (PDNA).

Examples of Industrial Applications that will be Impacted

The following subsections briefly target four applications for which a low cost microwave sensor can be used to make a significant impact on manufacturing cost and product quality. The selected applications address important problems in food processing, energy production, infrastructure, and personal health. Specifically a metrology system is described which can measure percent fat, protein, and moisture in food products such as ground meat, the energy content and quality of steam, the water to cement ratio in the production of high performance fresh concrete, and the caloric content of foods at the point of consumption. These applications are presented to illustrate the wide range of possibilities for the PDNA.

Ground Meat

Meat is mainly a three component mixture of fat, protein, and water, if we disregard the fact that it also contains less than 1% in minerals. In a typical food processing operation, percent fat often has the largest variance of the three, ranging from 1% to 90%. Percent water is inversely correlated with the fat percentage and the ratio of water to protein is usually between 3:6 and 3.8:1 [1].

A batch of ground meat formulated by a processing facility will have a specific fat percentage requirement defined by the customer. That fat percentage is typically controlled by mixing a high fat content meat source with a reduced fat one. Without the availability of an on-line sensor, a time consuming and expensive laboratory analysis is done on each of the individual input sources so that mixing by weight can be used to determine the ratio of the blended mixture. Each meat source is mixed in large quantities on the order of thousands of kilograms which exhibit large variances in the percent fat, moisture, and protein within that batch. An in-line measurement system for percent fat could be used as feedback in a control loop to produce blends with percent fat values much closer to the customer's requested target.

Steam Quality

Steam quality is defined as the percent mass of water present in the vapor phase (m_v) divided by the total vapor plus liquid mass (m_l) as shown in (1). When steam is in the saturated region with a constant temperature and pressure, the enthalpy of the steam can vary by as much as 2200 kJ/kg as shown in Fig. 1. The ability to measure steam quality in-line would be an important measurement for a variety of energy intensive operations such as in the down-hole injection of steam for enhanced oil recovery or

improving the efficiency of operation of steam turbines in power plants. Some types of thick oil found in California and the Middle East have a rather high viscosity, which makes extraction of the oil difficult and slow. To reduce the viscosity and thereby increase oil well yield, steam is injected. The costs of the energy content of this steam directly reduce the well's profitability. If the energy content of the steam at each well head is known a more accurate cost benefit analysis could be done on each well.

$$S.Q. = \frac{m_v}{m_l + m_v} \tag{1}$$

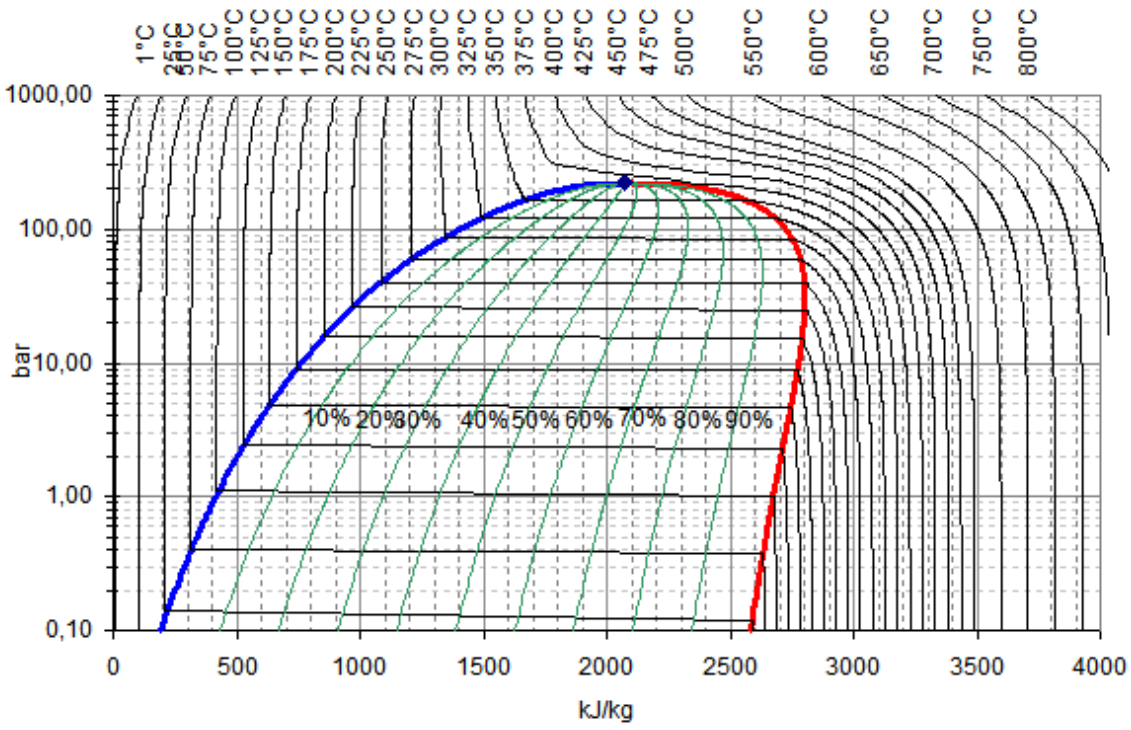

Fig. 1. Pressure-enthalpy diagram of steam.

A majority of coal and natural gas power plants in the United States as well as all nuclear power plants use steam at or below the critical point of water. When operating in the sub-critical region a percent of the steam can be in the liquid phase. Water droplets

cause extremely damaging erosion to turbine blades as well as increasing the corrosion due to steam impurities, which decreases turbine operational life and efficiency [2]. Turbine maintenance costs are approximately 0.5¢ per kWh [3].

Fresh Concrete

Concrete is composed of water, cement, and fine and coarse aggregate. The strength of concrete is linearly correlated with the water to cement (W/C) ratio as shown in Fig. 2 for various ratios of cement to aggregate. The current standard test for determining the W/C ratio is ASTM C143, which is a measurement procedure called a slump test [4]. The slump test uses a metal cone 12 inches in height, 8 inches in bottom diameter, and 4 inches in upper diameter. This cone is filled with concrete, placed on the ground, and then removed. The height decrease of the now free standing concrete is called the slump and is the standard for the specification of concrete strength. The accuracy of the measurement depends on the reading of a ruler out on the job site. A precise microwave instrument would drastically improve the precision and accuracy for the measurement of the strength of concrete as it is being poured during construction.

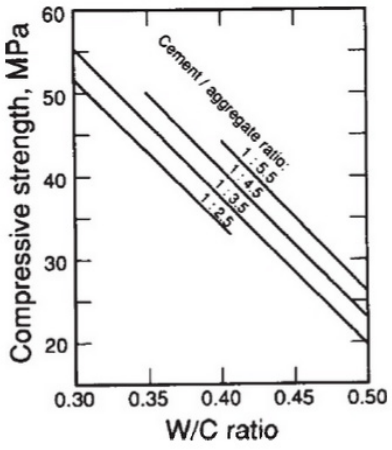

Fig. 2. Compressive strength of concrete [5].

Caloric Measurement

Increased body weight has been correlated with increased risk for cancer [6], diabetes and heart disease [7]. A consumer instrument to measure the caloric content of food would improve individual's dietary management and weight loss ability [8]. Scientists at GE Global Research have developed and patented an algorithm (2) to calculate the calorie content of food based on its mass in grams (M), percent water (W), and percent fat (F) [9]. This equation when applied to over 6500 foods in the USDA National Nutrient database exhibited a strong correlation with actual calories as shown in Fig. 3.

$$Calories = M\big(3.79(1 - W - F) + 8.89(F)\big) \tag{2}$$

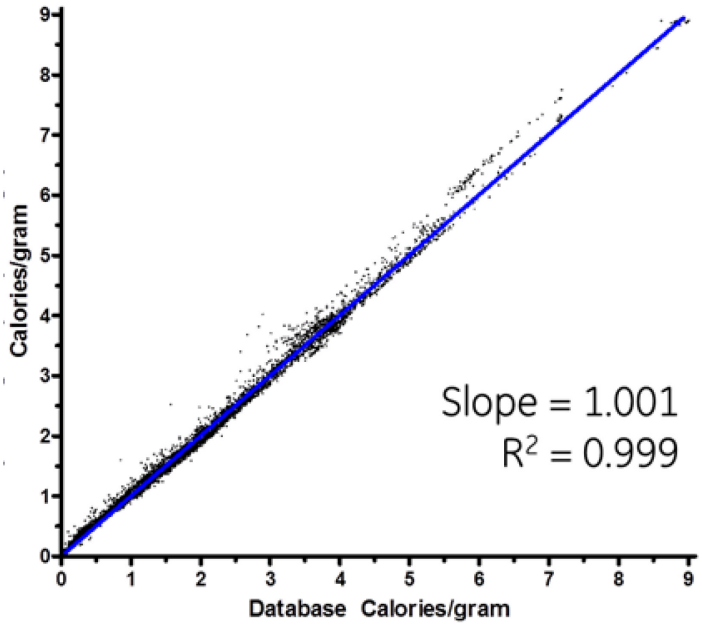

Fig. 3. Comparison of calories from USDA food database and (2).

The instrument would also be beneficial to increase the accuracy of calorie values reported by restaurants and grocery stores. One study found that restaurants have under reported calories by 18±59% with a maximum of 200% difference [10]. This large variance and inaccuracy could be reduced with a commercial grade caloric counter. To implement a non-destructive caloric counter, percent water and fat would need to be measured on a plate of food. A mockup of a consumer product produced by GE is shown in Fig. 4.

Fig. 4. Commercial mockup of a calorie counter.

Material Properties and Geometry

Two of the major factors in configuring a microwave sensor are material properties and geometry. Controlling the sensor geometry represents the ability of the engineer to create various structures such as waveguides or resonators for causing the energy to interact with the material to be measured based upon contacting or containing the material as well as accounting for the interaction of electromagnetic waves at the boundaries of materials which satisfy Maxwell's equations. The term material properties

can be divided into two categories: those known and unknown. The known properties of conductors and dielectrics can be used to create novel structures. As different materials are mixed together, the mixture's composite properties vary with the constituent ratios, and when measured can be correlated back to determine the mixture.

Permittivity and Conductivity

The response of a material to electromagnetic waves is determined by that material's complex permittivity, complex permeability, and conductivity which are functions of frequency, temperature, and density. Materials can also be non-homogeneous or anisotropic or both, where those electromagnetic properties are also functions of the interrogating field's position and polarization inside the material. The number of independent variables can be simplified depending on the materials involved in the industrial application. For the applications presented in this work, complex permittivity over frequency, temperature, and frequency independent conductivity will be the main variables considered.

Changes in a material's permittivity over frequency are due to Maxwell-Wagner polarization, molecular orientation, ionic polarization, and electron polarization displayed in Fig. 5. The Maxwell-Wagner polarization occurs due to an accumulation of charge on the boundary between two materials. This effect is only present in non-homogenous or biological materials and dramatically increases the low frequency permittivity by several orders of magnitude. For example, in biological materials such as fat, the Maxwell-Wagner polarization doubles the permittivity as the frequency is reduced from 100 MHz to 14 MHz.

The molecular orientation polarization occurs when polar molecules exposed to an electric field rotate to orient parallel to the direction of the field. These molecules have a relaxation time which is defined as the time it takes the molecule to rotate due to an applied electric field. When the period of the oscillation of the electric field approaches the molecular relaxation time, the material's permittivity begins to decrease. This relaxation time commonly occurs in the microwave frequency range.

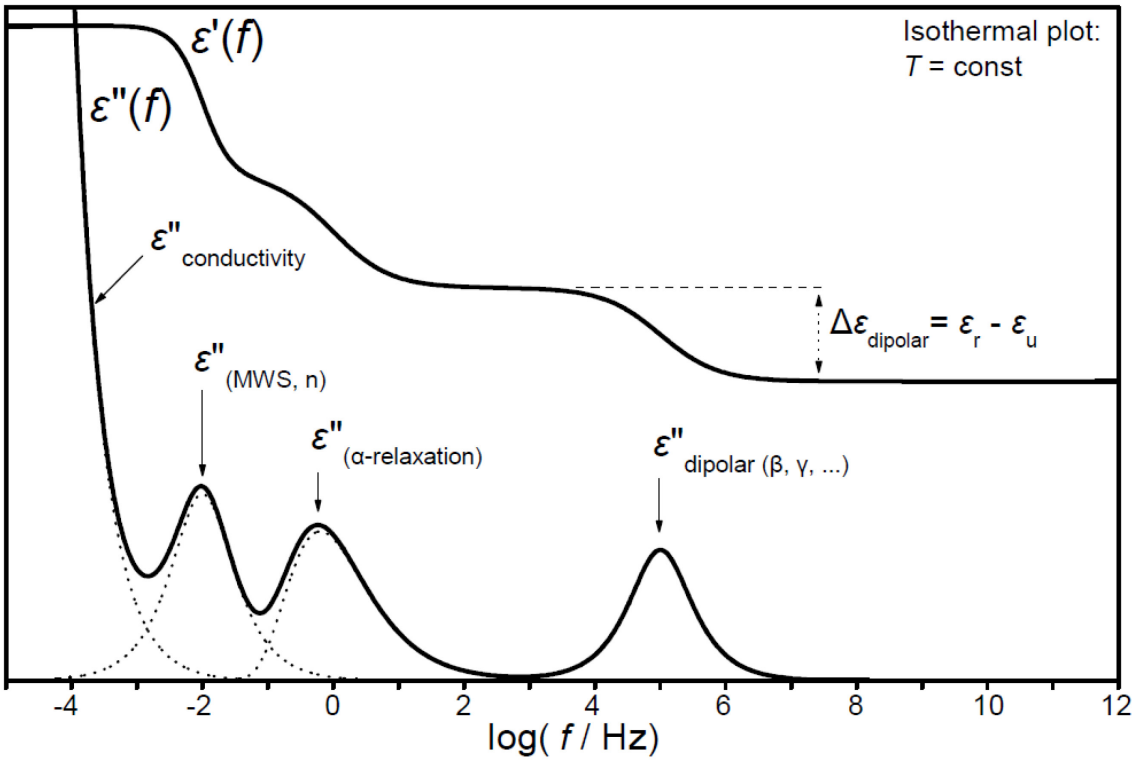

Fig. 5. Polar molecule's permittivity over frequency [11].

Three common mathematical approximations for a material's permittivity as a function of frequency are the Debye, Cole-Cole, and Lorentz models. The Debye model can be highly accurate for the molecular relaxation effects in polar materials and can be expanded into a second order model to include higher frequency atomic relaxations. The Cole-Cole model is more accurate than the Debye model for biological materials with

large interfacial effects. The Lorentz model is used to describe the atomic and electronic relaxations in the THz frequency range. For industrial processes in the 200MHz to 5GHz frequency band, the well-known Debye model is suitable for most polar molecules. The first-order Debye model including conductivity losses is described by (3), where ε_∞ is the high frequency permittivity, ε_s is the low frequency permittivity, and τ is the material's molecular relaxation time.

$$\varepsilon(\omega) = \varepsilon_\infty + \frac{\varepsilon_s - \varepsilon_\infty}{1 + j\omega\tau} + \frac{\sigma}{j\omega\varepsilon_0} \tag{3}$$

A mixture can be described as having an effective permittivity from the aggregation of the individual permittivities of the mixture components. Many models exist for approximating this effective permittivity for both homogeneous and heterogeneous mixtures. A widely used set of equations for effective permittivity (ε_{eff}) are based on the "power-law" shown in (4) with different values of the a parameter [12]. In (4) ε_1 and ε_2 are the permittivities of the individual components and φ_1 is the percentage of volume for the first component. For the a parameter, the Birchak formula uses $a = \frac{1}{2}$ [13], the Looyenga formula uses $a = \frac{1}{3}$ [14], and Ulaby has published with $a = 1$ [15].

$$\varepsilon_{eff}^a = \varphi_1\varepsilon_1^a + (1 - \varphi_1)\varepsilon_2^a \tag{4}$$

For a heterogeneous mixture with small inclusions, the Maxwell Garnett Equation (5) is an approximation of the effective permittivity, ε_{eff} as a function of the permittivity of the medium (ε_m), the permittivity of the inclusions (ε_i), and the percentage of volume

of the inclusions (φ_i) [16]. This permittivity model is useful for taking into account the effect of large aggregate in fresh concrete. However, the model is usually only considered effective for electrically small inclusions. Thus at higher frequencies it is more difficult to predict the permittivity effects as multiple modes begin to propagate.

$$\varepsilon_{eff} = \frac{2\varphi_i(\varepsilon_i - \varepsilon_m) + \varepsilon_i + 2\varepsilon_m}{\varepsilon_i + 2\varepsilon_m + \varphi_i(\varepsilon_m - \varepsilon_i)} \tag{5}$$

Waveguide Cutoff Analysis

Two established methods to measure the permittivity of a material in the microwave frequency band are coaxial line reflectometry and network analysis [17]. Both of these techniques require precise control of the sample material's thickness and position which is prohibitive in an in-line industrial environment. An alternative technique to measure a material's permittivity as well as conductivity is to measure the response of a waveguide filled with the material [18]. The rectangular waveguide in Fig. 6 has dimensions of a and b. The cutoff frequency of a rectangular waveguide is governed by (6), where ε_r is the relative permittivity of the material, and m and n are the number of half-wavelengths across their respective waveguide dimensions of a and b [19].

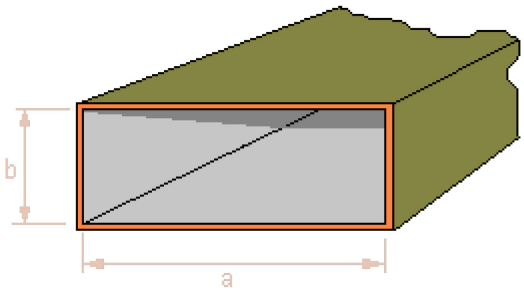

Fig. 6. Rectangular waveguide with dimensions.

$$f_c = \frac{c}{2\pi\sqrt{\varepsilon_r}} * \sqrt{\left(\frac{m\pi}{a}\right)^2 + \left(\frac{n\pi}{b}\right)^2} \tag{6}$$

However, when the permittivity is complex and a function of frequency, the propagation constant can be used to find the response of the waveguide over frequency given by (7). The real and imaginary parts of the propagation constant are respectively called the attenuation and phase constants. Note that the permittivity ε is complex and a function of frequency thus using the term, constant, is slightly misleading.

$$\gamma(\omega) = \sqrt{\omega^2\mu\varepsilon - \left(\frac{m\pi}{a}\right)^2 + \left(\frac{n\pi}{b}\right)^2} \tag{7}$$

The ideal S_{21} response of a rectangular waveguide as computed with the Debye model for the dominant TE_{10} mode is illustrated in Fig. 7. The simulated waveguide dimensions are 50 mm wide and 0.1 m long waveguide and then filled with water of varying levels of purity and temperatures. The blue curve is deionized water at room temperature. The shift in the cutoff frequency between the red and blue traces illustrates water's large permittivity variation due to changes in temperature. This dependence between temperature and permittivity necessitates an independent temperature measurement for multicomponent mixtures with substantial water content. Non-polar molecules also exhibit a correlation between permittivity and temperature, but the variation is not as large. A temperature measurement might not be needed if the process temperature does not vary more than a few degrees.

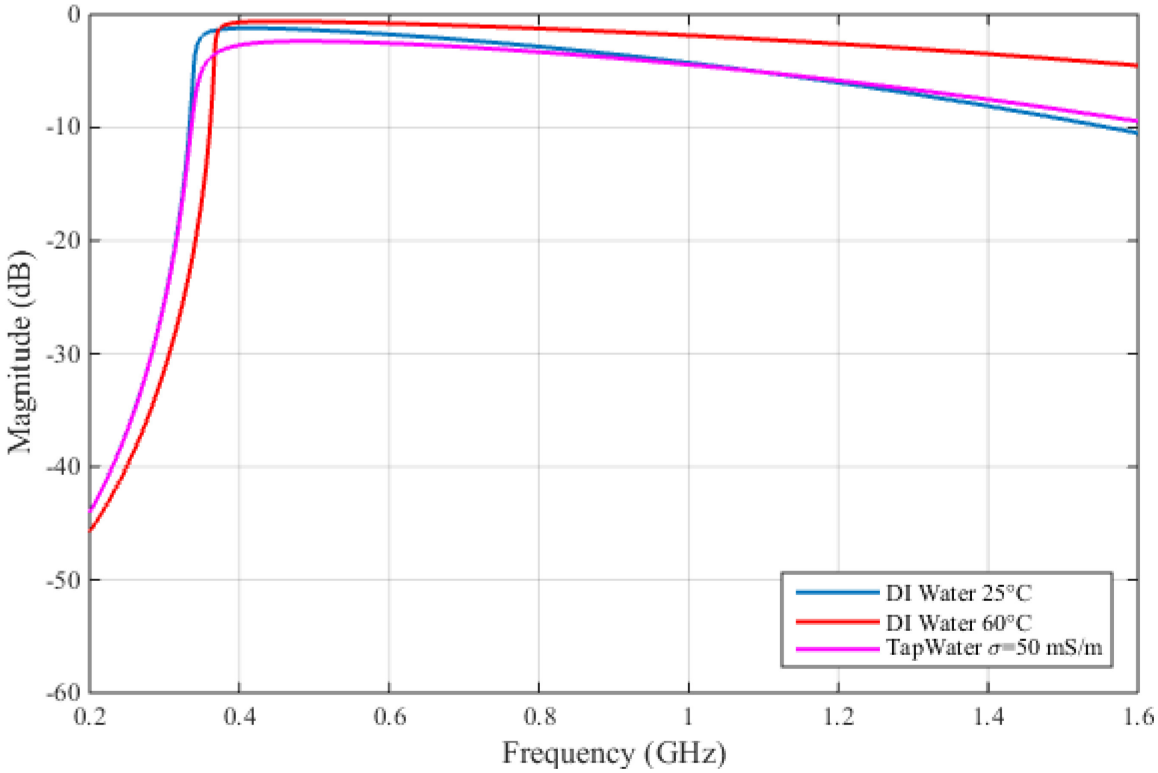

Fig. 7. Mathematical response of ideal rectangular waveguide loaded with water.

Fig. 8 shows an idealized volumetric mixture of deionized water and oil in a waveguide using the same dimensions as the previous figure. Once again this is calculated using the permittivities of water and oil, and not a measured response. At constant temperature, the cutoff frequency decreases by approximately 50 MHz for an increase from 40% to 50% water content. By measuring this frequency shift of a mixture with an unknown ratio of components, then that ratio can be inferred based on the cutoff frequency. However, the frequency shift is not a linear function, as noted in (6), so a large change in mixture permittivity will require a non-linear fitting function. Small changes in permittivity, such as an industrial process control with a target mixture ratio, can use linear methods for calibration [20].

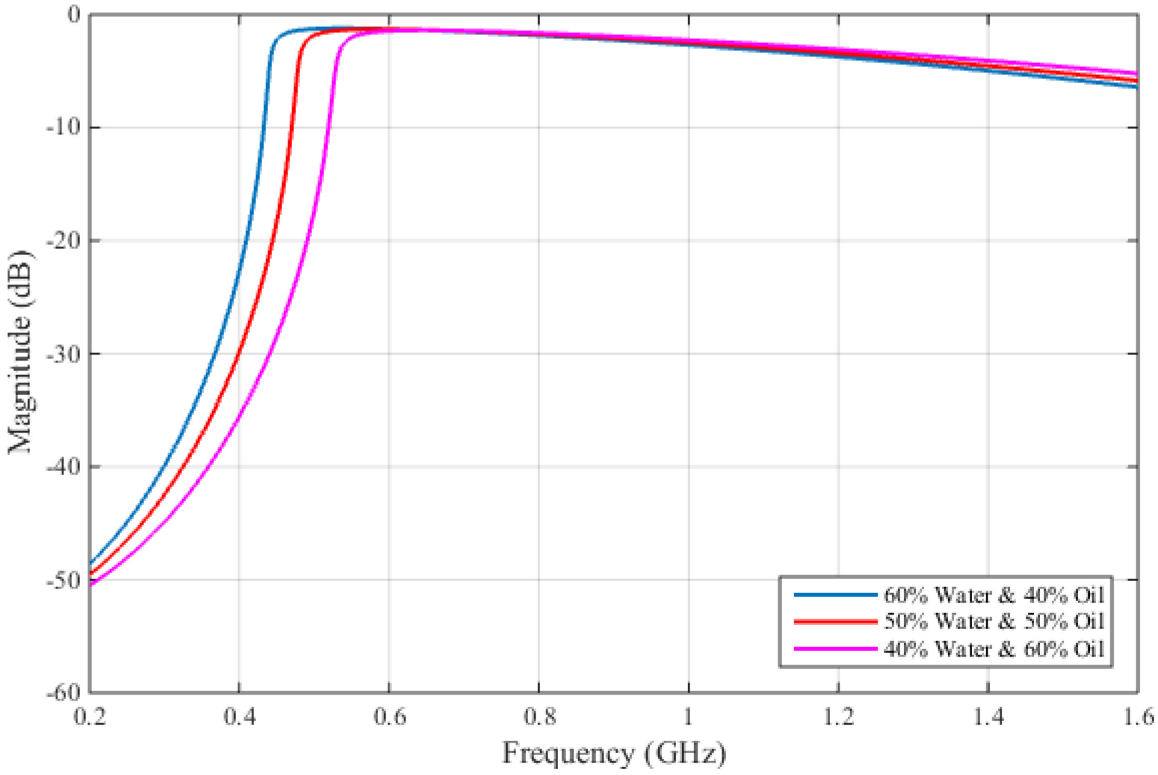

Fig. 8. Mathematical response of ideal rectangular waveguide loaded with an oil and water mixture.

Permittivity and conductivity can be determined by using the spectral response of a waveguide loaded with a material. An amplitude decrease at cutoff is associated with an increase of conductivity. An amplitude change in the pass band frequency range can be caused by changes in the relaxation time of a polar molecule, which could signify large changes in temperature. Shifts in the cutoff frequency convey a change of the real part of the material's permittivity.

A circular waveguide structure can have advantages for an in-line excitation structure as many industrial processes use circular piping. For a circular waveguide, the cutoff frequency is given in (8), where r is the radius, n and m are the number of half-wave lengths in the circumferential and radial dimensions, and p'_{nm} is the m^{th} root of the derivative of an n^{th} order Bessel function of the first kind. The first mode to propagate in

a cylindrical waveguide is the TE_{11} mode. A four inch diameter pipe is one of the smallest commonly found in industrial plants and its cutoff frequency is 1.729 GHz when filled with air.

$$f_{c_{nm}} = \frac{p'_{nm}}{2\pi r\sqrt{\mu\varepsilon}} \tag{8}$$

Resonance Analysis

Another method for measuring the permittivity of a material is to design a high Q resonator where the resonance frequency is a function of the material properties. These resonators could be designed at different frequencies to determine the permittivity of the material at those frequencies. The frequencies of the nulls will shift with changes in the material's permittivity replicating the behavior of the shift in the cutoff frequency of a dielectrically loaded waveguide. The depth of the null is correlated with the imaginary component of the material's permittivity, which are the electrical losses. The resonant analysis method has an advantage in ability for multiple measurements of the full complex permittivity at different frequencies. Resonators can also be waveguide cavities or planar structures, leading to a larger range of geometric possibilities for the sensor structure.

Split ring resonators have been shown to have a large Q as well as much lower resonance frequencies when compared to structures of similar size. A large Q increases the magnitude depth of the resonance which allows for the frequency of the null to be measured with an increased precision. Circular and square split ring resonators are shown in Fig. 9, with their complementary versions in Fig. 10. The structures exhibit electrical resonance when the capacitance between the rings and their gaps equals the

ring's inductance. The rings can be used to create structures which exhibit negative permittivity as well as negative permeability at their design frequencies. When used in this fashion they are called a metamaterial, double negative material, or left hand filter. One specific advantage is a resonance frequency which is much lower when compared to other structures of similar size.

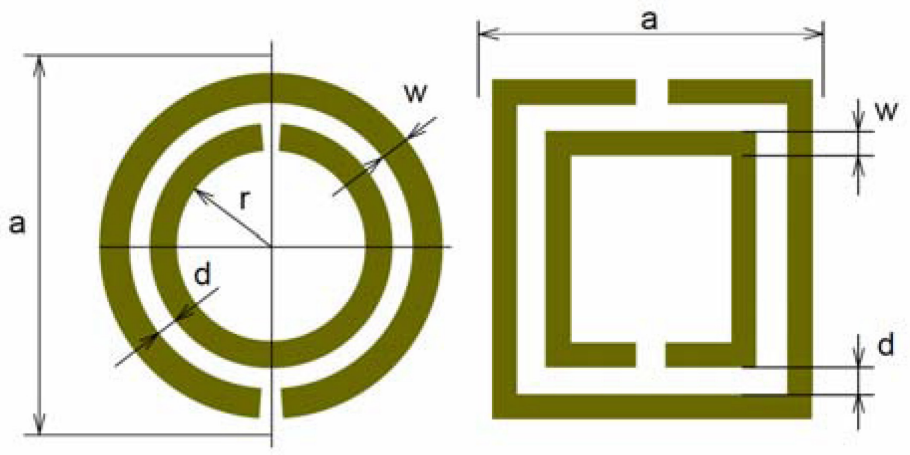

Fig. 9. A circular and rectangular split ring resonator.

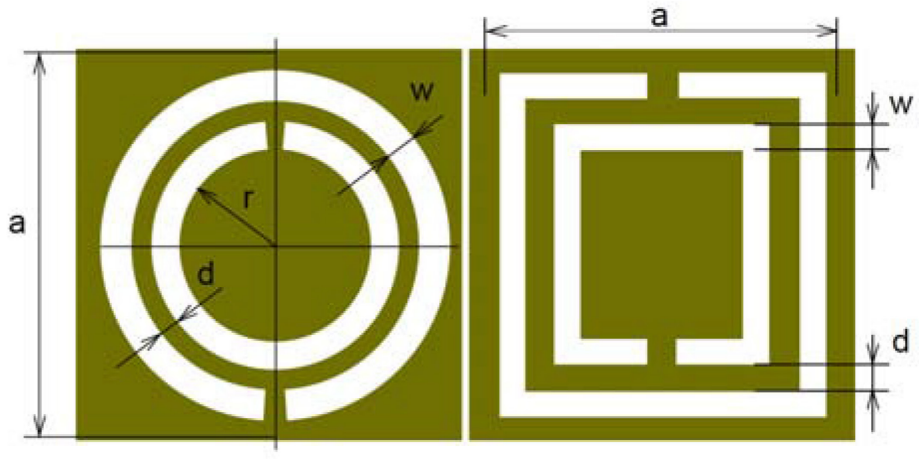

Fig. 10. A circular and rectangular complementary split ring resonator.

Several methods can be used to excite the SSRs and couple the electromagnetic fields resonating in the SSRs to a material under test. A common method is to use a

microstrip transmission line wherein the ground plane is interrupted by CSSRs. Fig. 11 shows a material under test placed on the ground plane tangent to the CSSR. In this configuration the resonance frequency will vary with the permittivity of the material [21]. The coupling between the CSSR and the material under test is a result of the fringing fields. The thickness of the material under test as well as the dimensions of the ring determines the amount of energy coupled into the material.

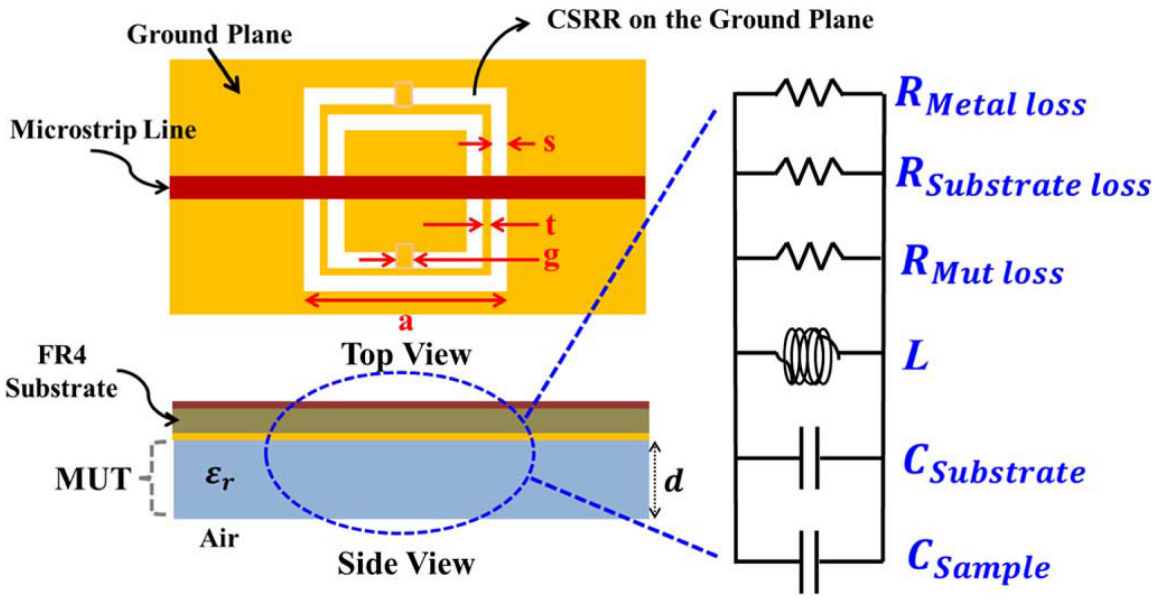

Fig. 11. CSSR excitation structure [21].

Fig. 12 is the resultant frequency spectrum of the microstrip transmission line. The figure illustrates the shift in resonance frequency as the material under test is varied between various dielectric substrates from Rogers Corportation as well as FR4. The relative permittivity of these materials ranges from 2.2 to 10.2 exhibiting a 600 MHz shift in frequency. The thickness of these materials is relatively small with most under one millimeter.

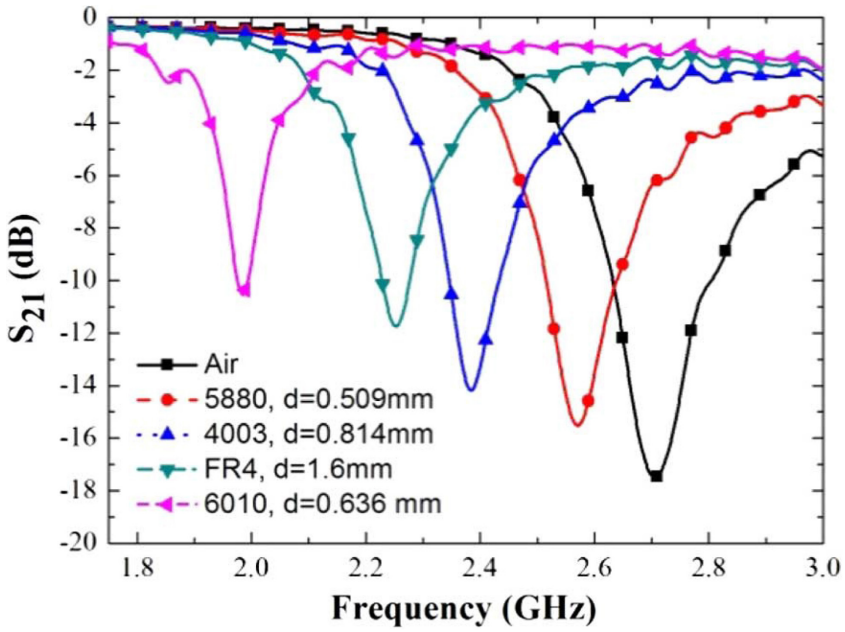

Fig. 12. Planar CSSR microstrip loaded with various dielectric materials [21].

A complementary split ring resonator could also be excited inside a waveguide loaded with the material under test. The right portion of Fig. 13 illustrates four different possible orientations of the CSSR inside of a C band waveguide. The orientation of the ring changes which fields can couple to the structure. In order from one to four, the coupling is as follows: electric and magnetic, electric only, magnetic only, and no coupling. The plots on the left side of Fig. 13 show the resonating null in the S_{21} response from each CSSR orientation at different orientations [22]. The upper left *a* graph uses a normal CSSR where the lower left *b* graph uses a continuous CSSR. The continuous CSSR's response is not susceptible to a rotation in the plane along the direction of propagation, but cannot couple any energy when in the plane of the waveguide aperture. The resonance frequency of the rings can be decreased by increasing their dimensions.

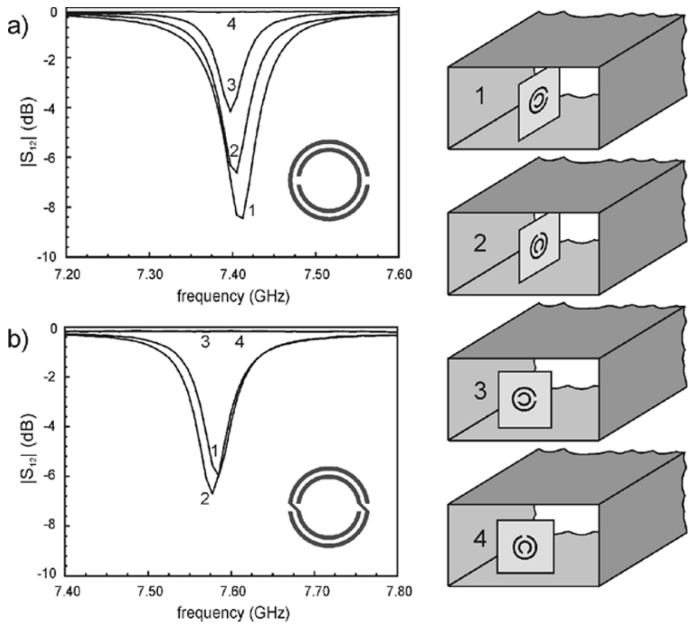

Fig. 13. Waveguide response with inserted CSSR [22].

Pulse Spectroscopy

Another major component to microwave sensing is the electronic implementation of the measurement. Two distinct methods of interest for determining the response of a material are swept frequency and impulse. In a swept frequency system, the response to each frequency is measured individually so that a wideband measurement takes more time than a narrowband one. An impulse system measures all frequencies simultaneously, but a structure with a narrowband frequency response takes more time to measure than a wideband one. The following sections discuss the principles, tradeoffs, and specifications of the electronics' implementation for industrial applications.

Swept Frequency

The traditional method to characterize the response of a device over a broad frequency uses a vector network analyzer (VNA). The VNA produces a RF sinusoidal signal and the frequency of this signal is then swept over the band of interest. A

comparison of the amplitude and phase of the generated signal to the received signal which has passed through the material under test yields the forward scattering parameter, S_{21}, which can be interpreted to be the system's frequency response. Fig. 14 is the block diagram of a typical VNA found in RF laboratories.

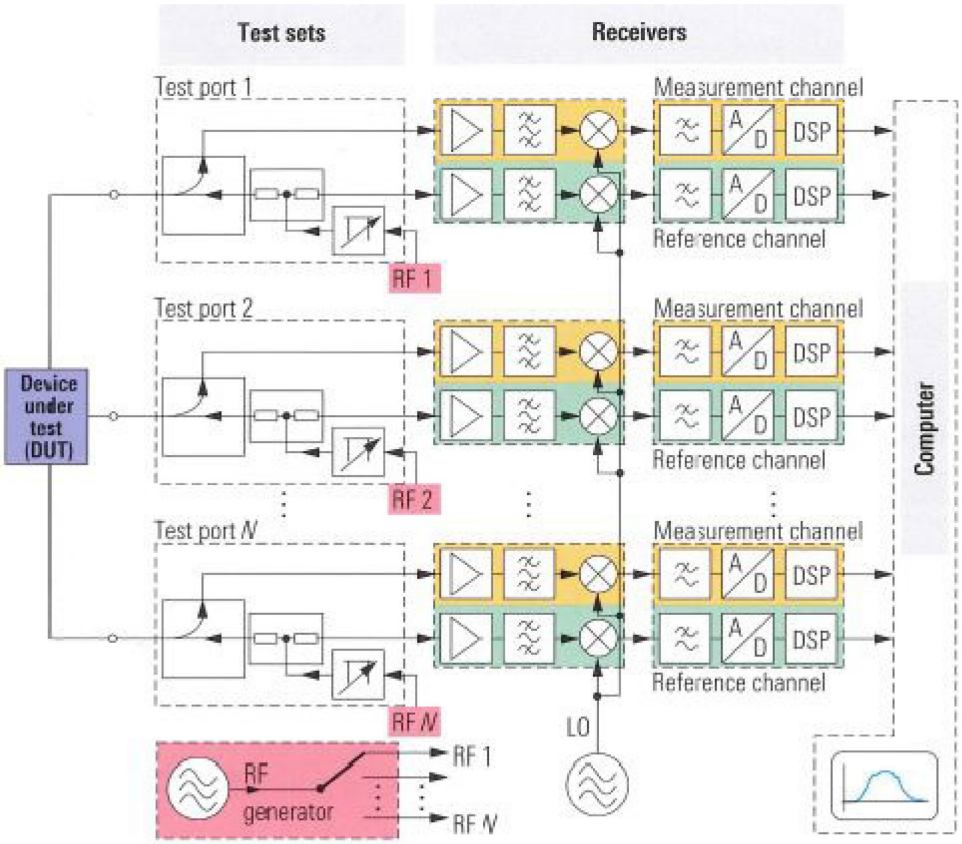

Fig. 14. Block diagram of a Rhode and Schwartz vector network analyzer.

The sinusoidal signal is generated using voltage controlled oscillators embedded in a phase locked loop. Multiple oscillators must be used to cover an ultra-wide band frequency range. The receiver uses superheterodyne techniques to shift the RF sinusoid to an intermediate frequency. This down conversion requires a mixer and local oscillator that is at a slightly different frequency than the RF excitation signal. The ultra-wide band mixer in the RF receiver is usually the limiting factor for dynamic range since the input

power must be in the linear region to maintain calibration. This IF frequency from the mixer is then filtered and sampled using an analog to digital converter.

After the IF signal is digitized, it is filtered at a controllable IF bandwidth. The filtered signal is then demodulated to baseband using a digital IQ demodulation at the IF frequency. This demodulation directly produces the real and complex components of the signal. The bandwidth of the IF filter is inversely correlated with the noise floor and the measurement's acquisition time.

For internal calibrations, the VNA has a splitter on the output of the RF signal which is the input to a separate secondary receiver. The amplitude and phase of the generated RF is then compared with the amplitude and phase of the received signal at each frequency to produce the S21.

The VNA has several drawbacks for use in an industrial environment. It is not specified to industrial temperature ranges, and the large dimensions prohibit mounting on pipes. However, the largest detractor for industrial use is the cost. For example, the MSRP of Keysight's E5061B 3GHz network analyzer is currently $26,926. This cost is uneconomical for a large set of applications and necessitates an alternative set of electronics for embedded industrial sensing.

System Design Specifications

First, design criteria need to be established for an alternative system that would fulfil the needs for the previously mentioned industrial applications. A few applications might require slightly different specifications depending on material loss, sensor operating frequencies or other application specific needs.

A bandwidth specification can be derived from the dimensions of common pipes and waveguides currently in use. A rectangular structure already in industrial use as a Guided Microwave Spectrometer (GMS) has a controlling diameter of 47.5 mm which results in an air cutoff frequency of 1.89 GHz. A common four inch steel cylindrical pipe has an air cutoff frequency of 1.729 GHz. Thus a 2GHz 10dB system bandwidth is defined where the spectrum amplitude remains within 10dB of its maximum out to 2 GHz.

The dynamic range of the system must be able to accommodate lossy materials as well as larger pipe diameters where the signal will incur even larger attenuation while maintaining signal integrity on materials with near zero loss. At a minimum, the dynamic range needs to be 50dB for adequate performance, but larger dynamic ranges can accommodate greater pipe diameters for lossy materials.

For a system in use in industrial environments, there cannot be a large amount of complex operator interactions. An operator cannot be responsible for normal microwave laboratory calibration procedures. The system needs to automatically correct the output spectrum for internal frequency characteristics as well as changes in temperature.

The most common and primitive process control method is a 4-20 mA current loop. Support of at least one 4-20 mA output is mandatory as it is prevalent is a majority of industrial settings due to its ease of implementation and reliability. For full instrument control the HART Protocol is commonly used. It is a digital signal which is overlaid on the 4-20 mA current loop. Well over twenty-five different process automation protocols exist, most of which are defined in IEC 61158 fieldbus standards. One protocol, Modbus, stands apart from the rest as it is openly published and royalty-free. Its simplicity,

reliability, and costs have caused it to become a de facto standard and the most widely used protocol. Incorporating Modbus in the PDNA will allow for compatibility in a wide range of industrial plants.

A user interface needs to be developed to control operator system variables and perform a process calibration. A secondary engineering user interface should be available to diagnose problems and control all the system variables. Frequency resolution under 1 MHz should be attainable with unsubstantial processing time.

The instrument enclosure needs to be rugged and industrial grade with at least a NEMA 4 and IP 66 ratings. Since the design and layout of the electronics can be heavily dependent on the enclosure, the enclosure is included in the specifications. The XDHM from Adalet was chosen to house the electronics as it satisfies the requirements, can be pipe mounted, and industrial factories are accustomed to circular enclosures such as this one. The enclosure also carries an explosion proof Class I, II, and III rating which allows for operation in environments with hazardous gases, dusts and fibers.

Fig. 15. Adalet XDHM instrument enclosure.

Time Domain

An alternative to the vector network analyzer's swept-frequency excitation is a pulsed time domain solution that generates all of the desired frequencies simultaneously. Theoretically an impulse or Dirac delta function has infinite bandwidth and would therefore produce all of the frequencies desired in the response. However, realized pulses have finite bandwidth and finite energy content with measureable, i.e. non instantaneous, rise and fall times, and an extended duration. To adequately determine the response of a system out to multiple GHz, these pulses must have widths on the order of a couple hundred of picoseconds. The difficulty of this task can be conveyed by the fact that light travels only 2.99 cm every 100 picoseconds.

The bandwidth of the electrical response produced by pulse excitation is limited by the frequency energy in the transmitted pulse, i.e. the bandwidth is limited to frequencies where the spectrum of the transmitted pulse is significantly greater than the noise floor. The magnitude of the pulse's spectrum decreases with frequency, which also reduces the system's dynamic range as frequency increases. A good metric for the bandwidth of the PDNA for a number of important applications is the 10 dB bandwidth, which is defined as the frequency where the magnitude of the pulse's spectrum falls to 10 dB lower than the maximum magnitude.

By way of illustration, consider a rectangle function as a simple model for pulses of the type being used in the present system. Taking the Fourier transform,

$$\mathcal{F}(\omega) = \int_{-\infty}^{\infty} f(t) e^{-2\pi j \omega} \tag{9}$$

of a rectangular pulse,

$$f(t) = \text{rect}(\frac{t}{t_0}) \tag{10}$$

results in a sinc function in frequency .

$$\mathcal{F}(\omega) = \frac{1}{\sqrt{2\pi t_0^2}} \operatorname{sinc}\left(\frac{\omega * t_0}{2\pi}\right) \tag{11}$$

Equation (11) quantifies the frequency information contained in the pulse and would be the ideal result from a discretized Fourier transform such as the FFT. The sinc function has nulls where no frequency content is transmitted when the argument of the sinc function equals an integer multiple of π. Thus the frequency response of the MUT cannot be determined near those frequencies. This property is a limitation with pulse spectroscopy, but can be mitigated by designing the nulls to occur at frequencies higher than the frequencies of interest. The position of the first null can be increased in frequency by decreasing t_0 in the argument which decreases the width of the rectangle function.

For a more accurate analysis of the frequency response of a real pulse, a slightly more complicated model is used shown in Fig. 16.

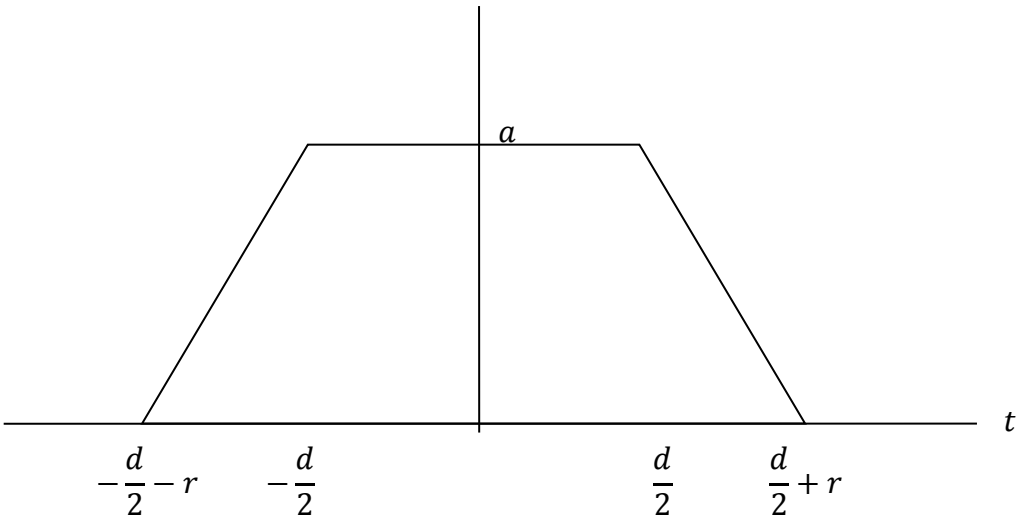

Fig. 16. Model of a pulse.

The parameter d represents the hold time of the pulse, r is the transition time, and a is the amplitude as defined in the piecewise function (12).

$$f(t) = \begin{cases} \frac{a}{r}t + a\left(1 + \frac{d}{2r}\right), & for -\frac{d}{2} - r \le t \le -\frac{d}{2} \\ a, & for -\frac{d}{2} \le t \le \frac{d}{2} \\ -\frac{a}{r}t + a\left(1 + \frac{d}{2r}\right), & for \frac{d}{2} \le t \le \frac{d}{2} + r \end{cases} \tag{12}$$

The Fourier Transform of the model (12) is given in (13). As the argument of the sinc function gets smaller, the first null position increases in frequency. From (5), the first sinc function with frequency scaling factor $(d + r)/2$ will always have a first null lower in frequency than the second sinc function with $d/2$ as the scaling factor. Since the sinc function with $(d + r)/2$ for the scaling term is the limiting factor, pulse transition times and duration have approximately equal importance in achieving increased pulse bandwidth.

$$\mathcal{F}(\omega) = -a(d + r)\,\mathrm{sinc}\left(\frac{(d + r)\omega}{2}\right)\mathrm{sinc}\left(\frac{r\omega}{2}\right) \tag{13}$$

The pulse model in Fig. 16 uses linearly sloped sides to model the rise and fall of the pulse and was produced by piecewise functions in MATLAB. The pulse in Fig. 17 demonstrates transition times of 100 ps and a hold time of 200 ps which results in a first lobe bandwidth of 3.2 GHz. This performance would have excellent utility for a number of applications provided that hardware can be designed and fabricated with 100 ps transition times and a 200 ps hold time.

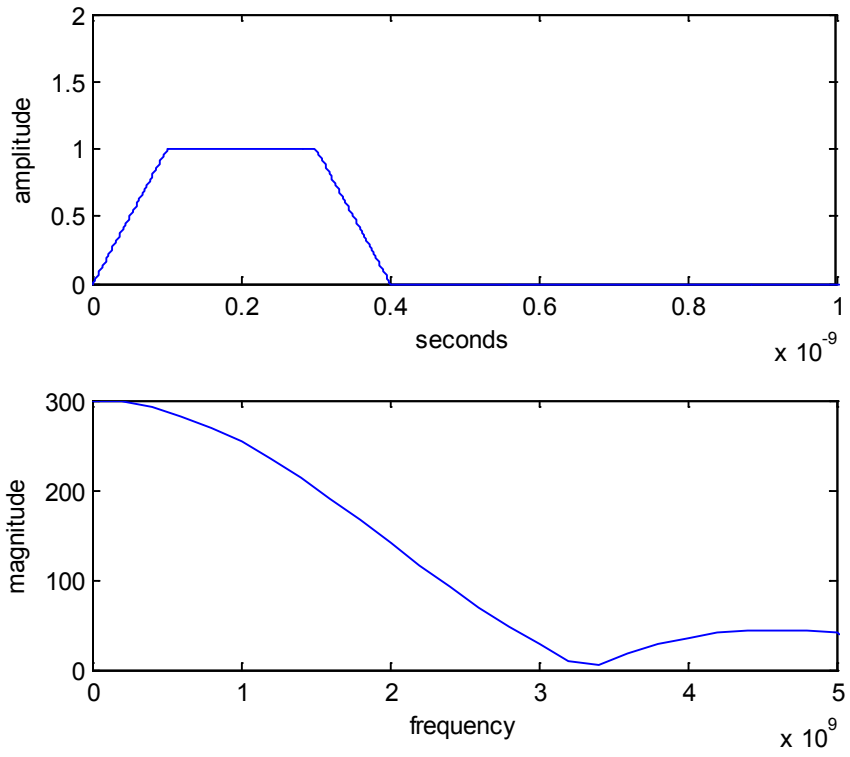

Fig. 17. Frequency content of a test pulse with 100 ps transition times and a 200 ps duration.

Equivalent Time Sampling

Generating an UWB pulse is only half of the requirement of a pulse transceiver. For example, to receive an UWB pulse with 2.5 GHz of bandwidth, a 5 Gs/s analog to digital converter (ADC) would be required to satisfy the Nyquist sampling criterion. Currently, the fastest ADC available on the popular commercial site, DigiKey, is only 3 Gs/s and costs $815. A design involving an RF ADC would not be a cost effective or adequate solution so an alternative method is needed. Equivalent time sampling (ETS) is a technique that may be applied to repetitive signals to achieve an equivalent sampling rate that is significantly greater than the actual sampling rate of an ADC. The ETS technique triggers the receiver at a slightly slower frequency than the generator. As the receiver triggering clock slowly drifts out of phase from the generator triggering clock,

the point sampled from the RF input signal shifts with the phase difference. Each generated pulse provides a single sample point in the extended time domain.

Fig. 18 provides an example of equivalent time sample. The top panel of Fig. 18 contains generated pulses with pulse widths of 1ms and a 1 kHz repetition frequency. The middle panel shows impulses representing the receiver trigger signals that have a slightly slower pulse restitution frequency of 0.9 kHz. These frequencies are much slower than the frequencies used in the system and are only used here for illustration purposes. The 100 Hz offset between the generation and the receiver causes the receiver to extend the pulse in time by a factor of 10. This factor is called the extended time factor (ETF) and is expressed by (14), which includes the values used in the Fig. 18 example.

$$ETF = \frac{f_0}{\Delta f} = \frac{1\ k\text{Hz}}{100\ \text{Hz}} = 10 \tag{14}$$

From (14), the original 1 ms pulse has been extended in time by a factor of ten so that it is now 10 ms wide. This effect is illustrated in the bottom section of Fig. 18. The transmitted pulse train from the top section is shown along with blue dots at each point where the receiver is triggered from the middle section. Then the dotted blue line is an $\sin(x)/x$ interpolation between the blue data points representing the analog reconstruction of the original pulse that is now ten times as wide. In practical use much larger ETFs are used allowing for many more data points. Again, the ETF of ten used in Fig. 18 is only for illustration purposes.

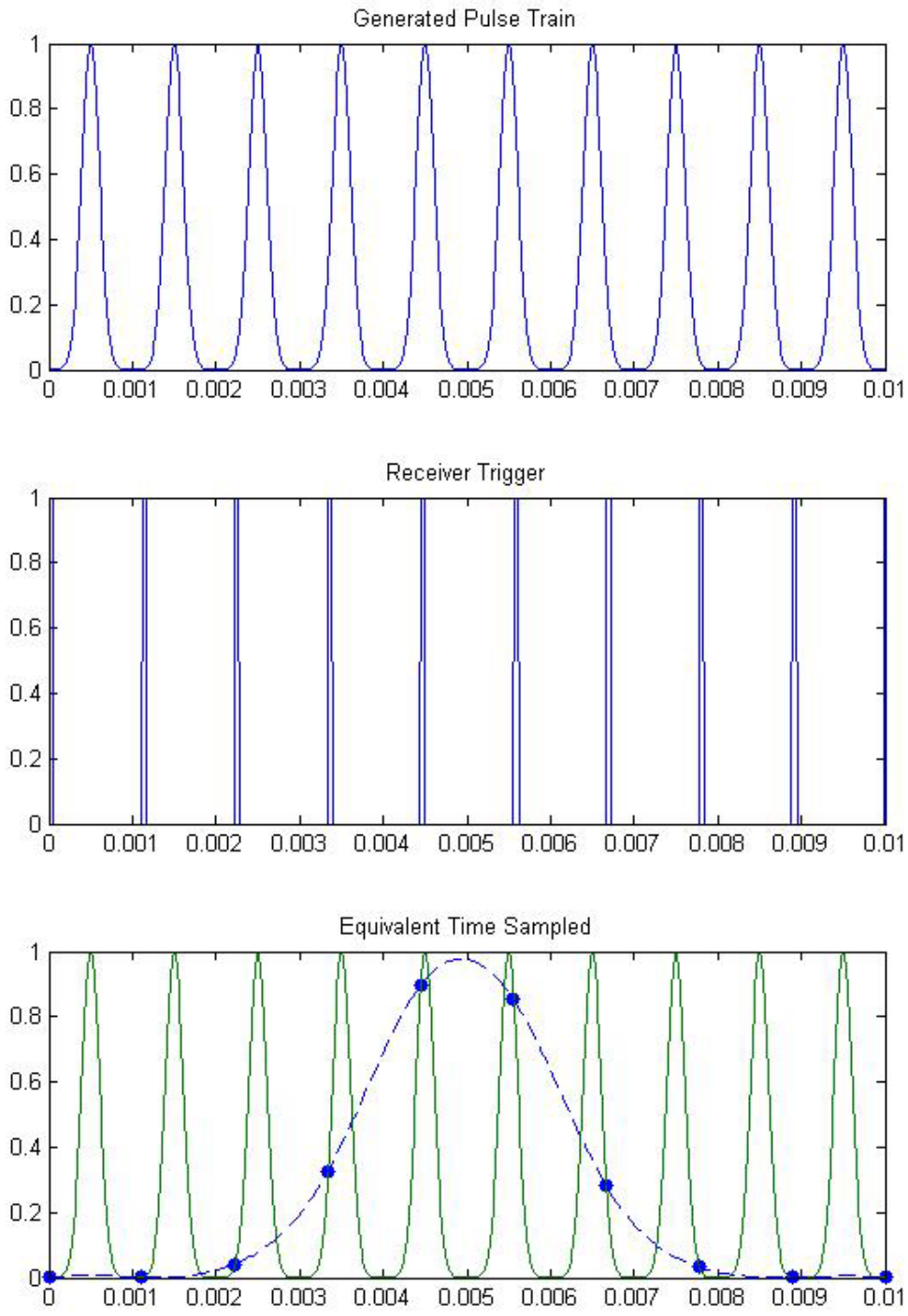

Fig. 18. Equivalent time sampling example.

Fig. 19 illustrates an overlay of the sub-sampled pulse with the generated pulse. Note the two different time scales, which vary by the designed factor of ten. This extended time factor designates how many data points will be used in the sub-sampling. The Pulse Dispersion Network Analyzer operates with ETFs between 50,000 and 1,000,000. As the ETF increases so does the time of acquisition by the same amount.

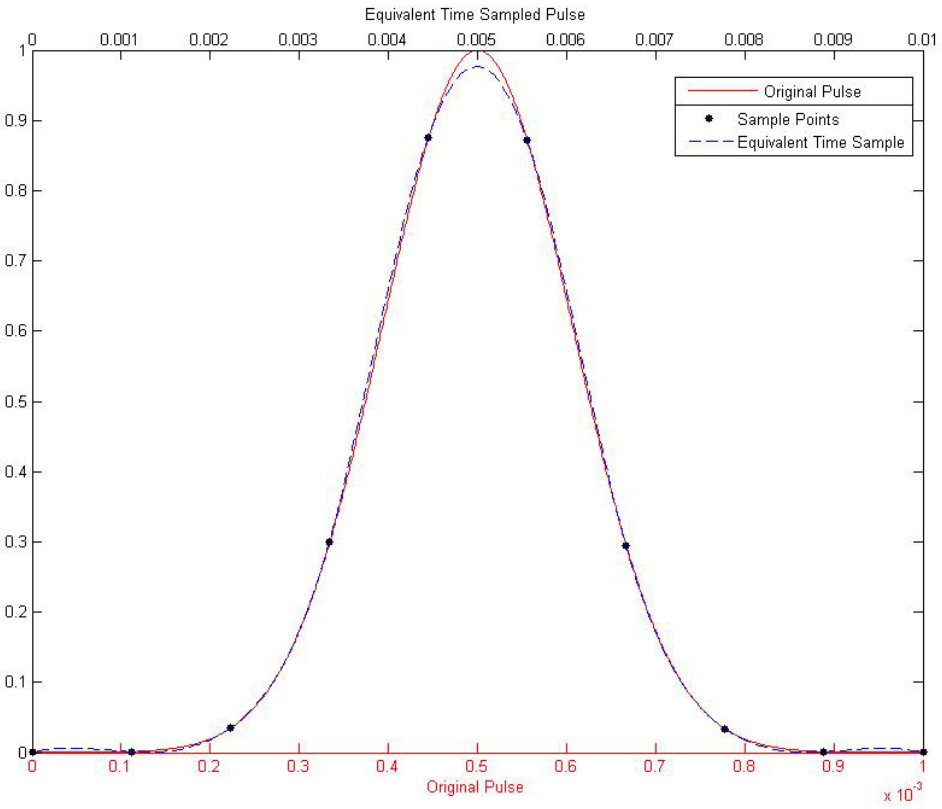

Fig. 19. Equivalent time sampling overlaid with original pulse.

CHAPTER TWO

A Hardware Design Example

This chapter details the hardware design of a microwave metrology system for the measurement of material properties which satisfies the needs of the four example industrial applications. The Pulse Dispersion Network Analyzer consists of six printed circuit boards laid out in Fig. 20. Two of the PCBs are purchased from third parties, the Phycore AM335x from Phytec and the VMS-20 from CUI. The PhycoreAM335x contains the processor, RAM, and voltage regulators for the digital ICs. The VMS-20 is an AC to DC converter soldered directly onto the Powerboard. The remaining four PCBs were designed using Proteus Design Suite from Labcenter Electronics in North Yorkshire, United Kingdom. The Powerboard has the voltage regulators for the analog and digital voltages. The RF Transmitter produces the UWB pulses and the RF Receiver demodulates the pulses to baseband. The Mainboard has baseband automatic gain control, clock generation, and communication circuits. Earlier prototype designs were previously published [23].

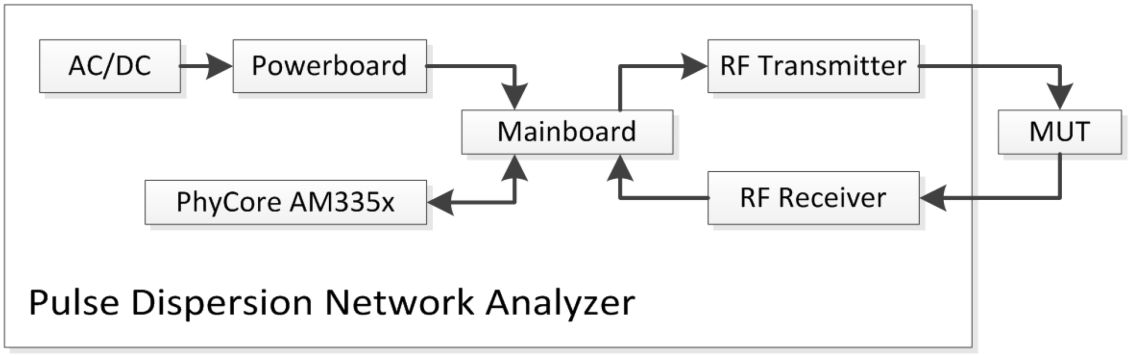

Fig. 20. Block diagram of the Pulse Dispersion Network Analyzer.

RF Transmitter

The primary function of the RF transmitter is to generate the UWB pulses. It consists of a glitch generator and pulse sharpener along with an amplifier and controllable attenuation illustrated in Fig. 21. There is also a switch to route the output directly to the RF for internal correction. The transmitter also has secondary functions for bandwidth control by designating pulse widths.

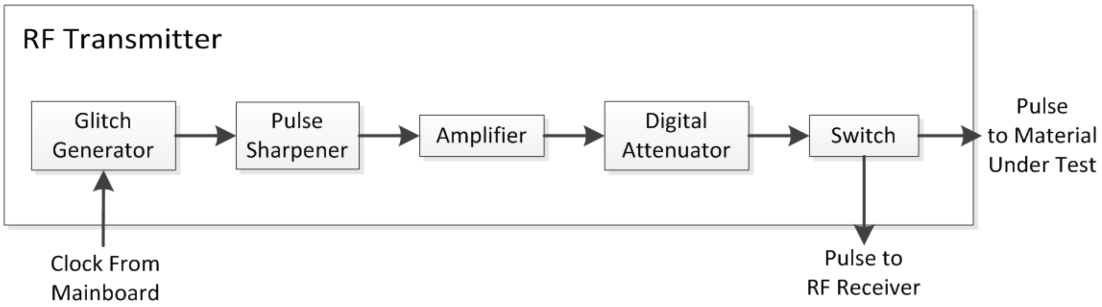

Fig. 21. Block diagram of the RF Transmitter.

Design

For a simple pulse generation circuit a self-resetting D flip-flop was designed with the output of the flip-flop routed to the reset terminal so a short pulse is generated when the flip-flop is clocked. The duration of this pulse will be equal to the propagation delay of the flip-flop after the addition of its rise and fall times. The MC100EP51 was selected as it is the fastest reasonably priced differential flip-flop available from Digikey. The total pulse width at 20% amplitude for the MC100EP51 is 660ps. Since this pulse width is larger than desired, a pulse sharpener needs to be added to the design. The flip-flop output logic levels can be 3.3 V PECL which falls within the range of the pulse sharper described below [24].

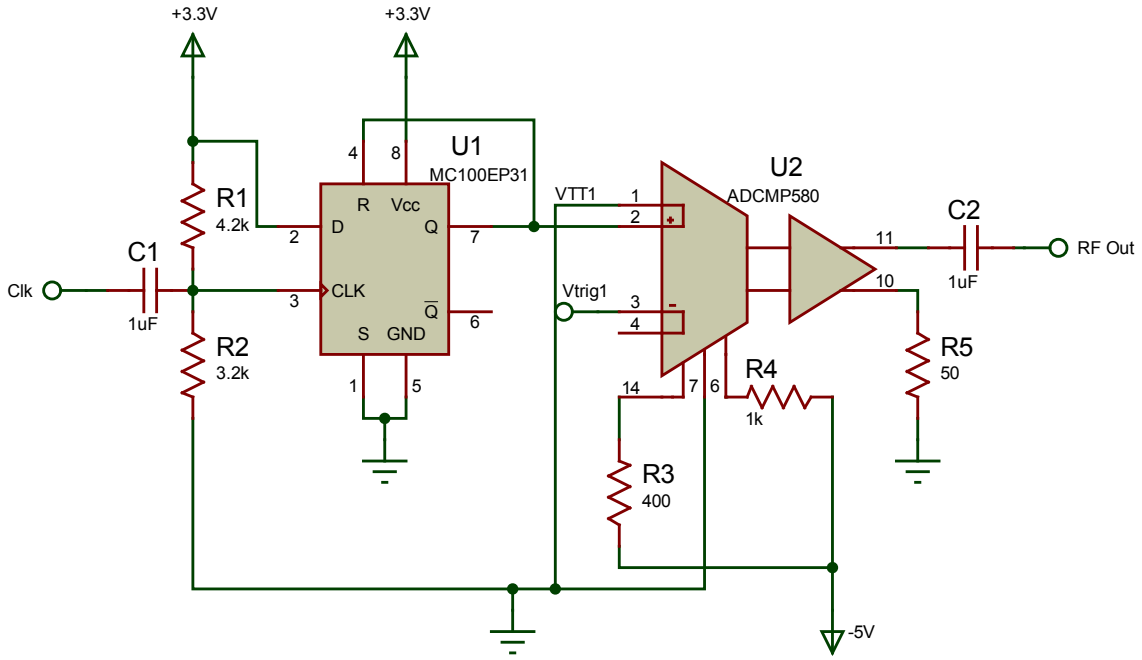

Fig. 22. Schematic of the pulse generation circuit.

In order to generate a pulse with faster rise times, a comparator is used after the flip-flop. The ultrafast silicon germanium ADCMP580 was selected as the comparator for its high performance at a low price point. If the outputs of the differential flip-flop directly drive the comparator, only the pulse rise and fall times would be decreased. Since it is equally beneficial to reduce pulse widths, a slightly different configuration was used. A single-ended output from the flip-flop along with a DC reference voltage were selected as the inputs to the comparator. The DC reference voltage, when produced by a DAC, can be raised or lowered to adjust the pulse bandwidth since the pulse from the glitch generator is triangular in shape. Care must be taken to reduce noise in the reference voltage as that will now affect pulse widths and jitter [25].

The CML amplitude from the comparator is 400 mV driving a 50 Ω load which is 5dBm of output power. To increase the amplitude a Skyworks SKY65017-70LF RF

amplifier was used on the output to the comparator. This amplifier provides 20 dB of gain with a gain flatness of ±1.5dB from 0 to 6 GHz. The SKY65017-70LF which dissipates 500mW of power was designed to be cascadable in wireless base stations, thus it has good stability. With the 400mV pulse single-ended output from the comparator, the amplified pulse with 20dB of gain should have an output power of 25dBm. However, the SKY65017-70LF's 1dB compression point is 20dBm. This operating condition means that the amplifier is being driven into compression. Compression of sinusoidal signals causes the peaks of the signals to be flattened which add higher frequency harmonic content. Compressing a pulse will cause the pulse shape to be squarer, which is actually a more desirable shape.

Pulse amplitude control is accomplished with a HMC624 digital attenuator from Hittite Microwave. While its 2dB of insertion loss is not ideal, it is a necessary tradeoff to obtain 30dB of amplitude control. This wide range of pulse amplitude allows for the RF Receiver to be designed to saturate at 30dB lower power levels. When measuring materials with high loss the pulse amplitude can be increased while maintaining the receiver's input power just under saturation. Using this technique, system dynamic range is effectively increased by 30dB.

For internal correction, vector network analyzers have multiple receivers to sample the transmitted and received waveforms simultaneously. In order to reduce costs and system complexity in the Pulse Dispersion Network Analyzer, only one receiver is used. Thus for internal corrections, the transmitted pulse must be switched directly into the receiver while bypassing the material under test. The switch was selected for low insertion and return loss, but more importantly isolation. Poor isolation will result in

frequency content from the transmitted pulse leaking into the receiver without passing through the material under test.

Layout

A four layer design was chosen to provide space for power planes, but keep costs low. The first inner layer is ground for microstrip transmission lines on the top. The second inner layer and bottom layer are used for power planes. Care was taken to minimize ground loops when adding power zones. Ground vias were added surrounding the RF traces to prevent the fringing microstrip fields from propagating through the substrate like a parallel plate waveguide. The primary method to reduce the EMI is the use of a board level shield covering the integrated circuits and traces. Grounded vias also surround the edge of the board to further reduce EMI.

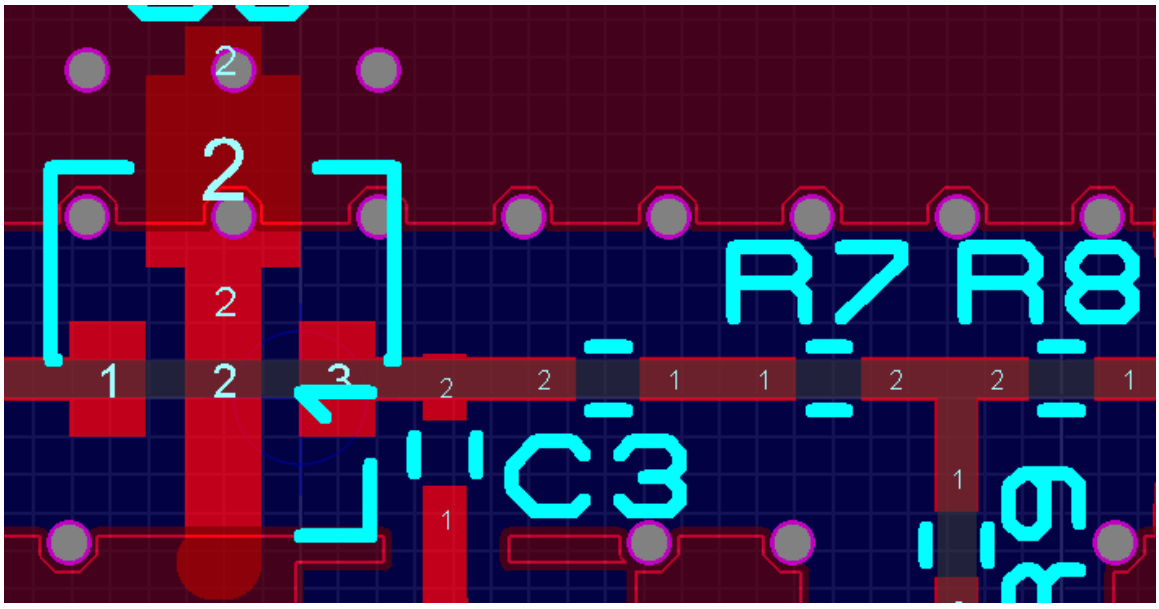

Fig. 23. A section of the RF Transmitter layout.

Rogers 4350 was chosen as the substrate for its low loss tangent and wide use in RF commercial applications. The Rogers 4350 has a relative permittivity of 3.48, and 10

mil substrate thickness was chosen to result in 50 Ohm line widths of 23 mils. This trace width is a good compromise between keeping the trace size small and providing ease of fabrication, as smaller line widths are more susceptible to impedance variations from manufacturing.

Performance

The PCBs were fabricated and assembled by Sierra Circuits in Sunnyvale, California. A populated RF Transmitter is shown in Fig. 24 with the EMI shield unpopulated. The RF Transmitter and RF Receiver were produced together on a panel to reduce manufacturing costs. The Ultraminiature Coaxial (UMC) cable can be seen in black providing the internal correction path to the RF Receiver.

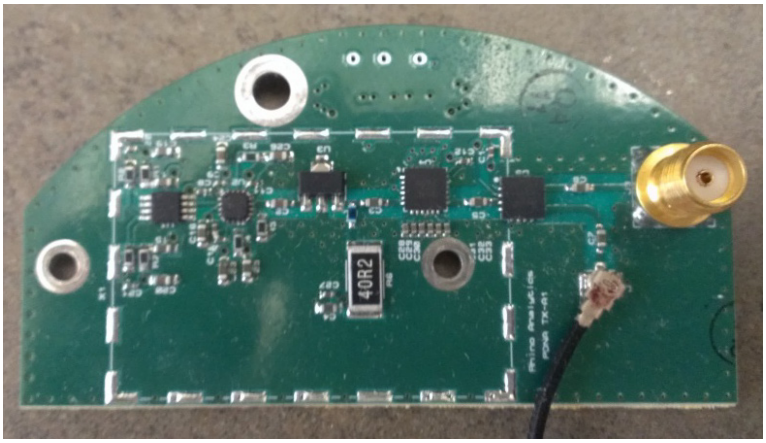

Fig. 24. The fabricated RF Transmitter.

The signals for each of the inputs to the pulse sharpening comparator are displayed in Fig. 25 . The blue trace is the output of the glitch generator with a pulse width of 600 ps. The overshoot and ringing at the end of the pulse is due to the impedance mismatch caused by the addition of the high frequency probe used to capture the signal. The green trace is the adjustable DC reference voltage.

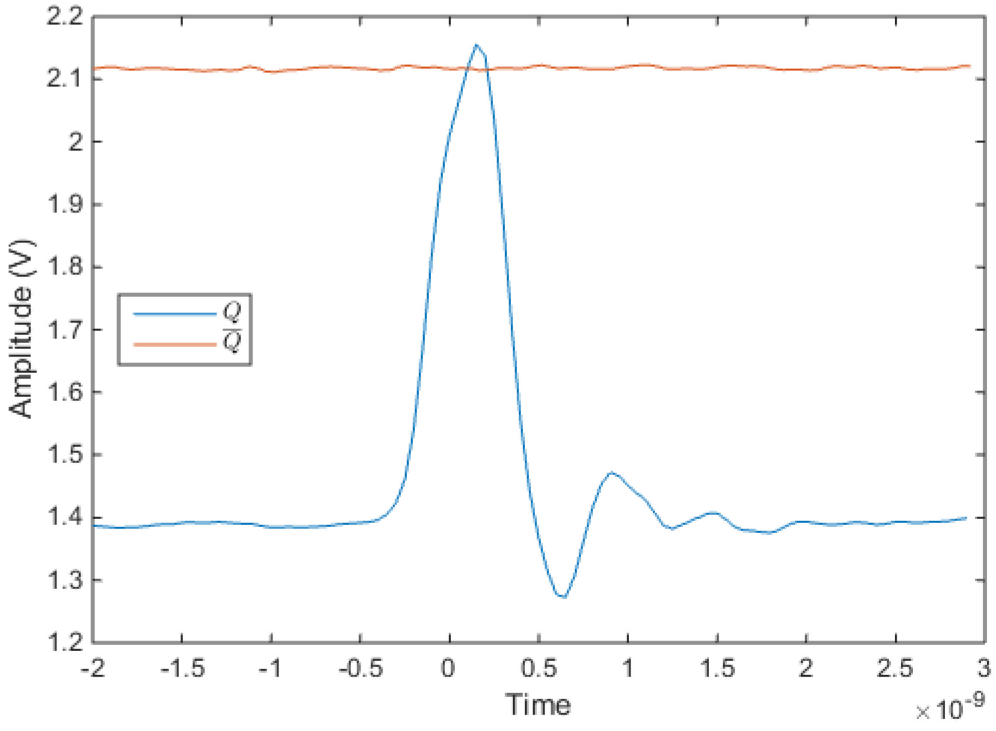

Fig. 25. Time domain inputs to the comparator.

Fig. 26 shows the out from the RF Transmitter as the comparator DC reference voltage is varied. The 80/20 pulse widths vary from 175ps to 850ps with 1.65 to 2.145 voltage levels. The comparator is specified with a minimum pulse width of 100 ps for digital communication purposes. However, in analog use, the pulse's amplitude begins to decrease at higher speeds. As the reference voltage approaches the peak of the flip-flop output, the pulses begin to exhibit jitter in the pulse width. Electromagnetic interference and noise on the reference voltage become more influential factors and averaging must be increased. Multiple capacitors covering several orders of magnitude are placed in parallel on the reference voltage trace to reduce the noise.

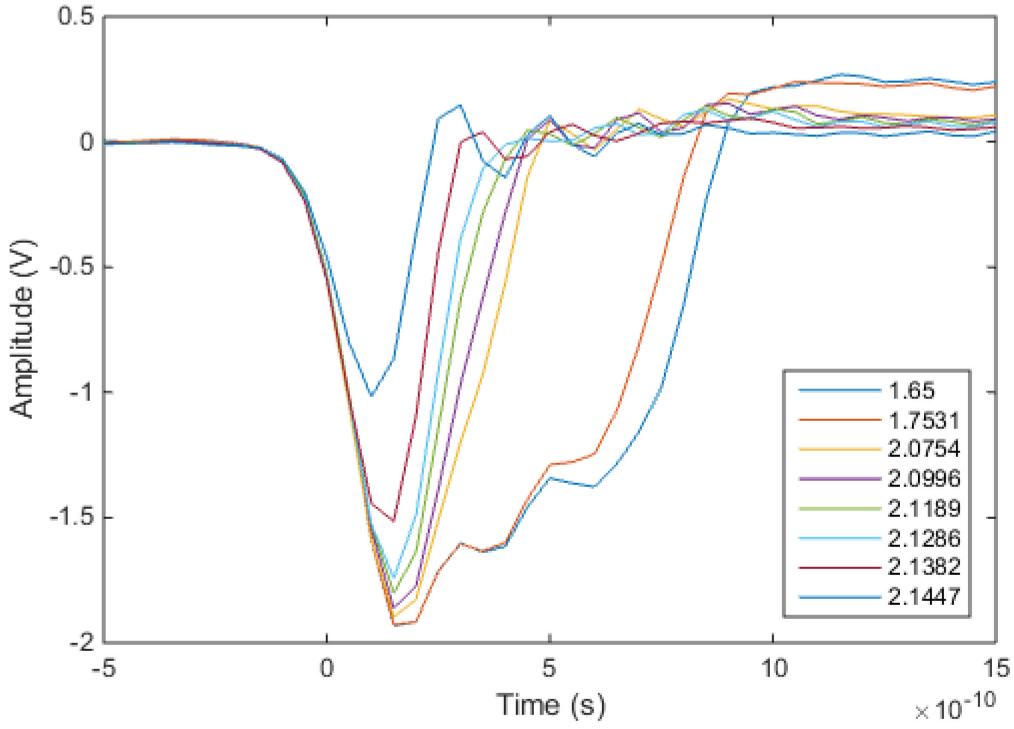

Fig. 26. Output pulse widths with varying DC reference voltages.

The frequency spectra of the pulses in Fig. 26 are shown in Fig. 27. The 2.00 V trigger level's spectrum is close to that of a comparator triggered differentially by the flip-flop instead of the DC reference voltage, having a first null at 2.1 GHz and a 1.4 GHz 10 dB bandwidth. The 2.18 V trigger level's spectrum is significantly flatter with a first null that is beyond the range of the 5 GHz LeCroy Oscilloscope and has a 3.5 GHz 10dB bandwidth. This pulse more than doubles the bandwidth of the pulse generator, but also sacrifices 10 dB in output amplitude. However, the pulse width is now tunable and could offer increased amplitude with decreased bandwidth if desired. It is also possible to use the frequency content in the second maximum of the wide pulses.

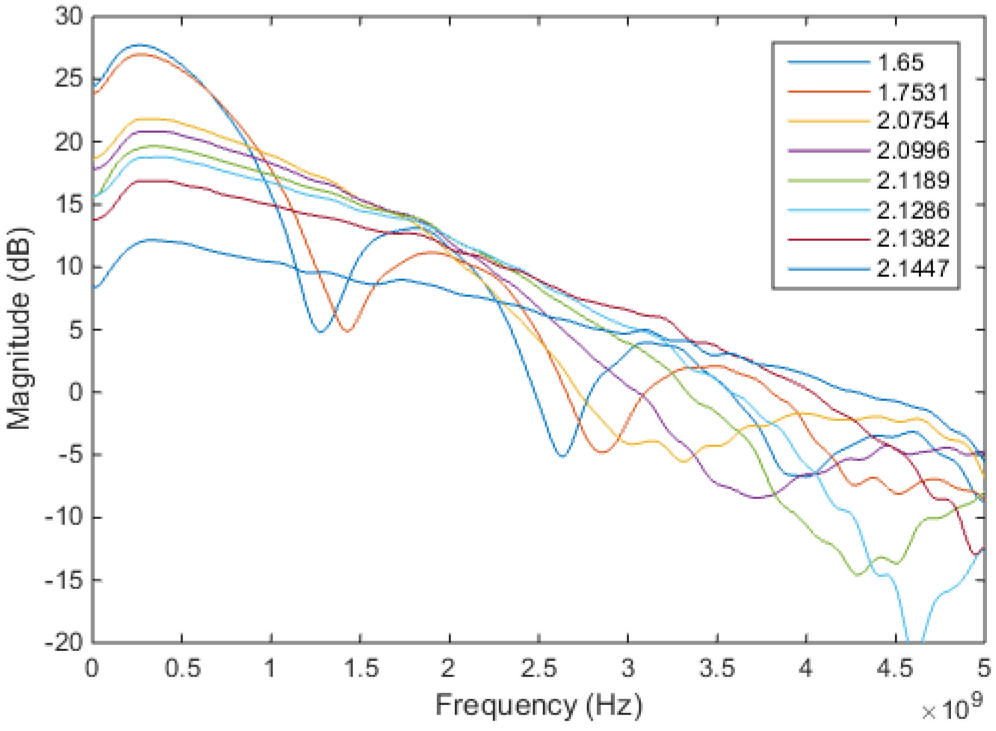

Fig. 27. Frequency spectrums of the variable pulse widths.

RF Receiver

The primary function of the RF Receiver is to down convert the RF signal to baseband using equivalent time sampling. The portion of the receiver which does the down conversion is called the sub-sampling circuit. The receiver has two input ports one for the material under test and one for the internal correction, which connects directly to the transmitter with an ultra-miniature RF cable. This internal path contains a fixed attenuator to reduce the amplitude of the calibration pulse so as to not saturate the receiver. The demodulated low frequency signal is also amplified and buffered for processing on the Mainboard.

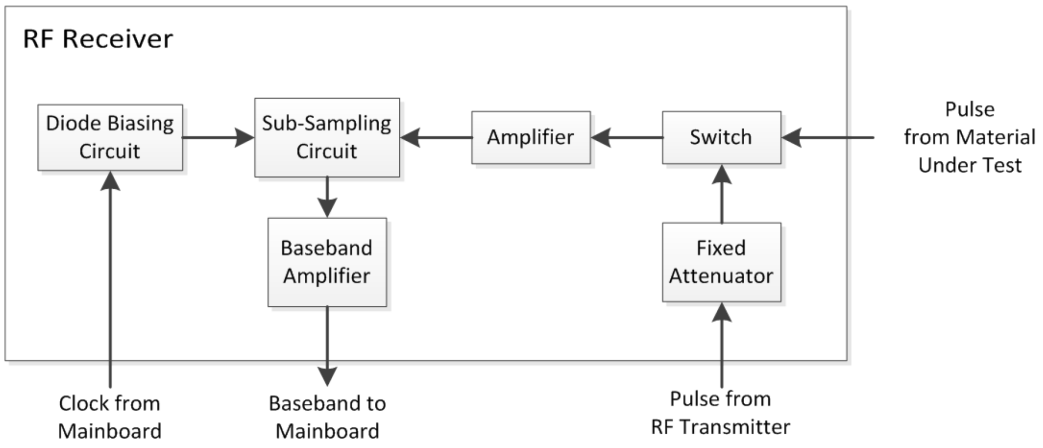

Fig. 28. Block diagram of the RF Receiver.

Design

The sub-sampling circuit implements the sample and hold function necessary for equivalent time sampling. This process is described by Jean [12]. Equivalent time sampling uses two independent frequencies to control the timing of the trigger signals of the source and the sampling circuit. In the initial prototypes, the source timing frequency is 4 MHz. The sampling frequency is chosen to have a difference frequency of 64 Hz which results in the extended time factor as defined in (15).

$$\frac{f_0}{\Delta f} = \frac{4\ \text{MHz}}{64\ \text{Hz}} = 62500 \tag{15}$$

This extended time factor means that frequency content at 3.5 GHz is scaled down to 56 kHz and can be sampled by an ADC with a minimum sampling frequency of 112 kS/s. The extended time factor can be controlled to provide a tradeoff between the receiver's bandwidth and the FFT frequency resolution. For example, a 120 kS/s ADC and a 62500 ETF with a 1024 point FFT has a frequency resolution of 7.3 MHz with 3.75 GHz of bandwidth. If the ETF is increased to 100000, the bandwidth is increased to 6

GHz, but the frequency resolution has also been increased to 11.7 MHz. The larger frequency resolution means that any peaks, nulls or other features identified will have a frequency error of ± 5.85 MHz. This error could be mitigated by expanding the number of points in the FFT along with the associated computational time and cost.

The sub-sampling circuit shown in Fig. 29 is based on Zhang [26] which offers an improvement upon Han [27] by using a fully balanced structure. However, in Zhang's work the sampling circuit was triggered using a strobe step generator connected to the sampling switch circuit through a wideband balun. The circuit produces a sampling signal that has a 100 ps gating duration, but it also introduces significant ringing after the triggering pulses. This ringing response could inadvertently bias the diodes to an ON state and introduce error into the sampled voltage.

The triggering pulses for the sub-sampling circuit in the present design are generated by an analog comparator, which already has a balanced output. The same comparator that was chosen for the pulse generator is used to trigger the sub-sampling circuit. The comparator's balanced output eliminates the need for a balun, which are difficult to design for large bandwidths. A high speed ECL flip-flop triggers the sub-sampling circuit comparator as described above for the pulse generator. Here both the inverting and non-inverting outputs of the comparator are used. Blocking capacitors are placed on both outputs to maintain circuit symmetry, although technically only one is required to remove the DC bias in the inverting output.

Fig. 29 shows the sampling circuit used in this work. HSMS-286C Schottky detector diodes were chosen for their low series resistance (6 ohms) and high sensitivity. R3 and R4 are used for impedance matching. C1 and C2 are the RF holding capacitors

which form an RC discharge circuit with the diode resistance. The RF time constant is set at 36 ps to provide a small sampling window. The inside resistors and capacitors (R1, R2, C3, C4) also form a RC discharge circuit to hold the voltage for the intermediate frequency (IF). The IF time constant is set to approximately 810 ps so as to maintain the voltage level from sample to sample.

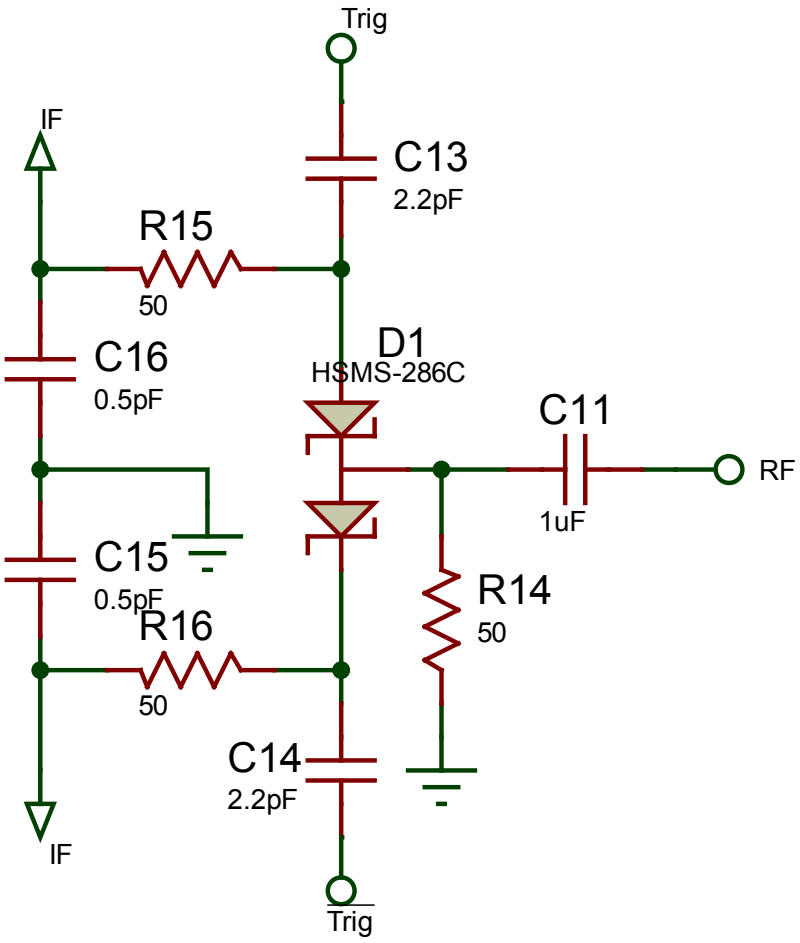

Fig. 29. Sub-sampling circuit schematic.

The sub-sampling circuit needs two differential pulse signals to forward bias the sampling diodes at the proper sampling time. These differential pulses are generated with a self-resetting flip flop and comparator as in the RF Transmitter.

Layout

The PCB layer stack of the RF Receiver is replicated from the RF Transmitter. It is a four layer board with 10 mil Rogers 4350 between the top layer and inner 1. The other dielectric substrate is FR4 and the total board thickness is 59 mils. Ground vias were also used around the microstrip traces and around the board edge with a board level shield around the integrated circuits.

Performance

The RF Receiver was fabricated and populated in a breakout panel alongside the RF Transmitter. Combining the two PCBs into one panel significantly reduced manufacturing costs. A populated RF Receiver is shown in Fig. 30. The outline of the EMI shield can be seen, but remained unpopulated for picture clarity.

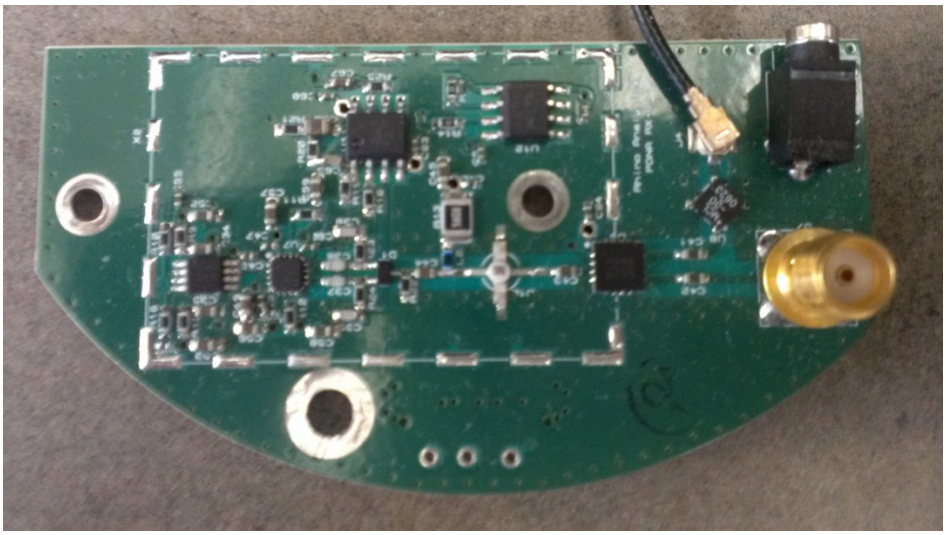

Fig. 30. The fabricated RF Receiver.

Fig. 31 shows the outputs of the diode biasing circuit to trigger the sample and hold mechanism in the sub-sampling circuit. The width of these trigger signals is approximately 400 ps. This width can be adjusted using the same manner that the

transmitted pulse width can be controlled. As the diode triggering signals reduce in length, the overall amplitude of the down sampled signal will also reduce resulting in increased conversion loss.

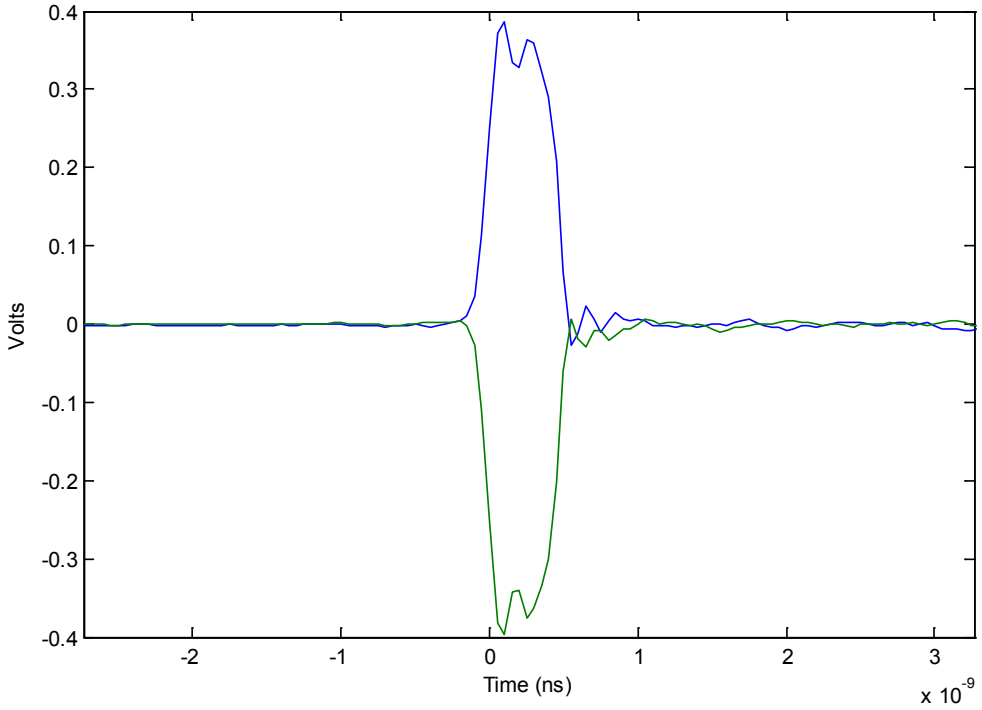

Fig. 31. The differential diode biasing signals.

A comparison of the extended time sampled pulse from the sub-sampling circuit and the pulse from the RF Transmitter is shown in Fig. 32. The pulse from the RF Transmitter is in red, as measured by a LeCroy Wavemaster 8500 oscilloscope, while the sub-sampled pulse from the RF Receiver is in dotted black, as measured with a Yokogawa 1640 oscilloscope. The sub-sampling circuit output demonstrates good agreement with the transmitted pulse in amplitude and the correct expected extended time scale. Some small error can be noticed before the beginning of the pulse caused by the

start of the triggering. This error is systematic and can be corrected with an internal calibration or omitted using time gating.

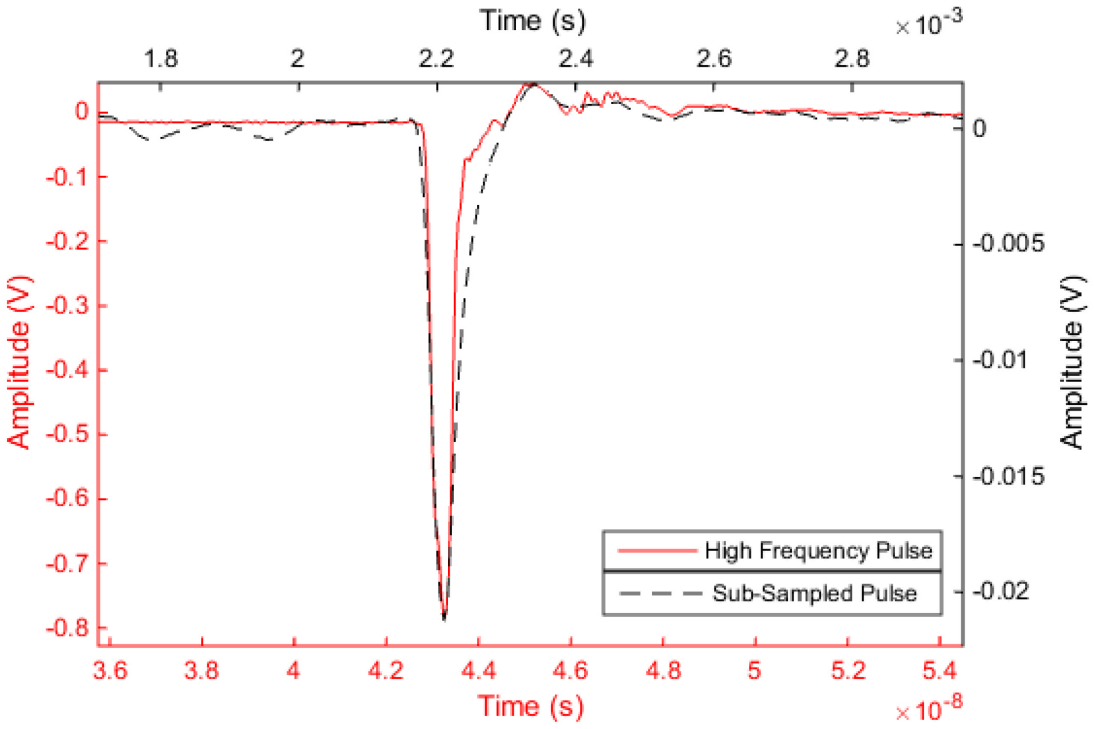

Fig. 32. Comparison of the high frequency pulse versus the sub-sampled pulse.

To test the RF Receiver's input power capability, the amplitude of an undispersed pulse was varied using external attenuators. The peak voltage of the sub-sampled pulse was then plotted in dBm and is displayed in Fig. 33. Note the system impedance is 50Ω common to most laboratory equipment. From the figure the 1dB compression point is approximately -1.5 dBm with a conversion loss of 9 dB. This conversion loss is a result of the diode load resistors as well as the forward biasing voltage. The bias voltage could be increased without significant modifications to the circuit.

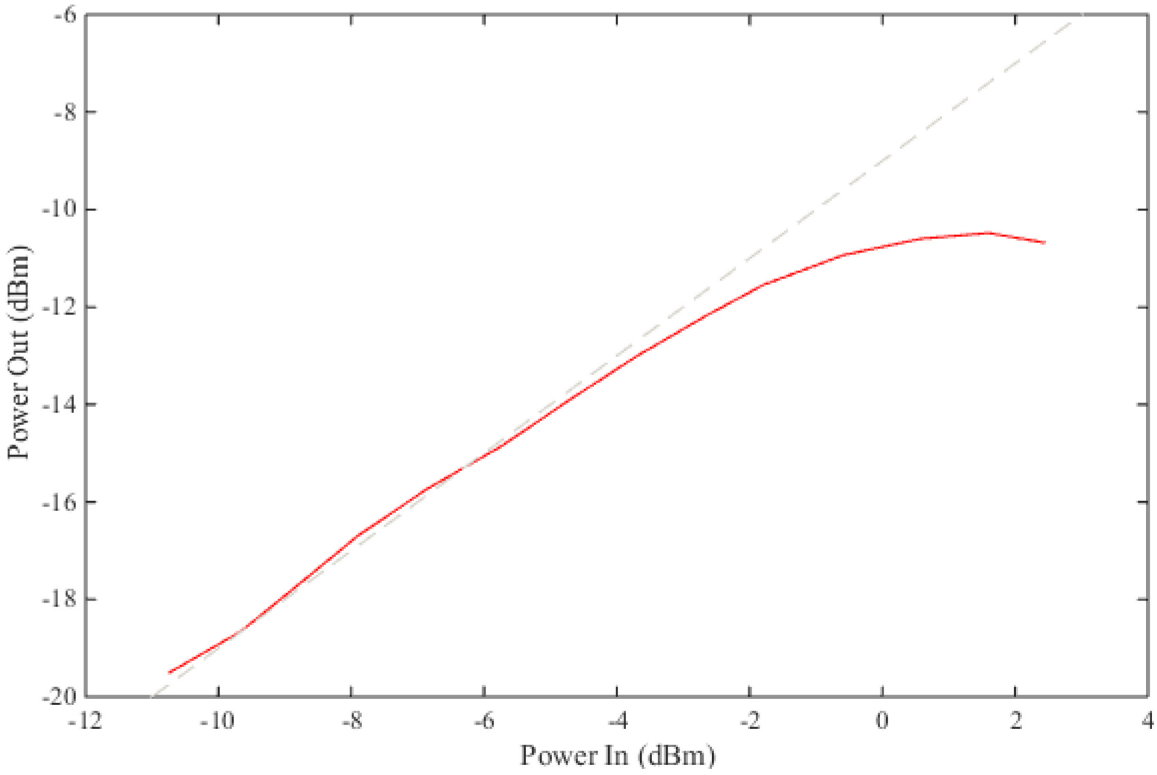

Fig. 33. Sub-sampling circuit power compression.

The extended time factor was varied from 100,000 to 1,500,000 resulting in the time domain waveforms shown in Fig. 34. In the figure, the x axis is samples from the ADC instead of being converted into seconds to illustrate the spreading of each pulse. The amplitude of the received pulse slowly decreases due to the high pass filtering of the bootstrap amplifier and could easily be modified for larger ETFs. As the extended time factor increases, noise due to clock jitter also increases, thus more averaging is needed. The frequency response of the pulses from Fig. 34 are shown in Fig. 35. The degradation in low frequency response can clearly be seen. The capacitors in the bootstrap amplifier can be increased to remedy the low frequency performance if the system is operated with large extended time factors.

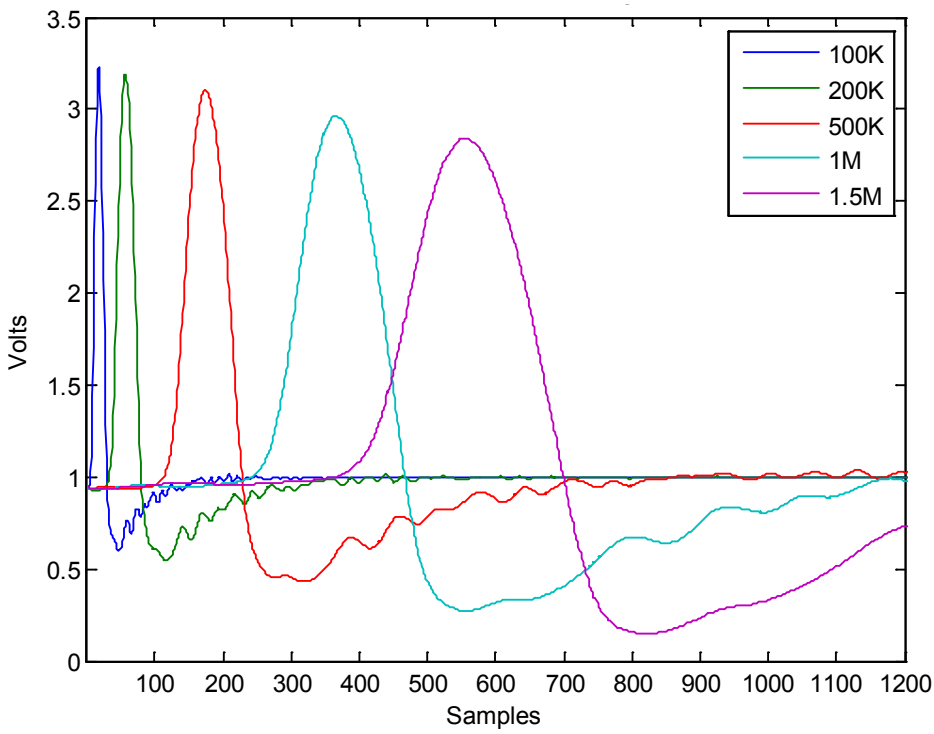

Fig. 34. Raw time domain signal of sub-sampled pulses with different extended time factors.

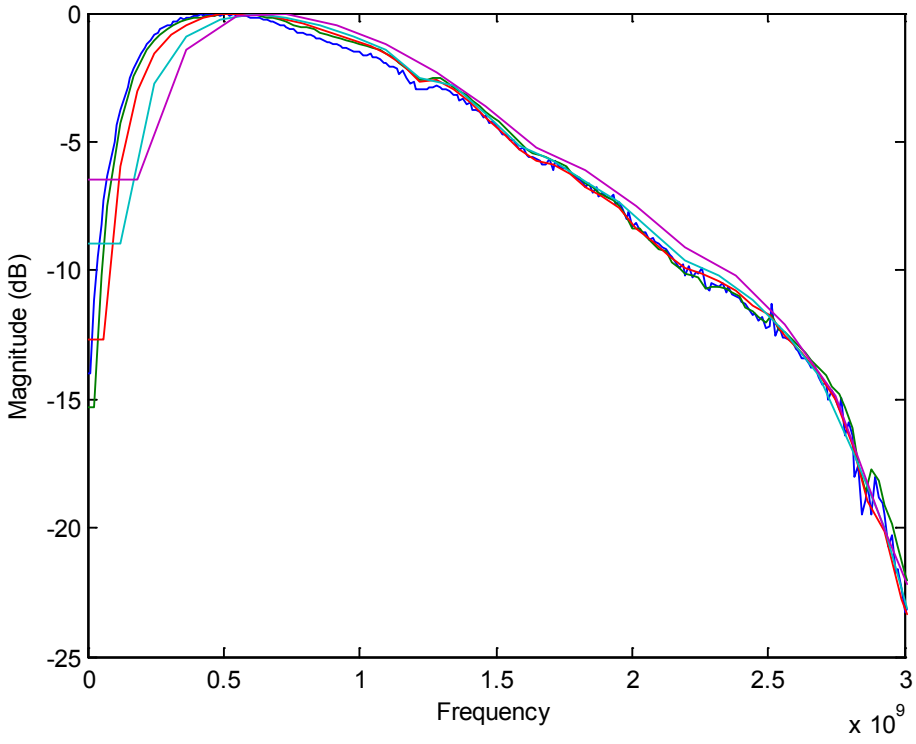

Fig. 35. Spectral response of pulses with varying extended time factors.

Mainboard

The Mainboard contains the circuits for the automatic gain control, clock generation, and communications. There are four surface mount connectors for the Powerboard, RF Transmitter, RF Receiver, and Phycore-AM335x which mount to the Mainboard with soldered standoffs.

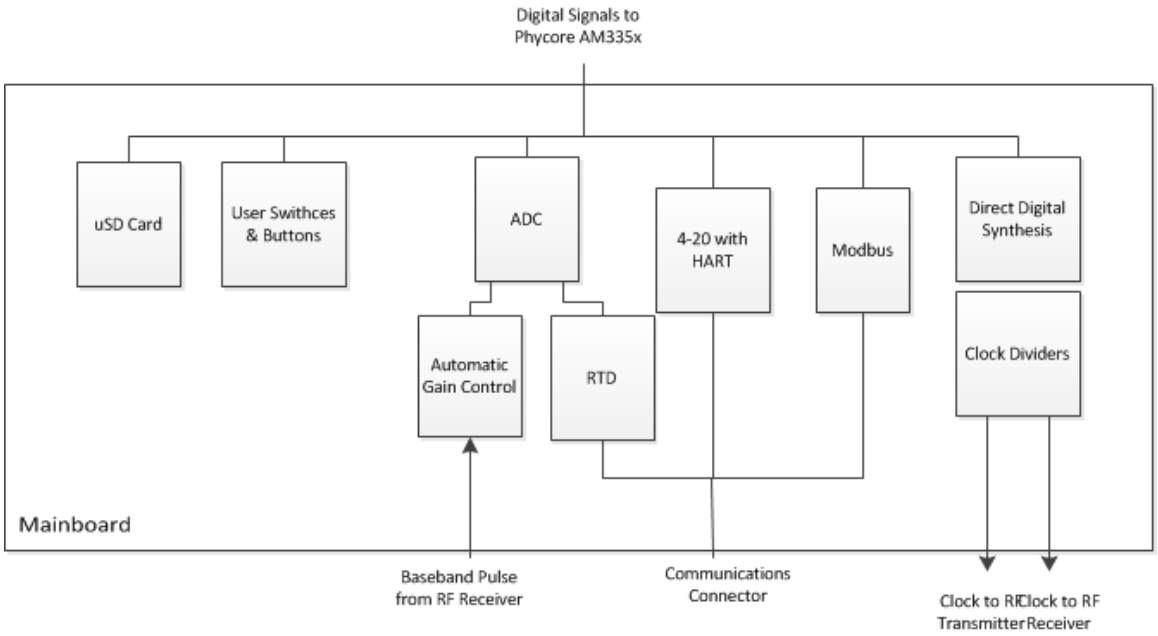

Fig. 36. Block diagram of the Mainboard.

Clock Generation

Two differential clocks are needed to control the RF Transmitter and Receiver. Phase noise along with frequency resolution and accuracy are key specifications. As an example, for 1% frequency accuracy with a pulse repetition frequency of 5MHz and extended time factor of 500000, the clocks frequencies must be accurate to 0.1Hz. This accuracy is equivalent to 0.02ppm which is 3 orders of magnitude greater than crystal oscillators and 2 orders of magnitude for phase lock loops. The chosen solution for clock generation is direct digital synthesis.

The AD9958 is a dual channel DDS IC with 0.12Hz frequency resolution. Direct generation of the pulse repetition frequency requires physically large filters to eliminate the harmonics. These harmonics, if not properly filtered, will introduce large amounts of clock jitter. The alternative design is to use clock dividers and synthesize a frequency much higher than the pulse repetition frequency. Clock dividers can then be used without an increase in clock jitter [28]. The system default uses a 120MHz center frequency with two differential 7^{th} order 135 MHz low pass Chebyshev filters. This center frequency allows for pulse repetition frequencies as low as 3.75 MHz.

Signal Conditioning

A dedicated analog-to-digital converter was used instead of the AM3359 to obtain a better signal to noise ratio as well as dynamic range. The low power, 16 bit, 1 MSa/s, dual unipolar input ADS8330 from Texas Instruments was used. It communicates using an SPI channel also multiplexed with the FLASH memory on the PhyCORE-AM335x.

The control board has a two stage operation amplifier circuit to maximize the dynamic range of the analog-to-digital converter for pulse receiver's output. This circuit uses a 10 bit digital to analog converter (DAC), the DAC7574 from Texas Instruments, to set the DC voltage level, and a 200kΩ 8 bit digital potentiometer (pot), the AD5280 from Analog Devices, to control the gain. A voltage divider was used between the DAC and the non-inverting input of the second opamp stage so that the output DC offset has zero gain. When the pot's resistance between the wiper and "low" terminal is set to 10kΩ the circuit has unity gain. The output of the operational amplifier is approximated in (16). Both the DAC and pot are controlled via an Inter-Integrated Circuit (I^2C) bus. This DAC

also produces the DC reference voltages needed to set the trigger level for the comparators on the RF Transmitter and Receiver.

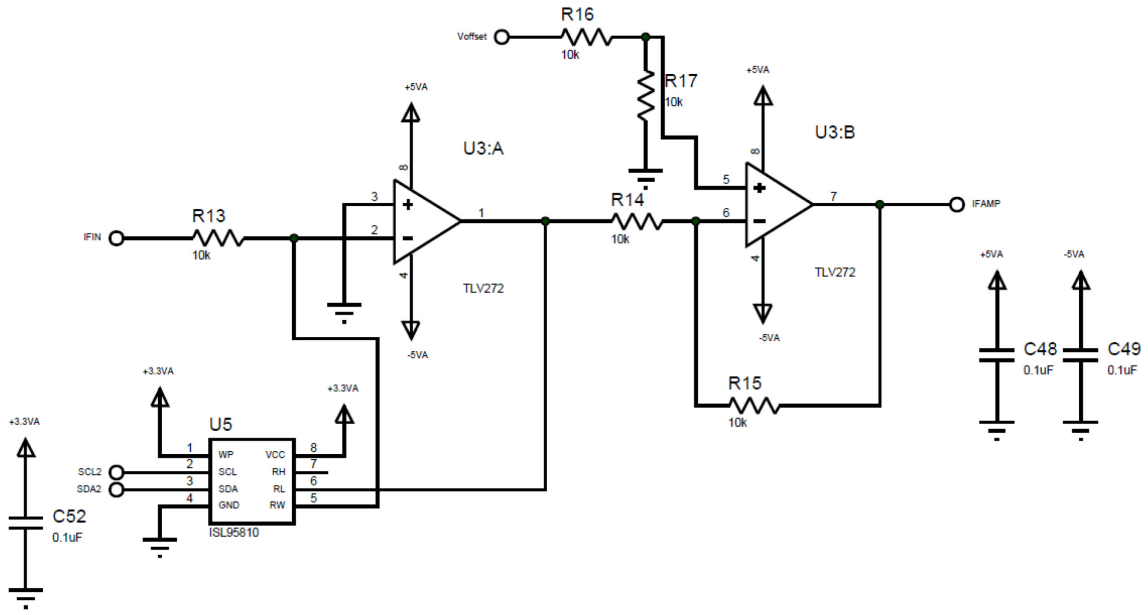

Fig. 37. Intermediate frequency signal processing circuit schematic.

$$IF_{out} = IF_{in} * \frac{R_{pot}}{10k} + V_{DAC} \tag{16}$$

Communications

The Mainboard has two industrial communication protocols: Modbus and a single 4 to 20 mA current loop with the Highway Addressable Remote Transducer (HART). The Modbus physical protocol uses 2-wire RS-485. Both Modbus signal lines along with its ground are magnetically isolated with 15kV ESD protection.

Layout

The Mainboard required a six layer stack due to the density of the traces and power planes. Two of the inner layers were used as power planes with another inner

layer used as a ground plane. Traces were then contained to the top and bottom plus the last inner layer. Board level ground shields for EMI were used around the clock generation circuits as well as the ADC and AGC circuits.

Performance

Fig. 38 shows the fabricated and populated Mainboard also manufactured and assembled by Sierra Circuits. The EMI shields have not been populated to display the circuits underneath them. The three notches in the top of the PCB are for the SMA cables to pass through. The PCB functioned as designed with minimal clock jitter from electromagnetic interference

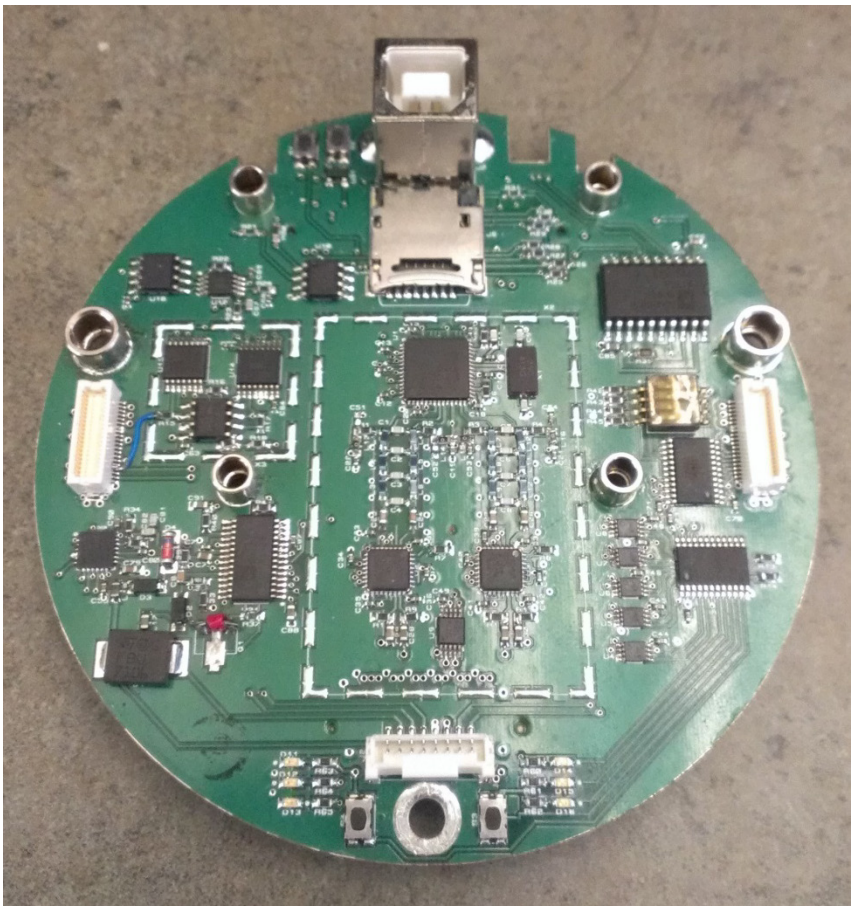

Fig. 38. A fabricated Mainboard.

Powerboard

The PDNA must accept 120V AC as well as 12-24V DC. There are five different positive and negative analog voltages along with three digital voltages. The design of the analog voltages favors performance and efficiency over cost. The surface area available to the Powerboard is reduced due to the instrument side conduit extrusion in the Adalet enclosure.

The analog voltage supplies use RF low dropout regulators from Texas Instruments designed for high-accuracy and high-precision instrumentation. Their ripple rejection is 82dB for low frequency noise and greater than 55dB for RF noise. To increase their efficiency and decrease board temperatures, DC-to-DC step-down switching regulators were used to provide the input voltages to the linear regulators. The voltages of the buck regulators were set to be half a volt above the output voltage of the linear regulators. The half volt increase was chosen because of the 450mV maximum specified dropout voltage of the linear regulators.

The positive analog voltages use buck regulators whereas the negative analog voltages use an inverting buck-boost converter. All switching frequencies are set at 500kHz which is the same frequency used for the ADC.

Performance

The Powerboard in Fig. 39 was fabricated and assembled by Sierra Circuits. The left side of the PCB is the digital power supply, with the positive analog supplies in the middle, and the negative analog on the far right side. The PCB is not completely circular due to the restrictions of the Adalet enclosure. The pads for the three RF shields can be seen in the figure, but remain unpopulated for the visual presentation.

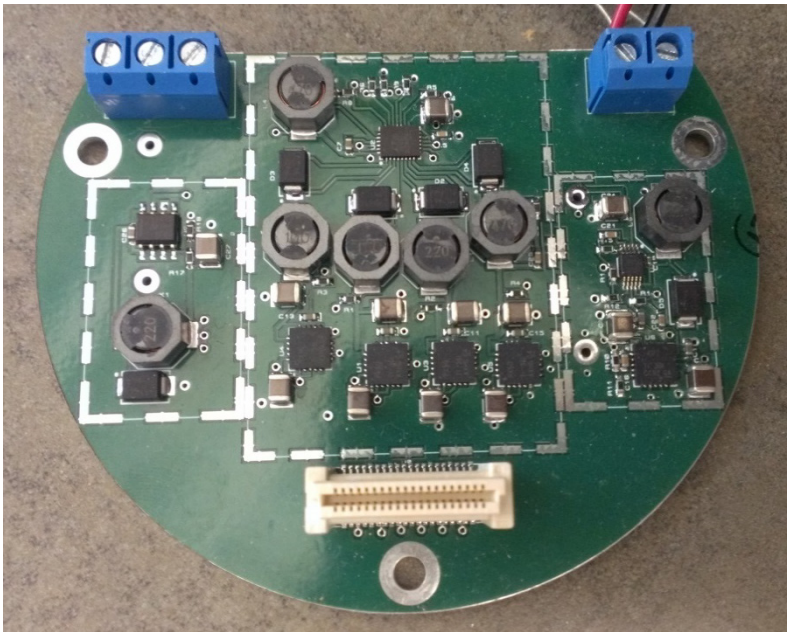

Fig. 39. A fabricated Powerboard.

The signals in Fig. 40 compare the five volt analog and digital power supplies as captured by an oscilloscope with AC coupling. The digital power supply contains 500 kHz switching frequency noise not present in the analog supply due to the inclusion of the additional linear voltage regulators. These linear regulators increase the system's size and cost, which is further discussed in Chapter Five.

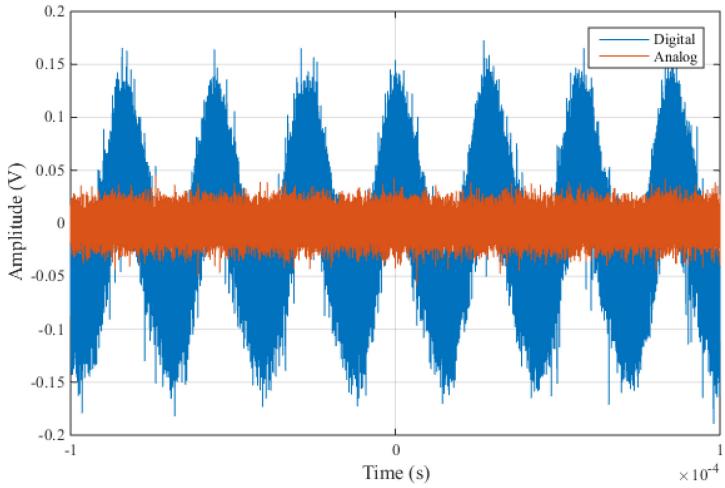

Fig. 40. Five volt digital and analog rails measured with AC coupling.

Processor

The Pulse Dispersion Network Analyzer requires a processor capable of implementing many embedded digital signal processing techniques in a reasonable time. Some of these techniques include fast Fourier transforms, training of neural networks, principal component analysis, filtering, and multivariable linear regression. The processor needs enough RAM and memory storage for internal corrections and process calibrations. To meet the processing and cost requirements an ARM processor was chosen. In 2011 Texas Instruments released the AM-335x processor line targeted for embedded industrial applications with a 10 year production volume commitment. These microcontrollers contain modules for additional industrial communication protocols such as Profibus, Profinet, and Ethernet/IP. While these protocols are currently not specified in the PDNA, this microcontroller could allow for additional communication features if needed.

To integrate the AM335x in the system, a third party module could be purchased or a module could be developed in-house. It was estimated that internal development of the module would take a minimum of 8 months and manufacturing costs per unit would have to be under $50 to break even. Thus purchasing a system on module (SOM) from a third party was a more economically viable approach. SOMs from Phytec, Variscite, and Critical Link were evaluated for use in the PDNA. The Phycore-AM335x from Phytec in Mainz, Germany was chosen over the other manufactures because its size was the only one which could easily fit inside the specified enclosure. Phytec also provided full schematics which were useful in development.

The supporting memory components of the SOM are 512 MB of DDR3 RAM, 512 MB of NAND-Flash, and 4 KB of EEPROM. The following is a list of features used

from the SOM: 2 Serial Peripheral Interface (SPI) with chip select lines, two UARTs including one with flow control, one I^2C bus, one high speed universal serial bus (USB), one four-bit Secure Digital (SD) bus, one PWM output, and six general purpose input output (GPIO) pins. TI's Pin Mux Utility was used to carefully verify availability and design of all necessary buses and pins. Some pin multiplexing combinations are banded together in subsets so not all possibilities are simultaneously available. The most exotic combinations were SPI1 set to IO subset seven and UART2 set to IO subsets one and five. More direct PCB trace routing was also a major factor in pin selection.

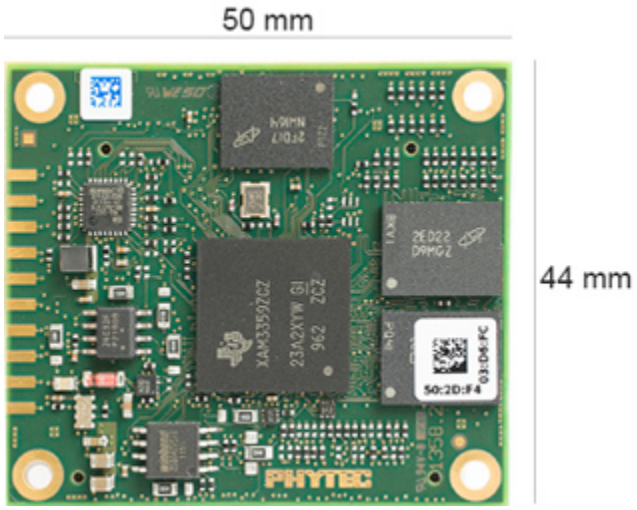

Fig. 41. The Phycore AM335x processor.

CHAPTER THREE

Software

The complete software suite for the PDNA has four components: the firmware, USB drivers, USB application program interface (API), and graphical user interface (GUI) as displayed by Fig. 42. This chapter is divided into three sections most of which describes the firmware. The first section details parts of the firmware specific to the AM3359, the second section describes the digital signal processing (DSP), and the last section includes the industrial and USB communications as well as the GUI.

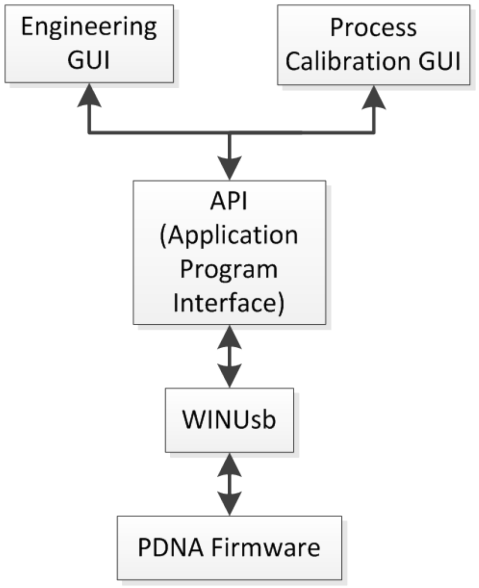

Fig. 42. Block diagram of the software components.

The AM3359 firmware is composed of several C software libraries developed in Code Composer Studio 6.0.1 compiled with TI's ARM compiler v5.1.7 as well as the GNU Compiler Collection v4.7.4. Several of the libraries were modified from Texas Instrument's StarterWare software package v02.00.01.01. Other third party libraries

which were ported to the ARM include FatFS, MiniINI and FreeModbus. The StarterWare was the basis for the device abstraction layer, system configuration, and USB libraries. FatFS provided the file system used for the SD card, MiniINI is used to store system variables on the SD card, and the FreeModbus library is used for the Modbus communication stack.

WinUSB is used as the Windows USB driver with the API written in C++ and compiled to a dynamic-link library (DLL). The GUI is written in MATLAB and compiled as an x64 executable for Windows 7.

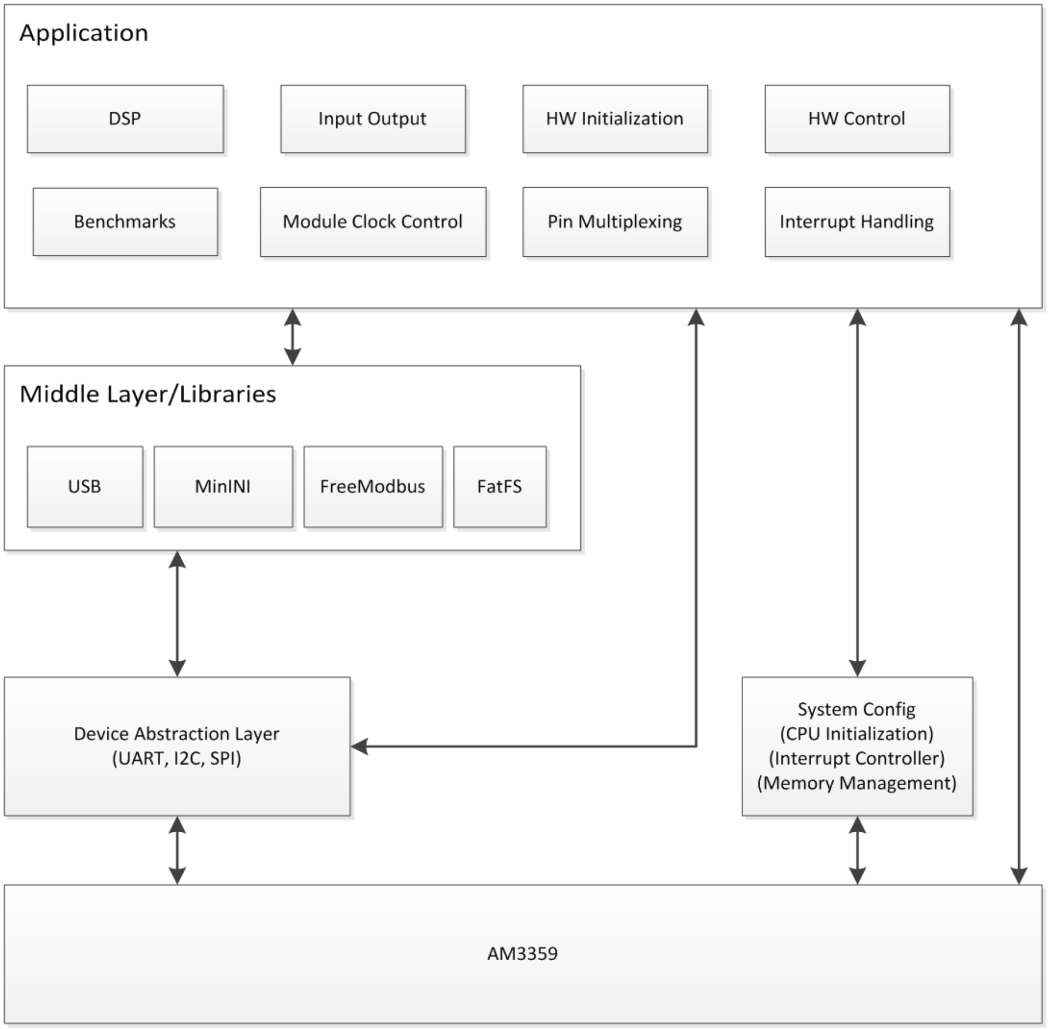

Fig. 43. Firmware organizational chart.

Hardware Control

The AM3359 contains the ARM Cortex-A8 processor which uses the 32 bit ARMv7-A architecture. Fig. 44 shows the functional block diagram for the AM3359 with the additional peripherals, memory controller, interconnect busses, and the programmable real-time unit and industrial communication subsystem (PRU-ICSS). The PRU-ICSS contains two RISC cores intended to be used for several different industrial protocols. During development a C compiler for the PRU-ICSS was not available and additional industrial protocols are not specified for the current PDNA. The PRU-ICSS is reserved for future system revisions.

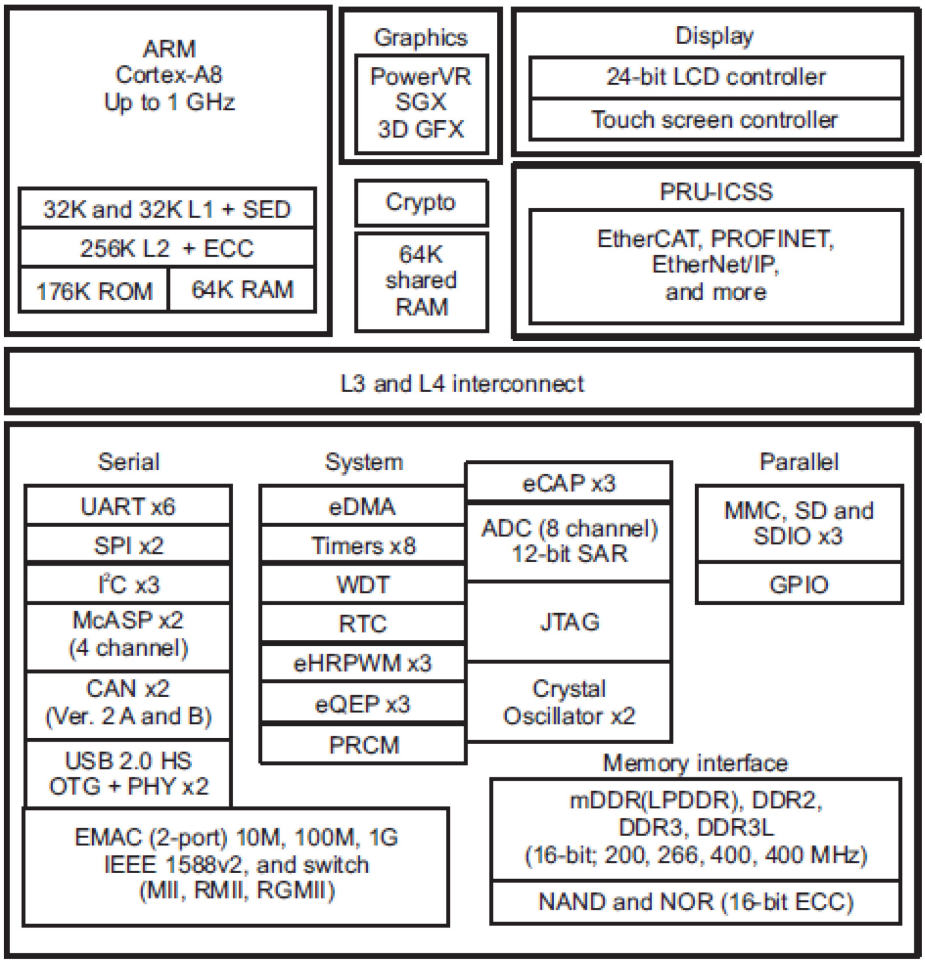

Fig. 44. AM3359 functional diagram.

Starterware

The StarterWare is broken into four main libraries which are separately compiled and included in the main application by the linker. The drivers library is the device abstraction layer, which contain the APIs for the peripheral modules. The system library provides functions for control of the clocks, memory management unit, interrupts, and CPU initialization. The utilities library is for miscellaneous support such as console commands, delay, performance and other timer functions. The USB library is used in the middle layer providing the stack for the generic bulk device class as well as others not utilized.

Several noteworthy modifications were made to the Starterware package. The first important change was to switch the connection type to 2.0 from 1.1 in the USB library as well as increase the USB packet size to 512 bytes. These changes cause the USB host to use high-speed operation instead of full-speed and greatly increase bulk transfer transmission rates. Another critical modification was disabling the automatic cache flushing in the MMCSD functions. Since the cache is being used, but direct memory access is not, the automatic flushing was preventing the reception of SD card packets.

The following paragraph summarizes the peripheral use from the drivers library for hardware control and initialization. Three timers are used to determine the Modbus end of frame, general software delays, and for benchmarking performance. Both SPI ports control the registers for direct digital synthesis clock generation, analog to digital conversion, 4 to 20mA current loop, and flash memory. Several GPIO pins control the ADC conversion timings and clock synchronizations. The SD card is used to store system and calibration variables along with data sampled for the calibration. The real

time clock is used to check for internal corrections. Only one I2C bus is used to control a multitude of hardware functions, from adaptive gain control, system temperature, user buttons and LEDs, RF pulse widths, and AM3359 voltages. The UART is used for the Modbus commination.

Memory Management

The memory map for the ARM Cortex-A8 is designated by the linker command script. The software stack is allocated to the 64kB of internal RAM using the on-chip memory controller to allow the stack to have the shortest access time. The program code along with initialized global and static variables are placed low to high in the DDR RAM as well as included in the binary distribution. The heap has 384MB allocated from high to low starting with the last available DDR address.

In order to utilize the Cortex-A8 cache, the memory management unit must be enabled. The master page table is initialized with a mapping the DDR, internal RAM, and shared peripheral registers. Of great importance to the map is the designation that the peripheral memory cannot be cached. The firmware currently does not make use of direct memory access (DMA) to simplify initial development. However restructuring the firmware for USB DMA would offer a large improvement in USB transfer times. Since an 8kB array is transferred in 1.1ms, optimization of the USB memory access was deemed a low priority task.

Boot Sequence

The AM3359 has a ROM for initialization preprogrammed by Texas Instruments. This initialization code reads four SYSBOOT pins to determine the order of external memory sources to look for executable code. The default boot order for the PDNA is the

NAND flash then the SD card, but this order could be changed by repopulating pull up and down resistors on the AM335x SOM. The ROM boot initialization code then loads itself and the application into the two blocks of internal RAM. However the total size of the RAM is 127kB with only 109kB usable once the initialization code is included. Since this size is significantly less than the actual program size a two stage boot process must be implemented. This 109kB or less code shall be defined as the bootloader.

The bootloader's function is to program the necessary registers to initialize the DDR3 RAM then load the main application into that RAM. A secondary task is to program the core voltage provided from the TPS65910 PMIC using the I2C bus. The ARM cortex-A8 voltage must be raised from 1.1 volts to 1.2, 1.26 or 1.325 volts in order to increase the clock speed from 500 MHz to 720, 800 or 1000 MHz. Currently the AM3359 on the Phycore SOM does not support 1GHz operation whereas AM3358 ICs do support it. After the core voltage is set, the bootloader sets the phase lock loops (PLLs) for the memory protection unit, ARM core, peripherals, and DDR. Then the various L3 and L4 interface clocks must be enabled with their respective power domains. Once the power domains have been fully activated then the DDR3 can finally be initialized and configured.

The main application is then be loaded from either the NAND flash or the SD card. Loading the application from the SD card is the default configuration because it is easier to update firmware in the field by exchanging SD cards rather than removal of the Phycore SOM to reprogram the NAND. In order for the bootloader to load data from the SD card it needs to have a FAT file system stack. The FatFs library was used as it is designed for embedded use in microcontrollers and carries the 1-clause BSD license

which does not restrict commercial use. Once the application is transferred to RAM the program counter is set at the memory location of the main loop also referred to as the entry point.

Clock Timings and Optimizations

The AM335x processor series has five operational performance points (OPP) specified by TI. OPPs can be varied by changing the microprocessor unit's (MPU) phase lock loop along with the MPU voltage produced by the TPS65910 PMIC. Table 1 shows a summary of the performance and power consumption of the different OPPs. The 1GHz clock speed is only supported by the AM3358 and not the AM3359 processor used in the Phytec SOM. For the performance benchmarks, the power measurement was made when the entire PDNA system was running, and the FFT is un-optimized with 8192 points. Changing the OPP from 100 to Nitro increased performance by 66% while only increasing total system power by 10%. As a reference, the PDNA draws 5.4 W when on standby.

Table 1. OPP power and performance.

OPP	Clock Speed	MPU Voltage	Power (W)	FFT Speed (ms)
50	300	0.95	8.88	43.06
100	600	1.1	9.00	21.31
120	720	1.2	9.36	17.73
Turbo	800	1.26	9.60	15.96
Nitro	1000	1.325	9.96	12.73

The Cortex-A8 has a vector floating point unit which is IEEE compliant for single and double precision floating point. The NEON coprocessor is 10 stage pipeline using a 128 bit parallel architecture and also shares the same registers with the VFP unit thus simultaneous operation is not possible. The NEON core is limited to single precision

floating point operations, but can compute four operations simultaneously. The NEON core uses the Advanced SIMD instruction set and algorithms must be autovectorized for it by the compiler or targeted explicitly by using intrinsics or assembly code. TI's ARM compiler does not support intrinsics so NEON code must be written completely in assembly without any C code. Due to the limitation of the TI ARM compiler, the software was switched to GNU's Compiler Collection (GCC). Switching to GCC reduced the final binary size by 40% as well as increased FFT performance by 10%.

Digital Signal Processing

The digital signal processing is completely embedded in the firmware and is written in C. Most algorithms are performed for every measurement: automatic gain control, the Fourier transform, quadratic smoothing, and adaptive line fit. Other main functions, the internal correction and process calibration, are only executed as necessary.

Fourier Transform

The Discrete Fourier Transform (DFT) is used to determine the spectral content of time domain signal of the dispersed pulses. The DFT algorithm requires N^2 complex floating point multiplications and N^2 - N complex additions. Alternative Fast Fourier Transforms (FFT) can reduce the number of multiplications to $(N/2)\log_2 N$ with $N\log_2 N$ complex additions. which offers substantial increase in performance. The most common FFT is the Cooley Tukey algorithm which decomposes the time domain signal into N/2 DFTs. A further increase in performance can be obtained using the bit reversal technique.

When computing the FFT of a signal which contains all real values, the complex inputs are set to zero. It is possible to compute an N length FFT of a real-valued signal

using an N/2 length FFT. Using the NEON coprocessor, the FFT was able to compute four simultaneous floating point operations to allow for additional improvement.

Table 2. FFT benchmark speeds in miliseconds.

N	FFT	Real FFT	Real FFT NEON
256	0.36	0.19	0.08
512	0.71	0.38	0.12
1024	1.69	0.88	0.25
2048	3.42	1.77	0.51
4096	7.91	4.05	1.02
8192	15.9	8.19	2.16
16384	37.8	18.8	4.90

Regression

To determine the slope and offset of the cutoff region in a waveguide a linear regression on the frequency spectrum is needed. The curve fit is accomplished with the linear least squares approach which involves solving an overdetermined system of linear equations. The algebraic solution requires computing the psudoinverse of a matrix which can be computationally impractical with large matrixes. Alternatively orthogonal matrix decomposition methods can be used. Common methods are the LU, Cholesky, QR, and SV decompositions. LU and Cholesky decompositions only operate on matrices of full rank. LU is mathematically Gaussian elimination requiring $2m^3/3$ flops and Cholesky decomposition is twice as efficient using only $1m^3/3$ flops. However, since most systems will be overdetermined, Cholesky was not implemented.

QR factorization decomposes a Matrix into a product of an orthogonal matrix and an upper triangular matrix. QR factorization can be computed using the Gram-Schmidt algorithm, Householder transformations, or given rotations. Householder requires $2mn^2 - 2\,n^3/3$ operations. The Gram-Schmidt process requires $2mn^2$ operations.

While Householder requires more operations, the Gram-Schmidt algorithm can be parallelized. Also with m much greater than n, the operation count is approximately equivalent. Singular Value Decomposion can also be used to solve a system of linear equations, but requires $2mn^2 + 11n^3$operations. The reduced modified Gram-Schmidt algorithm was chosen for implementation [29].

Smoothing and Averaging

Two smoothing algorithms have been implemented: a moving average filter and a locally weighted quadratic regression proposed by Cleveland [30]. The algorithms are more commonly known as boxcar averaging and LOESS. The boxcar averaging is implemented as a transposed Direct Form II filter with constant input coefficients normalized to the filter length. This filter is computationally inexpensive, but the slope of the rise region will be distorted with larger filter lengths. The LOESS algorithm when applied to equally spaced data points can have a significant computational advantage when compared to its use in statistics [31]. For the second order polynomial fit, a QR decomposition on the Vandermonde matrix is performed on the data subset. The Tricubic distribution is used as the weighting function. Also the equal spacing necessitates computation of only half of the tricubic weights due to symmetry. The additional "robust" outlier removal step commonly included in the LOESS was not implemented to keep computational time to a minimum.

Fig. 45 shows a comparison of a raw spectrum with the two types of averaging both having a 5% span. Note the large distortion of the general shape by the moving average where the LOESS algorithm demonstrates good correlation with the original data.

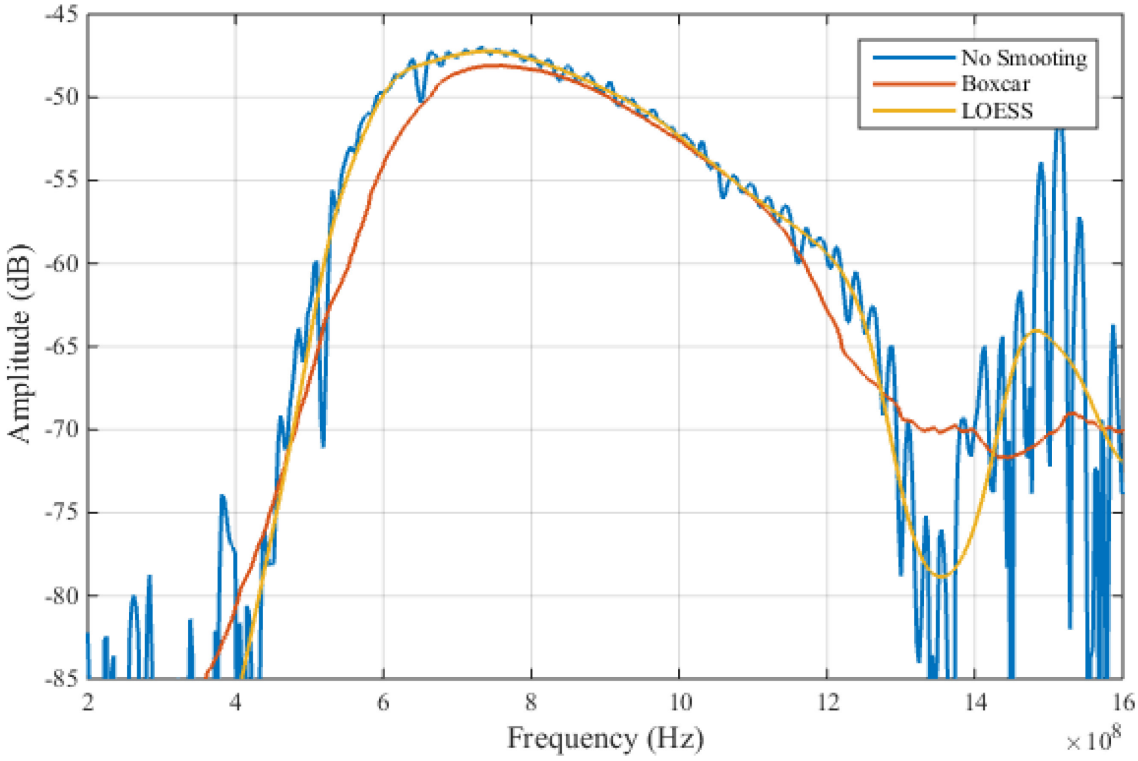

Fig. 45. Comparison of a waveguide spectral response with two types of smoothing.

Table 3. Benchmark of smoothing algorithms in miliseconds.

N	Boxcar			LOESS		
	1%	2%	4%	1%	2%	4%
256	0.10	0.21	0.32	0.08	0.31	0.67
512	0.41	0.54	1.21	0.44	0.88	2.55
1024	1.27	2.41	4.67	1.26	3.48	9.92
2048	4.84	9.41	18.9	5.48	13.7	40.9
4096	19.0	39.3	77.7	21.9	57.8	165
8192	79.1	158	313	91.5	232	665

Automatic Gain Control

The amplitude of the time domain waveform from the pulse transceiver can range from a few millivolts to over a volt. The ADC can capture signals ranging from zero to five volts. The DC offset voltage and gain needs to be adjusted in order to maximize the dynamic range of the ADC. This capability is present in the hardware, which can adjust a gain feedback potentiometer and a DAC driving the DC voltage over the I2C bus. An

iterative algorithm controls the automatic gain control. The algorithm will only adjust the signal if the voltage drops under two volts or is within 40 mV of the rails. When the voltage is too low the gain is increased to expand the peak to peak voltage to 4.5 volts. The new DC voltage is set by the ratio of the current DC voltage level to the signal minimum. The algorithm does not measure the current DC value, but uses the DAC's programmed value. If the signal is clipping the gain is halved and the algorithm is called again.

Internal Correction

Since an ideal spectrum of the pulse transmitted through the material under test is a sinc function, the spectrum's amplitude decreases within the frequency band of interest. This non-uniform excitation must be taken into account. Preprogrammed sinx/x correction cannot be used as the spectrum power level and shape varies strongly with the system temperature. There are also systematic spectrum inaccuracies from cross talk, switching noise, and impedance mismatches. These errors can also be removed with internal correction process. This process involves capturing the output spectrum through the calibration path without it passing through the material under test. Two isolation measurements are also taken to remove the systematic errors.

$$20 * \log_{10} \left| \frac{Ext - ExtIso}{Int - IntIso} \right| - 30 + ExtAtten - IntAtten \tag{17}$$

Adaptive Line Fit

Once the spectral response of the material under test has taken, features must be extracted from the response to perform a calibration. For waveguide cutoff analysis the rise region and fall region of the spectrum must be accurately identified over a wide

range of material properties. One method to characterize those regions is with a first or second order polynomial fit. However, the frequency ranges defining those regions must be adequately defined. Previous implementations of Guided Microwave Spectrometry used fixed frequencies which were selected by a calibration engineer. This procedure is highly effective when the material properties for that process have low variance as is the case for many control systems. When the material under test has large variances in permittivity and conductivity, a new method for the selection of those regions is needed.

An algorithm to adaptively extract the cutoff and passband regions of a waveguide was developed. The algorithm starts by performing a decreasing frequency peak search starting at the spectrum maximum in the frequency band of interest. In order for a peak to be identified, the difference in the spectrum's amplitude between local minimum and maximum must be at least 1dB. The lowest frequency peak within 12dB of the global maximum is identified as the cutoff frequency.

Communications and User Interface

Communication between the PDNA and a user is accomplished through either USB or Modbus. The HART protocol which is modulated on the 4-20 mA loop was designed and populated in hardware, but left for future firmware implementation. The USB connection has a graphical user interface for complete control and data display designed for Windows 7 x64 computers. Modbus, the second commination method can only modify system variables. Calibrated and raw spectrums for data display were deliberately not included in Modbus memory map due to its speed and packet limitations.

USB API

The primary method for control of the PDNA's calibration and settings is accomplished through USB. Rather than to use the USB communications device class (CDC) for a virtual serial port, the vendor specific class was used. While this method increased development time, a virtual serial port implementation has a much slower data transfer rate and requires careful settings of the COM ports. However, the vendor specific class requires custom firmware and drivers. To simplify development, WinUSB was chosen for the device driver instead of using the Windows Driver Frameworks. WinUSB is a generic USB driver written by Microsoft and provided with the Windows Driver Kit. While the various functions for control could have been built directly into the GUI a more flexible approach was taken. The functions were written in C++ as an application program interface (API) compiled to a windows dynamic-linked library (DLL). This API DLL can then be included in a MATLAB based GUI, a C# Windows Presentation Foundation GUI to be later developed, or even provided to clients for their own use.

Since WinUSB does not support isochronous transfers, a custom Bulk Device class firmware was used on the PDNA. This USB stack was provided with the StarterWare libraries and migrated from code for TI's Stellaris microcontrollers since they share the same USB hardware. USB bulk transfers have a guaranteed packet delivery with CRC-16 error detection, but no guarantee of bandwidth or latency. The modifications to the USB library previously mentioned provide good performance summarized by Table 4. The N column is number of single precision floating point number transferred.

Table 4. USB performance

N	Single Frame
256	340 us
512	421 us
1024	550 us
2048	809 us
4096	1.35 ms
8192	2.34 ms
16384	4.41 ms

Windows GUI

The graphical user interface was written in MATLAB to decrease development time. MATLAB allows deployment of the GUI as an x64 Windows executable with MATLAB Compiler Runtime (MCR). Use of the MCR does not require a license and does not have any commercial restrictions. Two individual GUIs were created, one for the manual adjustment of variables and one for implementing a calibration. Neither GUI performs any calculations or functions necessary for the day to day operations of the PDNA.

The engineering GUI shown in Fig. 46 displays the dispersed time domain pulse as well as the internally corrected spectrum. The raw time and frequency domain data including the isolation measurements can be displayed as well. A user can also modify system variables to adjust the extended time factor, dispersion capture length, output power, averaging, etc.

The second calibration GUI in Fig. 47 assists in the collection of data to perform a calibration for a new process. Sample spectrums, called replicates, can be saved and selectively displayed along with their respective dual line fit variables. These replicates are not stored on the PC running the GUI, but resided on the PDNA itself.

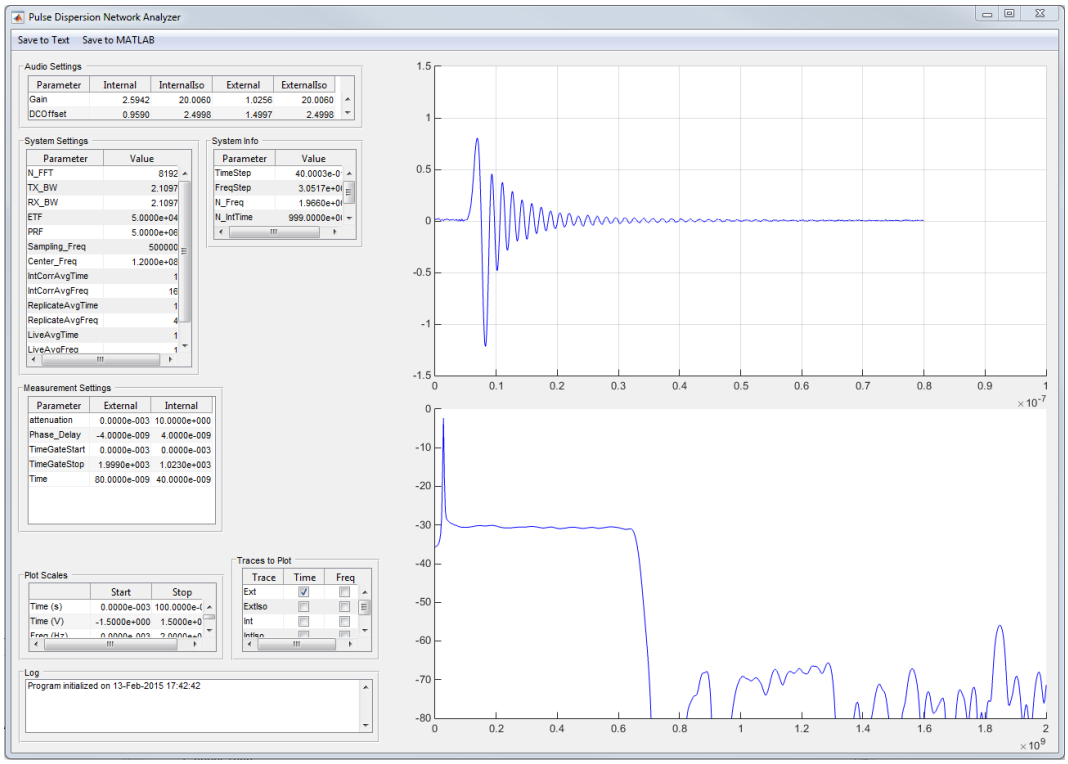

Fig. 46. The engineering GUI.

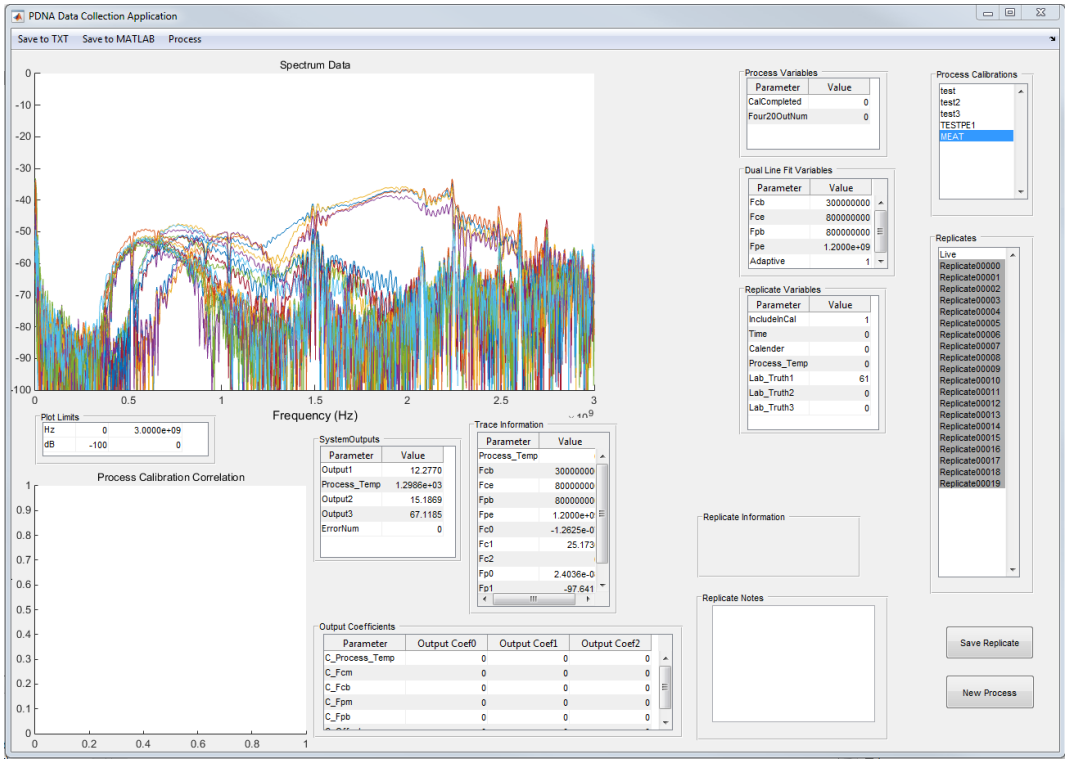

Fig. 47. The calibration GUI.

Industrial Communications

The FreeMODBUS stack from Embedded Solutions in Vienna, Austria was ported to the ARM for the Modbus communications. This software can be used commercially with as it is released under the BSD license. It supports all three frame formats of the Modbus specification: RTU, ADCII, and TCP. However, the RTU format is the most common in the targeted industries so it is the only one which is currently implemented in the firmware. The baud rate is set to 115200 with 8 data bits, 1 stop bit, and even parity. The only Modbus commands implemented are the read and write to holding register. Modbus coils are not used, as single bit registers are not practical for any system variables. Each variable structure is mapped to a holding register and can be changed. If variables are changed to invalid numbers the system will not update that particular variable, thus it is necessary to read the holding registers after a write to verify the change.

The 4-20mA current loop is circuit is controlled via the SPI interface multiplexed with the direct digital synthesis IC for clock generation. Since only one 4-20mA output is available, the output variable must be set along with its ranges and alarm condition. The loop voltage can also be reported. For calibration of the 4-20mA loop two measurements for correction must be made. The transfer function for the output current is given by (18), where D is the 16 bit current output register, and $Gain$ and $Offset$ the two variables available for correction.

$$I_{loop} = \frac{\frac{16mA}{2^{16}} * Gain}{2^{16}} * D + 4mA + \frac{16mA}{2^{16}} * (Offset - 2^{15}) \tag{18}$$

CHAPTER FOUR

Applications to Industrial Measurements

This chapter presents the theory and analysis of four industrial processes for which microwave spectroscopy could be applied. The excitation structures, data collection and calibrations represent preliminary work and do not constitute commercial ready products. The reader should take them as proof of concept demonstrations to motivate the development of applications for microwave metrology using the Pulse Dispersion Network Analyzer.

Steam Quality

Nuclear and sub-critical coal power plants monitor steam quality to insure extended longevity of turbine blades. Without an in-line measurement system for steam quality, the quality cannot be regulated by the power plant control systems for optimum efficiency. Also in highly viscous oil fields, steam is injected downhole to increase the extraction rate of the oil. The cost benefit analysis for the steam injection would have a much smaller degree of uncertainty if the enthalpy of the steam were known. Steam generating boilers could then be tuned in real time based on the output of individual wells.

Theory & Experimental Setup

As stated in Chapter One, the effective permittivity of a mixture depends upon a volumetric ratio instead of a mass ratio. Using the Birchak permittivity mixing equation (4), the effective permittivity of steam as a function of its quality is given in (19). Large

changes in steam quality result in very small changes in volume and thus permittivity. For example, 90% steam quality corresponds to 0.011% liquid water by volume which results in an increase of the effective permittivity by less than 0.01 as comparted to 100% quality. The small changes of the relative permittivity over steam quality are shown in Fig. 48. A highly resonant meta-material sensor approach was used because of this requirement of large sensitivity based on a previously acquired patent [32].

$$\varepsilon_{eff}(SQ) = \left[\frac{SQ \cdot (\frac{\rho_w}{\rho_s})}{1 + \left(\frac{\rho_w}{\rho_s} - 1\right) \cdot SQ} \cdot \sqrt{\varepsilon_s} + \frac{1 - SQ}{1 + \left(\frac{\rho_w}{\rho_s} - 1\right) \cdot SQ} \cdot \sqrt{\varepsilon_w} \right]^{1/2} \tag{19}$$

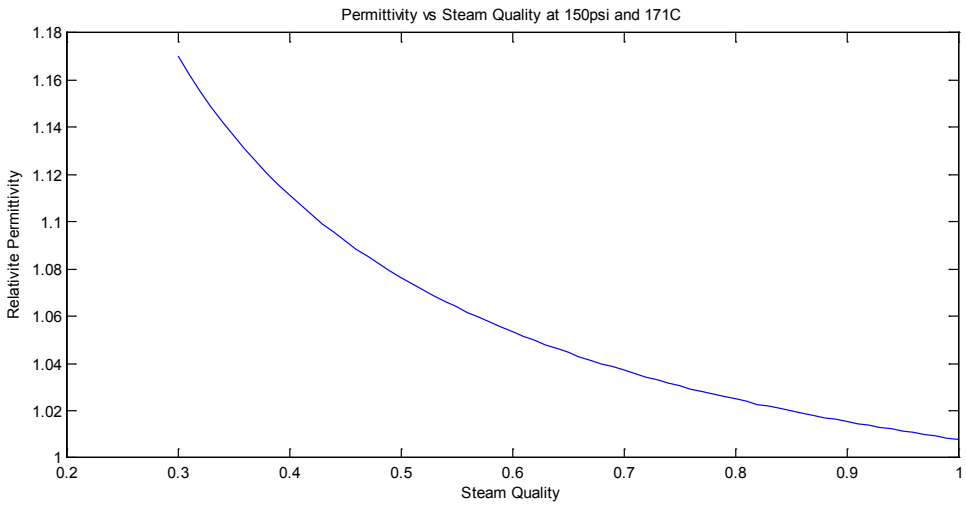

Fig. 48. Steam quality versus effective permittivity.

In many flow loops including steam, orifice plates are commonly used to determine the mass flow rate. With an orifice plate, the diameter of the pipe is restricted and the pressure on both sides of the pipe is measured. Flow rates can then be calculated based as described in the international standard ISO 5167. A steam quality sensor would have greatly reduced plant installation costs if it could be inserted into a circular pipe as a

replacement for an orifice plate. Orifice plates do not need to be limited to one central opening and could be altered for the design of a microwave sensor.

The orifice plate was restructured to have multiple openings in order to exhibit the properties of a split ring resonator. The new plate was specifically tuned to exhibit three distinct resonances with frequencies based on the material filling each ring. The largest of the rings dictates the lowest frequency null. For the excitation structure, a parallel plate waveguide is used so that the electric field is parallel to the resonator. A parallel rather than perpendicular electric field will increase the Q factor of the resonator as more energy is coupled into the rings. The microwave feed for the waveguide is a monopole encased in ceramic. A cross sectional view of the CAD model for the sensor is shown in Fig. 49. In practice, SMA cables are attached to the monopoles, shown in yellow, but are omitted from the CAD model. The complete design and analysis of this structure is published by Faulkner [33].

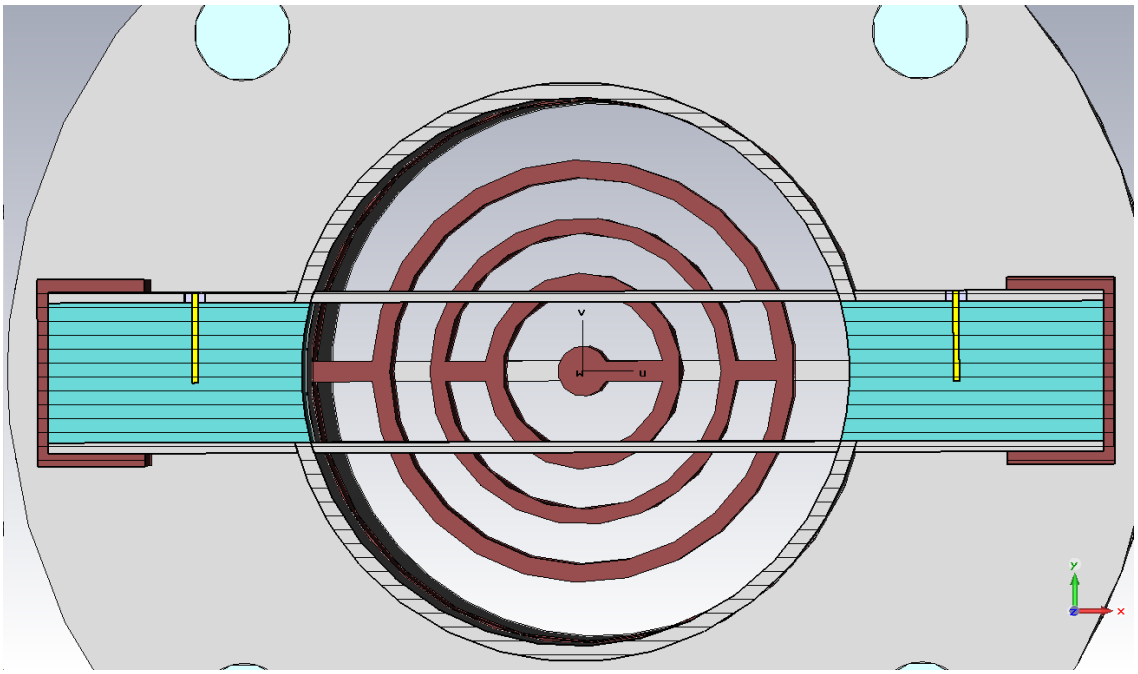

Fig. 49. Cross section of steam quality sensor.

The steam quality sensor was also simulated using the full 3D electromagnetic solver, CST Design Studio. The simulations were conducted in the time domain using using pulses while including material losses from the imaginary component of permittivity. The relative permittivity of the material filling the pipe was swept from 1.01 to 1.17 which equates to steam qualities of 100% to 30%. Fig. 50 contains the S_{21} magnitude in decibels of the simulation. Three distinct nulls near 1.1, 1.5, and 1.9 GHz can be seen with over 20dB of depth. The lowest frequency null is a result of the largest outer ring while the highest null is form the smallest center ring.

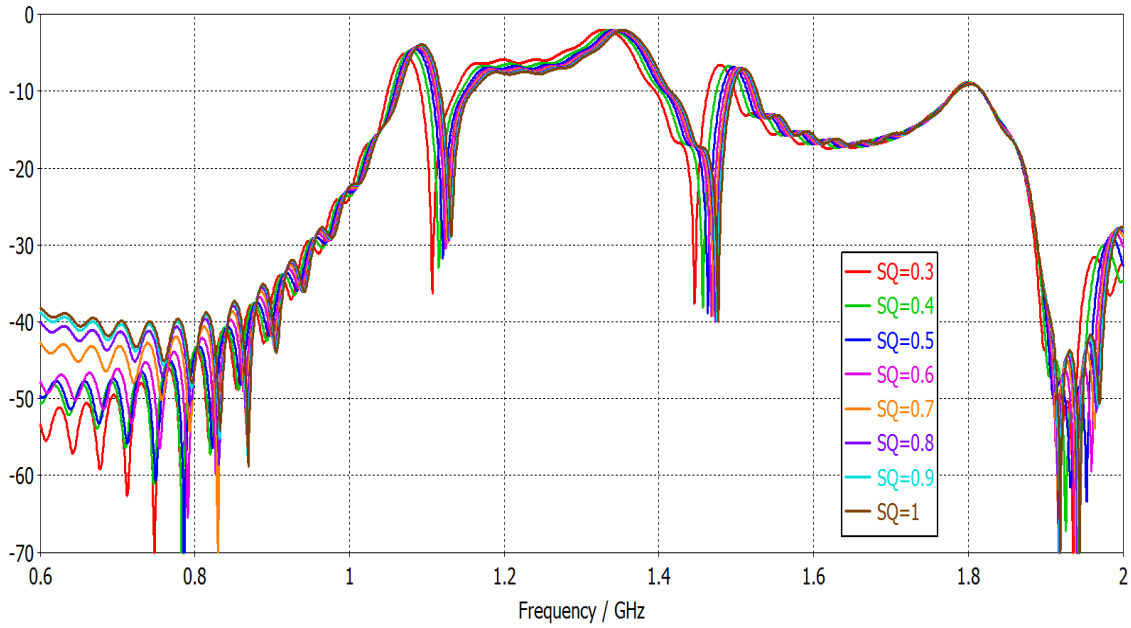

Fig. 50. Simulation of S_{21} response of steam quality sensor.

The frequency of the nulls are identified and tracked with a peak detection algorithm and the first two are plotted in Fig. 51. Both nulls exhibit shifts of approximately 25 MHz due to the 0.16 increase in relative permittivity of the material filling the pipe.

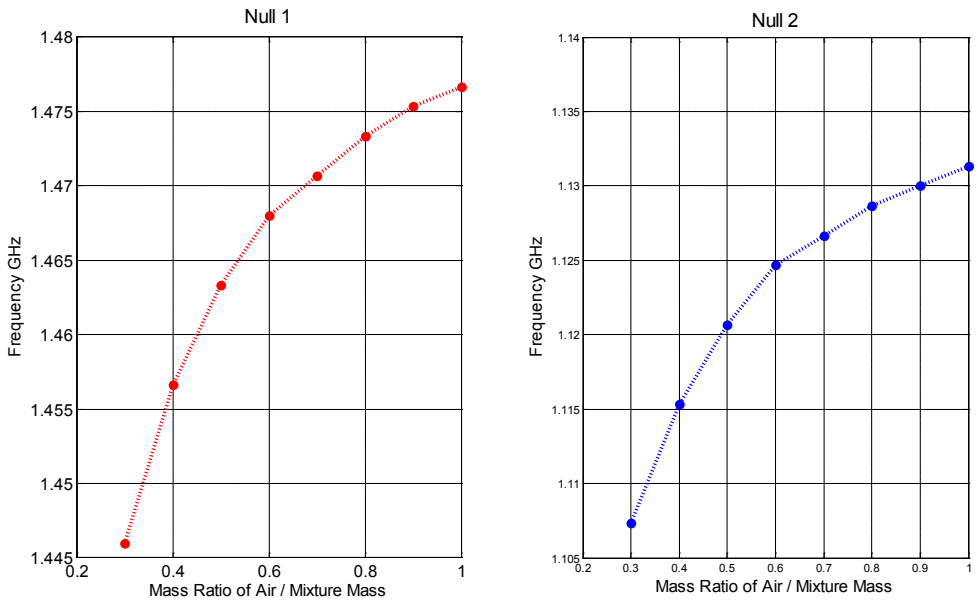

Fig. 51. Tracking the first two nulls of steam quality simulation.

Since the construction of a steam loop requires a large capital investment, sensor prototypes were evaluated on a two phase system consisting of water and air shown in Fig. 52. This procedure is commonly used to verify and test orifice plates for steam. The pipe and parallel plate waveguide were fabricated in-house out of steel. The split ring resonator was outsourced to be cut with a laser for increased precision in the ring's dimensions. The resonance properties of metamaterial structures are highly sensitive to manufacturing tolerances and rings machined with drill bits were not precise enough. Instead of a ceramic material filling the microwave feed assembly, HiK Cement from Laird was used. The cement has a similar permittivity to ceramics, but does not have the need for expensive tooling for prototypes. Production grade models will need the ceramic to survive in the high temperature and pressure environments. Fig. 53 is a picture of the finished prototype in the experimental test setup.

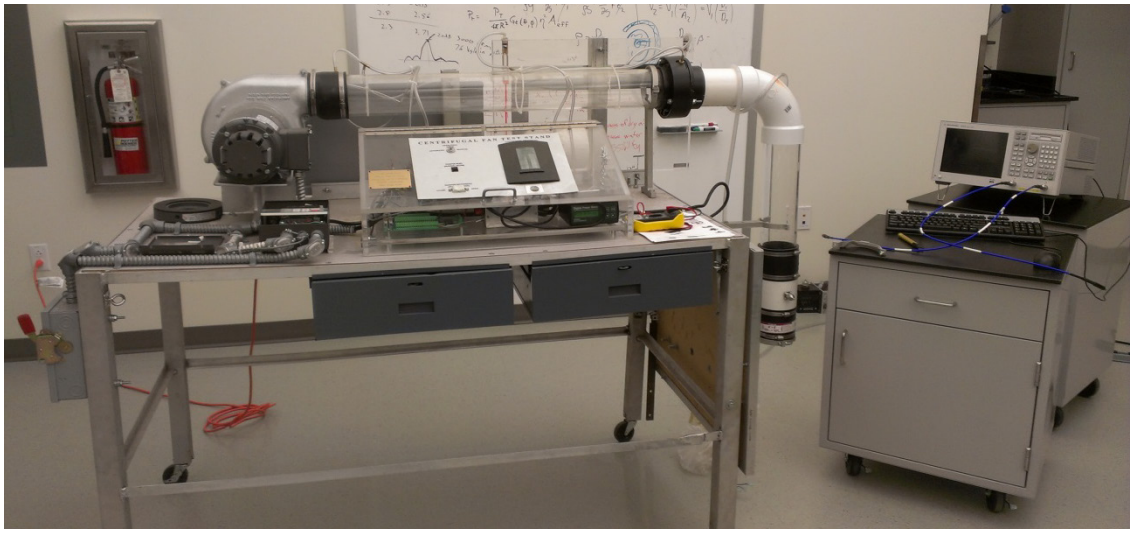

Fig. 52. Two phase test setup.

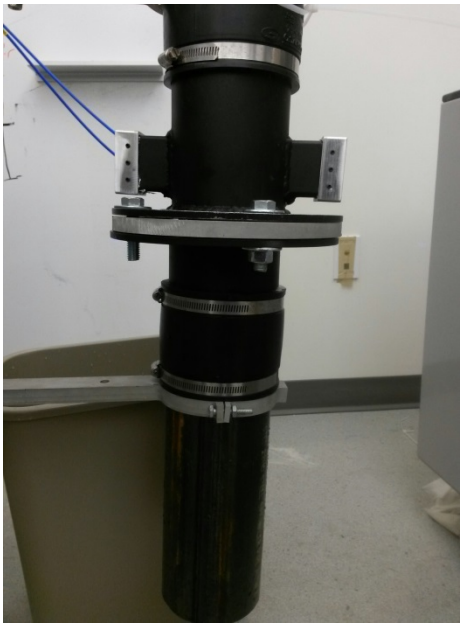

Fig. 53. Fabricated steam sensor prototype in the test system.

The air and liquid mixture exhibits a different effective permittivity than liquid and vapor. Using the measurable mass ratios from the test setup the effective permittivity as a function of volume will actual be lower than that in an actual steam loop. Fig. 54 compares the two permittivities versus their mass ratio.

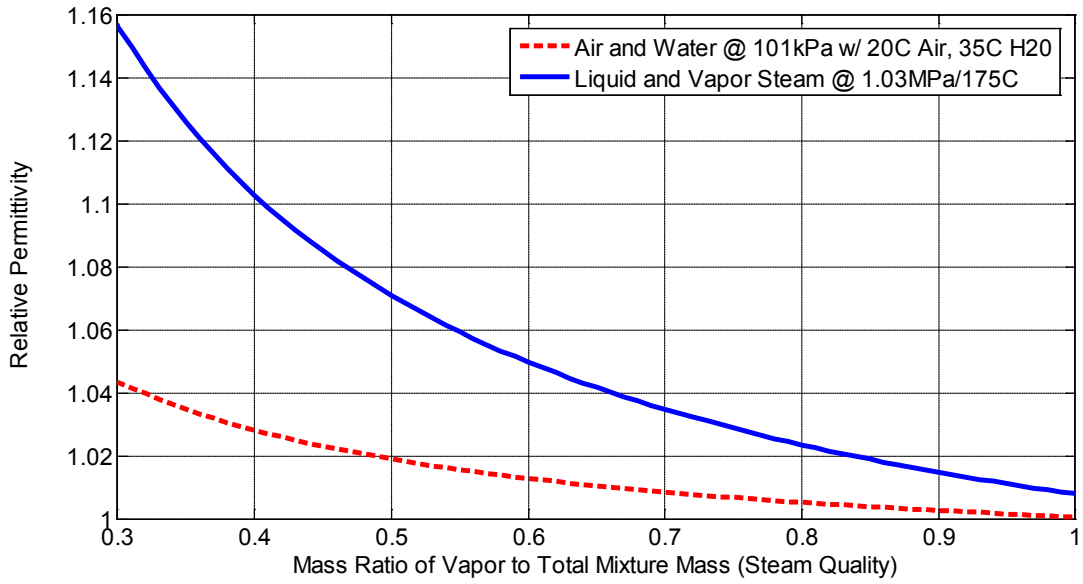

Fig. 54. Effective permittivity of air –water mixture and actual steam.

Measurement Results and Analysis

To conduct the experiment, the air mass flow rate was fixed at 0.15 kg/s while the water flow rate was varied from 0.1 to 1.5 GPM. This range equates to relative permittivity variations of 1.0018 to 1.0128. The equivalent steam quality at those permittivities is 100% to 93%. The resulting spectrum magnitudes from the experiment are shown in Fig. 55. The measurement exhibits good correlation with the simulation up to 1.75 GHz. A null tracking algorithm was used to identify the frequency of each null which are plotted in Fig. 56. While the frequency of the first null has good response to the water flow rate, the second and third nulls are more erratic. The measurement data contained a large about of time domain fluctuations due to the water injection in the test setup. Smoother data could be obtained by increasing system averaging in the frequency domain.

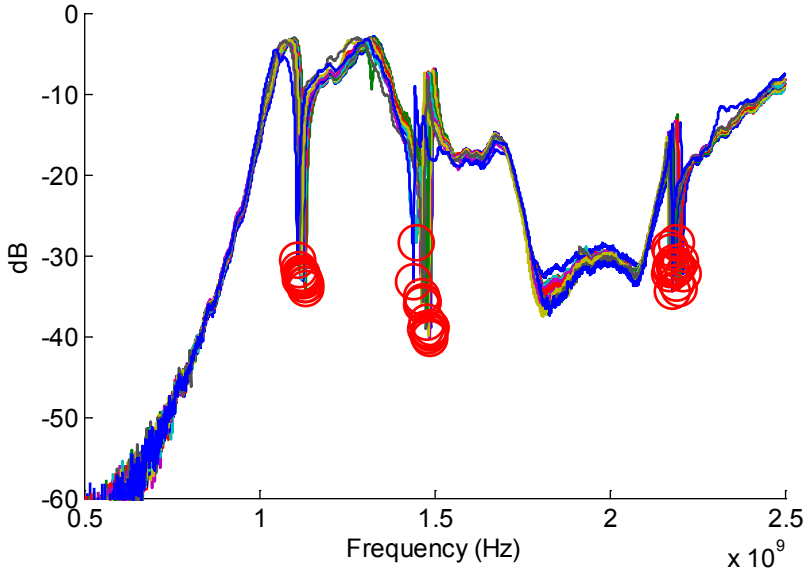

Fig. 55. Measured frequency response of steam sensor with varying water flow rates.

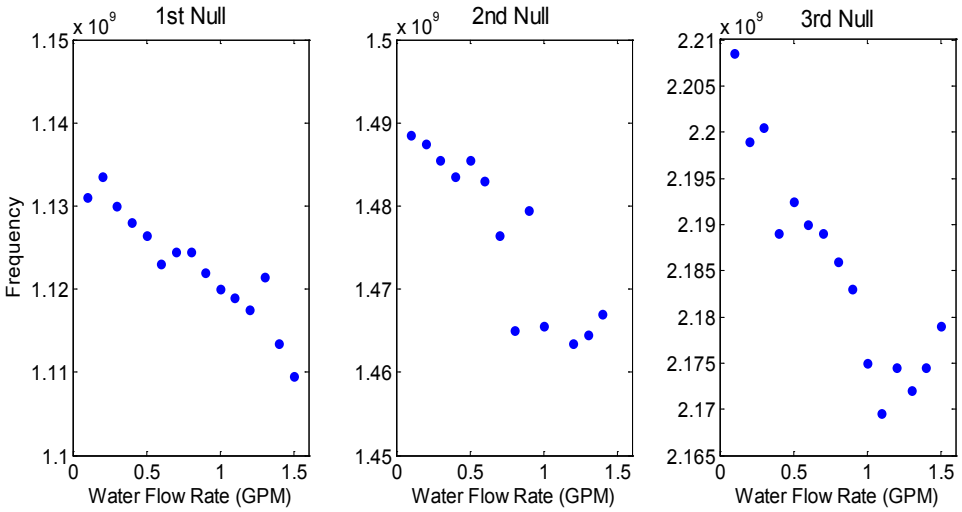

Fig. 56. Tracked null frequencies from two phase experiment.

Further Work

A high temperature and pressure sensor needs to be constructed before tests can be done in an actual steam loop. The split ring resonator needs to be evaluated for its sensitivity to vibrations along with mechanical survivability in high flow rate environments.

Fresh Concrete

As previously stated, the water to cementitious ratio in fresh concrete is linearly correlated with the compressive strength of the concrete. The current standard measurement procedure for the ratio is ASTM C143 otherwise known as the slump test. This test has a specified standard deviation of 6% to 19% depending on the range of the slump. For a microwave measurement system a major challenge is the non-homogeneity of the material. For initial laboratory testing, the concrete is mixed with a 1 to 2 to 3 ratio of cement to fine and then coarse aggregate. Portland cement is used along with sand for the fine aggregate and half inch diameter river rocks for the coarse aggregate. Instead of an in-line system design, the concrete sensor is targeted for a portable open air use. This will allow for the system to be used on site to measure small samples of concrete as it is being poured from the mixing truck.

Theory and Experimental Setup

The coarse aggregate in fresh concrete increases the difficulty of establishing a repeatable and accurate sensor due to the large geometric variances in the rocks. Larger rocks will lead to the propagation of higher order modes, which impedes the passband measurement of conductivity. Additionally the density of the aggregate typically varies from 1200 to 1750 kg/m^3 [34]. The Maxwell Garnett equation can be used to model the effective permittivity in the mixture.

Two different waveguide structures were investigated for their performance. The first is a standard guided microwave spectrometry chamber shown in Fig. 57. This waveguide is 155 mm tall, 46.6mm wide, and 101.2 mm deep. Coupling loops are used

for excitation on both sides of the waveguide. These loops are terminated with 50Ω loads. The bottom of the waveguide is closed, but the top was left open.

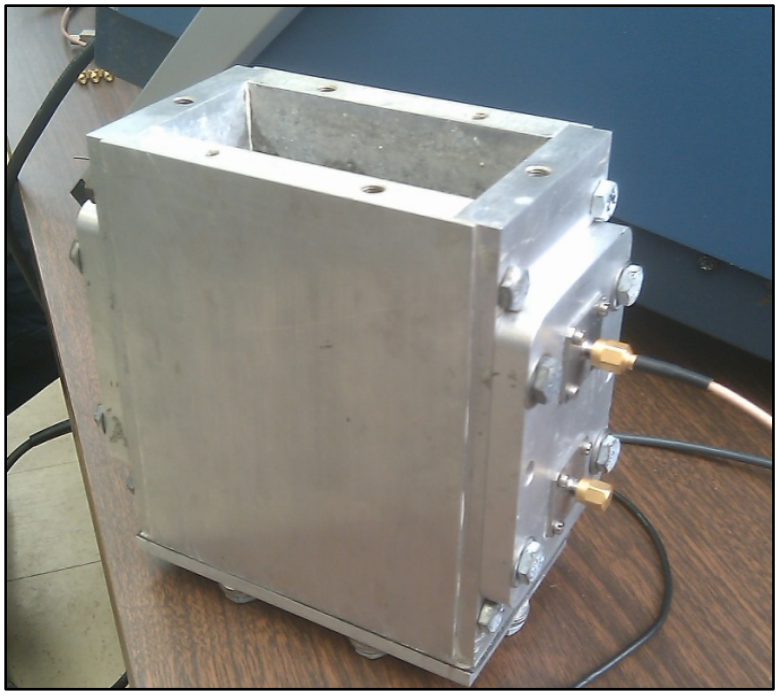

Fig. 57. Standard size GMS waveguide.

A second waveguide was designed to reduce the end effects of waves propagating out of the open chamber. This waveguide added metal grates to the top and bottom of the chamber. This grating raises the propagation frequencies of for any external radiating waves to beyond the frequencies of interest. The volume of the waveguide was expanded to be similar to that used in a slump test. The bottom of the chamber is held on with friction and is easily removable to facilitate the removal of concrete and cleaning of the sensor. The chamber is accompanied by an array of packing rods for a more uniform density between measurements as well as to remove the concrete. The waveguide and packing rods are shown in Fig. 58.

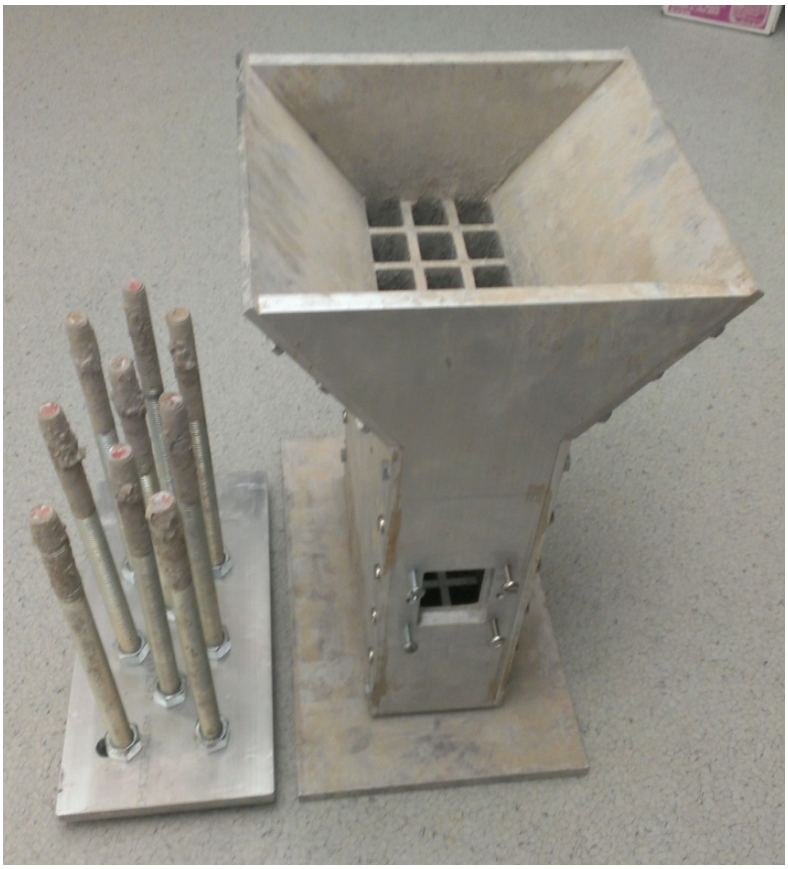

Fig. 58. Guided Microwave Spectrometry waveguide with grates and larger volume.

Measurement Results and Analysis

Before mixing concrete, measurements were first conducted using a sand and water mixture to determine sensitivity to small percentages of water. Fig. 59 shows the magnitude spectrum differentiation if the cutoff frequency as the water in the sand is varied between 4% and 10%. The shift is approximately 500 MHz with smooth transitions in the cutoff region. The high frequencies are attenuated by 10 dB due to the increased conductivity from higher water content. The high frequencies are more susceptible to the non-homogeneity of the mixture as higher order modes begin to propagate.

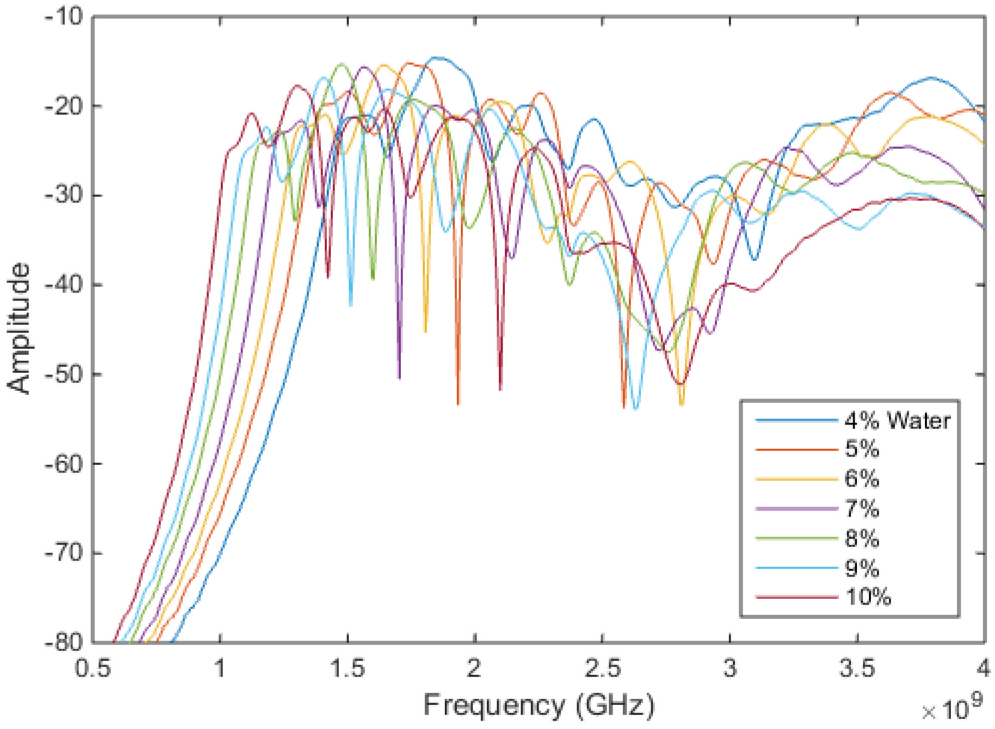

Fig. 59. Spectrum of sand and water mixtures in the standard GMS waveguide.

To further increase the material complexity, Class II and Class IV mortar were mixed and measured. Mortar has the addition of cement, but does not contain the larger coarse aggregate. Class II mortar has a one to three ratio of cement to sand, while class IV has a one to six ratio. The frequency response of the Class IV mortar is shown in Fig. 60 versus W/C ratios between 35% and 65% in 5% increments. The Class II data is omitted, but exhibits a similar response. The cutoff frequencies have a smooth transition between the seven W/C ratios and a total frequency shift of approximately 250 MHz. The high frequency attenuation from the water's increased conductivity is close to 20 dB. Each frequency trace was only measured once with zero averaging or remixing of the mortar.

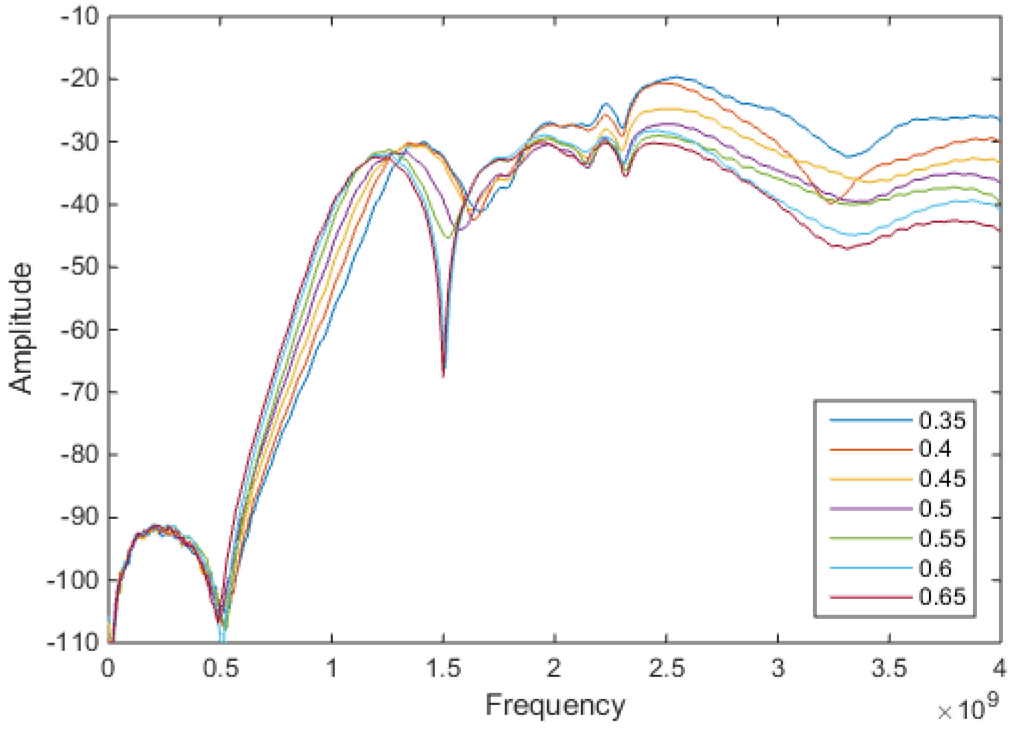

Fig. 60. Spectrums of Class IV mortar with varying W/C ratios.

Full concrete was mixed with and tested in the standard sized GMS waveguide. The water-to-cement ratio was varied again from 35% to 65% in 5% increments. The frequency spectrum responses of the measurements are shown in Fig. 61. The addition of the coarse aggregate causes large variations both in the cutoff region and the passband. Some passband irregularities are expected due to the increased propagation of higher order modes, increasing the inaccuracy of the conductivity measurement. The cutoff frequency variance is problematic and is caused by the proximity of the large aggregate to the coupling loops. Electromagnetic fields propagating outside the top of the waveguide also led to inconsistent measurements. To improve the data, multiple measurements at each W/C ratio need to be taken with remixing of the concrete.

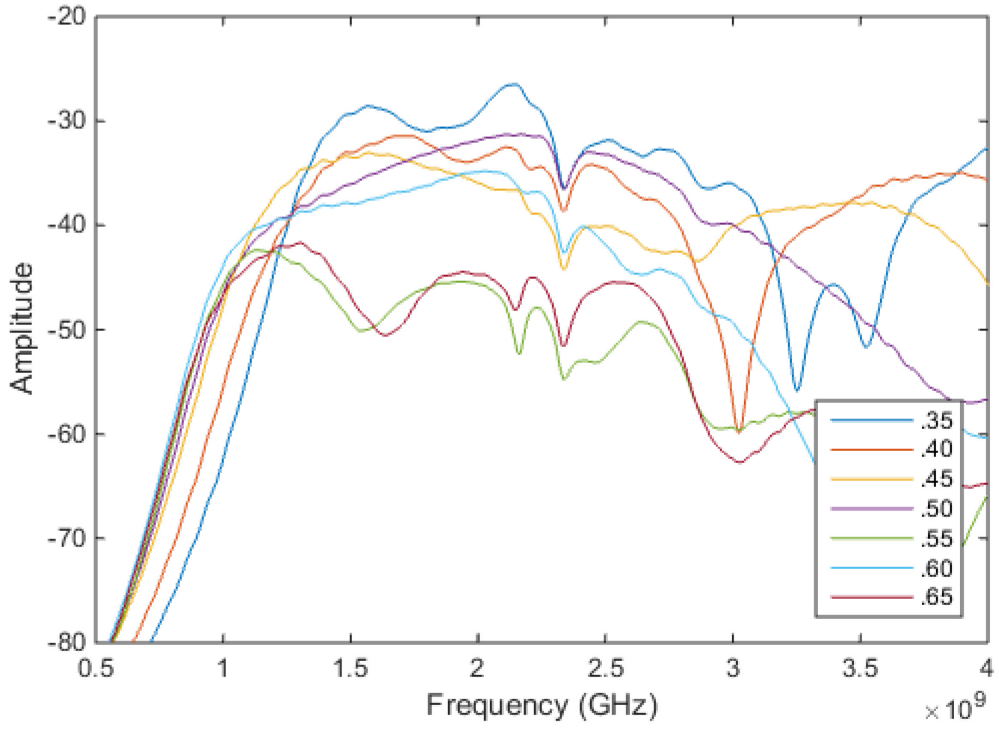

Fig. 61. Frequency response of concrete mixture with varying W/C ratios.

To obtain better cutoff frequency performance, the water-to-cement ratio was swept again from 35% to 65% in 5% increments, but measured using the larger GMS. Larger batches of concrete were used with each mixture containing 2.4 kg of cement, 4.8kg of coarse aggregate, and the water was varied from 0.7 kg to 1.4 kg. Every mixture was measured five times with complete removal and remixing of the concrete between each sample. Fig. 62 shows the $|S_{21}|$ for all the data. Repeatability between each measurement sample is quite good in the cutoff region and acceptable in the lower frequency passband region. Higher order modes from the large aggregate non-homogeneity begin to make a large difference past 2.5 GHz. The larger GMS waveguide reduces the amplitude by over 10 dB, but with a great increase in repeatability.

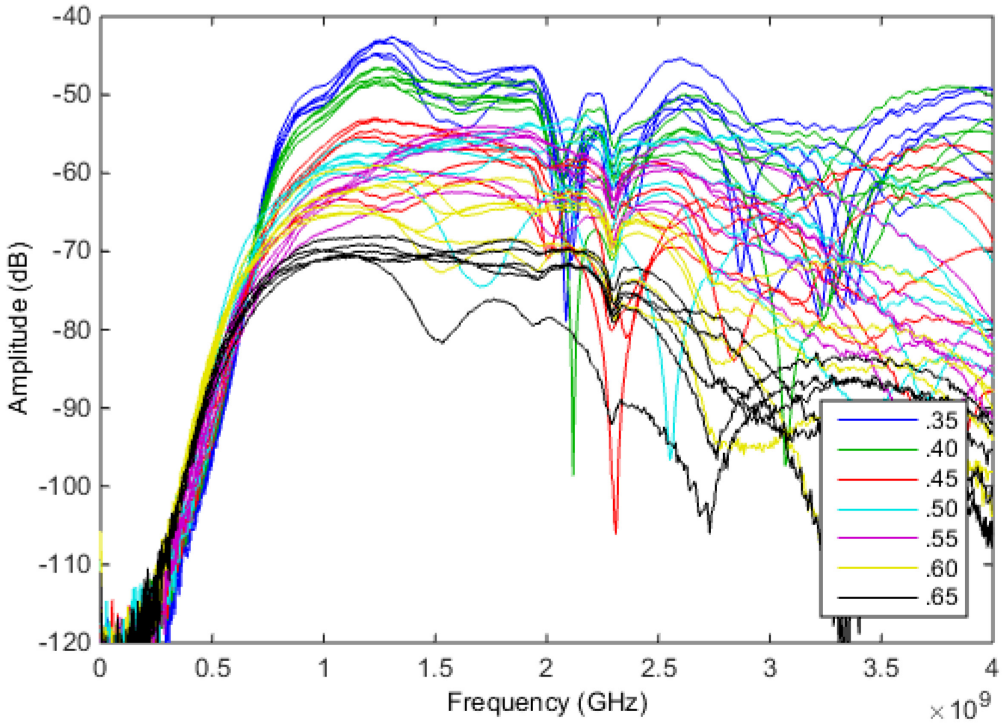

Fig. 62. W/C sweeps of fresh concrete in the larger grated waveguide.

The thirty-five data samples from the larger GMS were used as calibration data. For feature extraction, principal component analysis was used on the entire spectrums. The first five components contained 99.2% of the variation and were then used as inputs to a neural network along with the amplitude average of each spectrum. The neural network had six inputs, two hidden layers of five and three nodes, and a single output node. Each node used the common logistic function as its activation function. The network was presented three of each measurement for training, one for validation, and one for verification. The Levenberg-Marquardt backpropagation algorithm was used for training. Fig. 63 shows the output of the neural network calibration. The neural network calibration exhibits good correlation with r-squared values above 0.98.

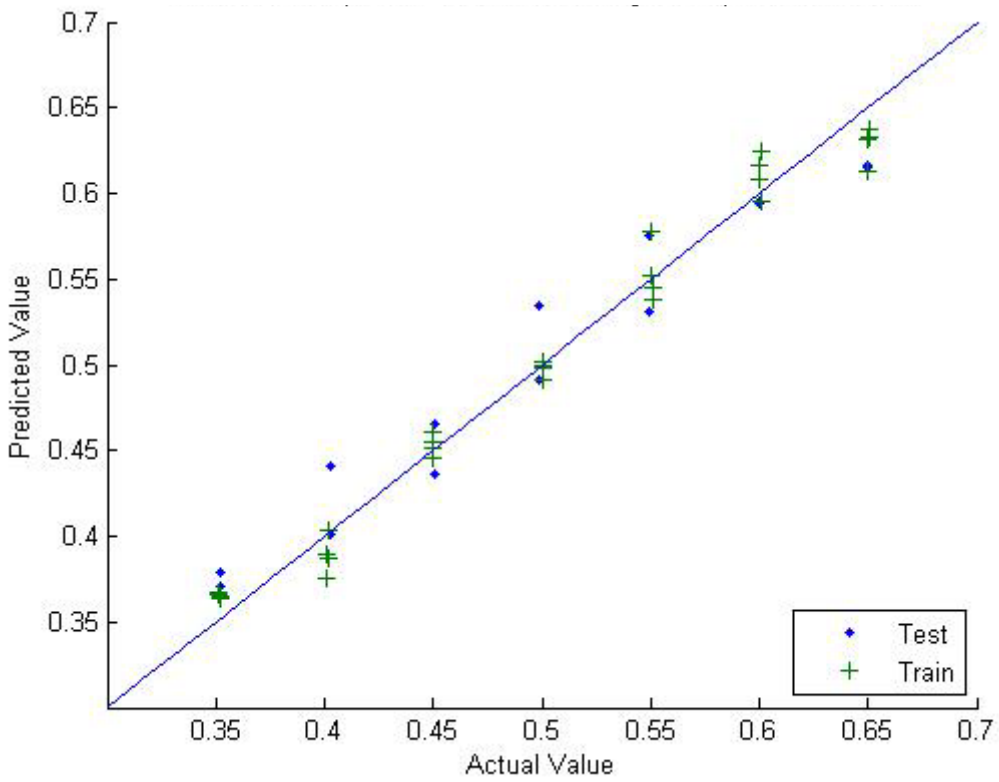

Fig. 63. Neural network predicted versus actual values of W/C ratio for fresh concrete.

The coarse aggregate poses increased difficulty in obtaining a repeatable measurement. A test was done where the placement of the coarse aggregate inside of the larger GMS was purposely distributed in a non-homogenous fashion. The first measurement was conducted in the same manner as all the previous ones, the second measurement left the aggregate at the top, the third packed the concrete down to increase density, and the forth was stirred inside the waveguide to distribute as evenly as possible. The results of these perturbations are shown in Fig. 64 with considerable impact in the higher passband frequencies. The cutoff frequency displayed small change reduced that was reduced by the longer wavelength relative to the aggregate's size at the lower frequencies.

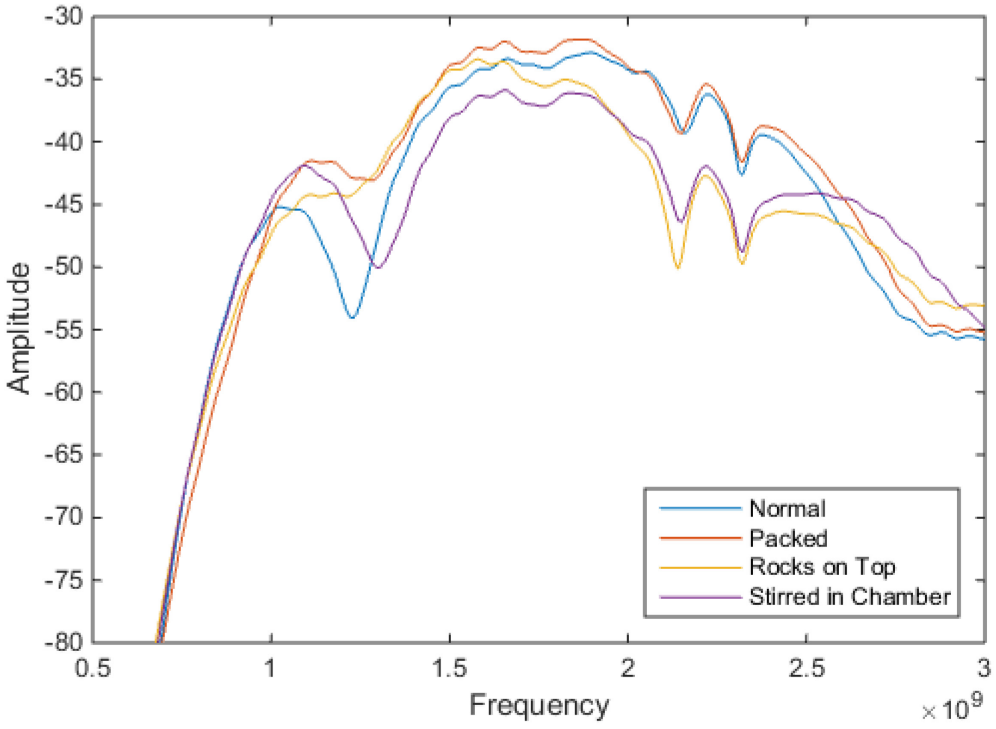

Fig. 64. Concrete perturbations in GMS waveguide.

Further Work

High performance concrete involves the use of various additives such as accelerators, retarders, and reducers, which could significantly alter its electromagnetic properties. While the volume of the additives is relatively insignificant, their inclusion needs to be investigated. In cold weather environments concrete is purposely mixed with entrained air to increase its durability during freeze-thaw cycles. This entrained air could noticeably reduce the effective permittivity.

Ground Meat

In a meat processing plant, raw meat received from a slaughterhouse is ground into small diameter pieces by use of large grinders. Grind plates with hole sizes from ½" to 1/8" are used on the exit of the grinder. The hole sizes are chosen depending on the

final product the meat is being prepared for and are a large factor in the density. The batch sizes are in the thousands of kilograms with the original fat content approximated by the slaughterhouse. Recipes for pepperoni, sausage, hamburger, etc. are specified by the customer along with desired fat content.

Theory and Experimental Setup

Lean beef and lean pork exhibit relative real permittivities between 55 and 62, whereas beef and pork fat have relative permittivities between 3 and 6 [35]. The imaginary components of the relative permittivity are approximately 19 to 25 in the lean meat and 0-1 in fat. Four types of pork were investigated with percentages of fat ranging from 14% to 80% as well as two types of beef with fat contents ranging from 5% to 55%. Four samples were taken for each of the six types of meat from batches of approximately 2000 kg. This experiment was conducted at a commercial meat processing facility. The meat inside of the chamber was then removed and sent to a commercial laboratory to measure percent fat, moisture, and protein.

Fig. 65. Expanded guided microwave spectrometer for ground meat.

Measurement Results and Analysis

Fig. 66 shows some spectral magnitudes for the variety of meat measured. The cutoff frequency exhibits shifts over a 400 MHz between the 5% fat beef and the 80% fat pork. Another feature of interest is the second order mode of propagation at 2 GHz present in only the pork trace samples. Each data point was captured while the meat grinder was paused.

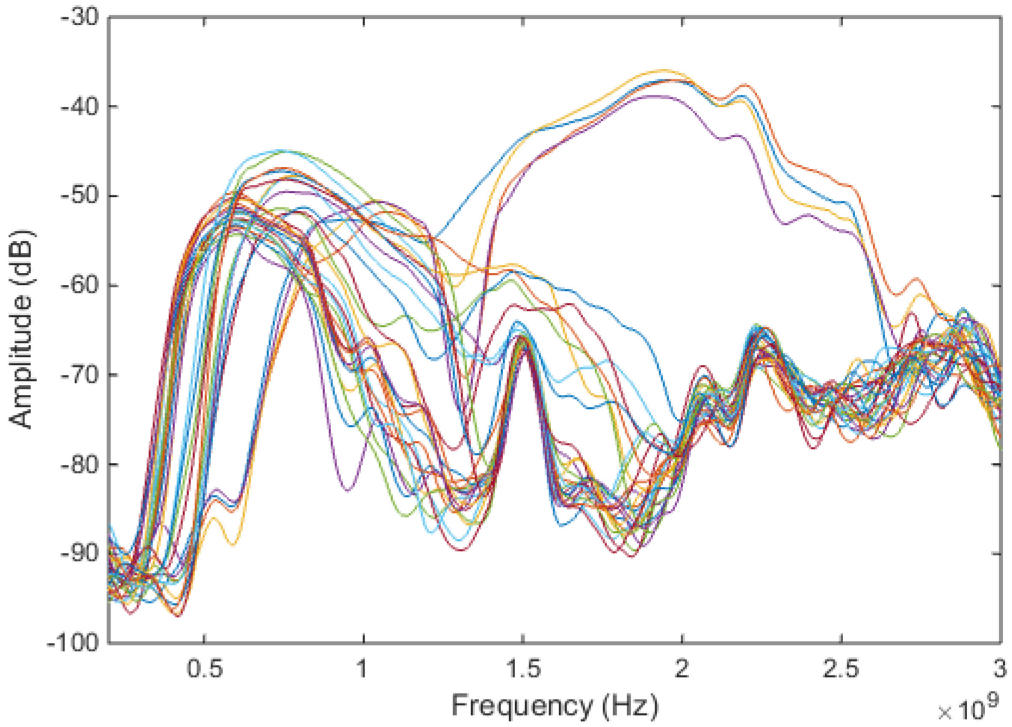

Fig. 66. Frequency response of differing types of ground pork and ground beef.

Fig. 67 shows one magnitude spectrum of 18% fat pork with two additional lines characterizing the cutoff and passband regions. These lines were calculated with the adaptive line fit algorithm explained in Chapter 3. A second order fit could be done on the rise region to increase the characterization accuracy. However, increasing the number

of features extracted from the signal requires additional data due to the curse of dimensionality.

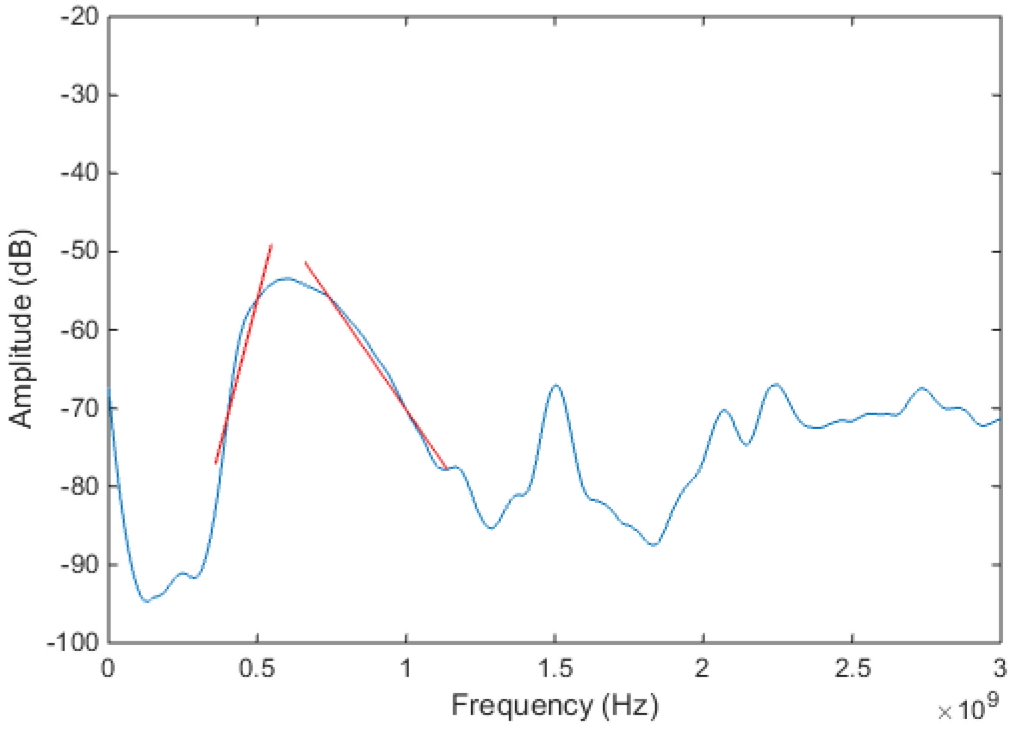

Fig. 67. Spectrum of 18% fat pork.

A multilinear regression was performed on the slope and offset of the frequency data as given by the adaptive dual line fit algorithm. Each regression used a total of twenty-eight replicates comprised of four types of pork and two types of beef. Since the span of the relative permittivies is quite large, the shifts in cutoff frequency will have considerable error if approximated by a linear function. To compensate for the non-linearity, a third order polynomial fit was applied to the output of each linear regression. The output of this calibration is shown in Fig. 68 for percent fat, Fig. 69 for percent moisture, and Fig. 70 for percent protein. The r-squared values for each calibration are 0.97.

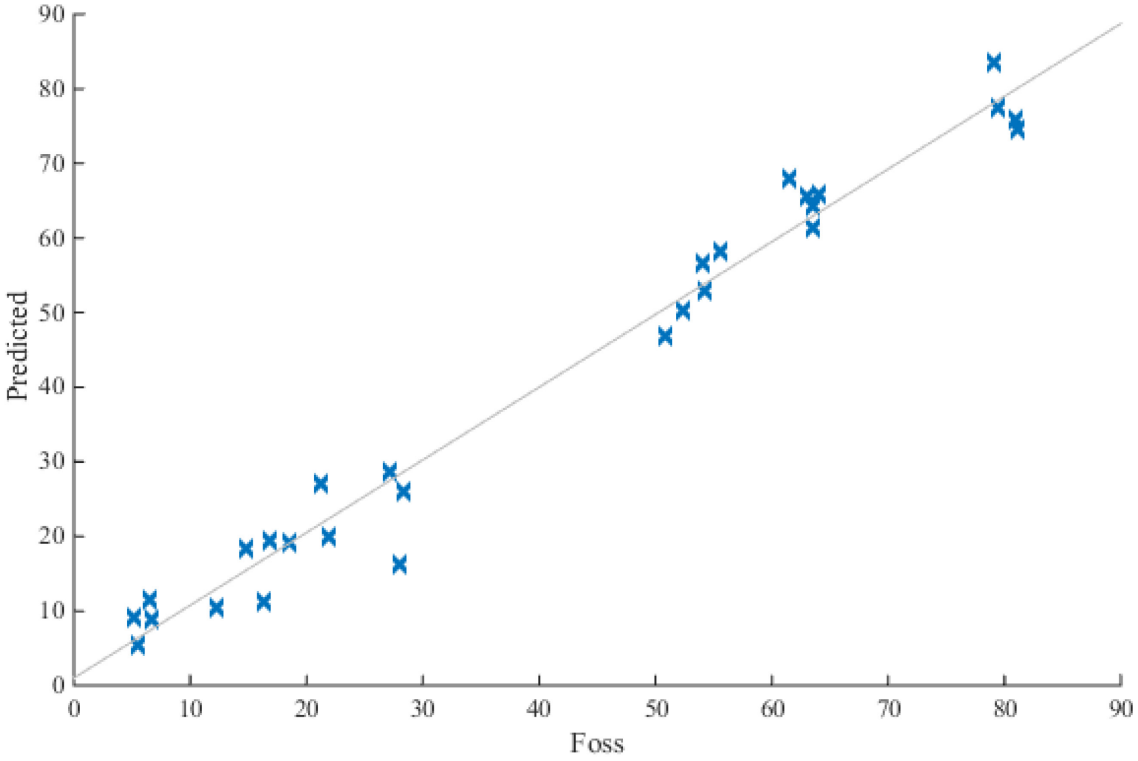

Fig. 68. Predicted versus actual percent fat in ground beef and ground pork.

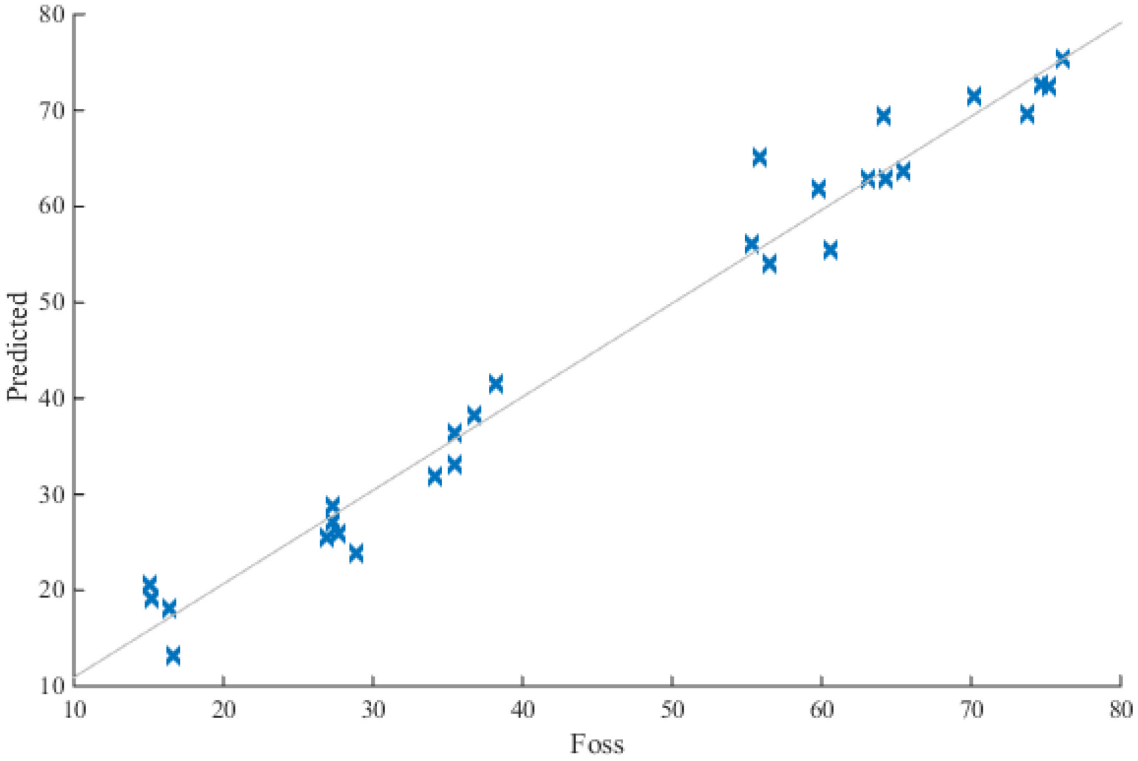

Fig. 69. Predicted versus actual percent moisture in ground beef and ground pork.

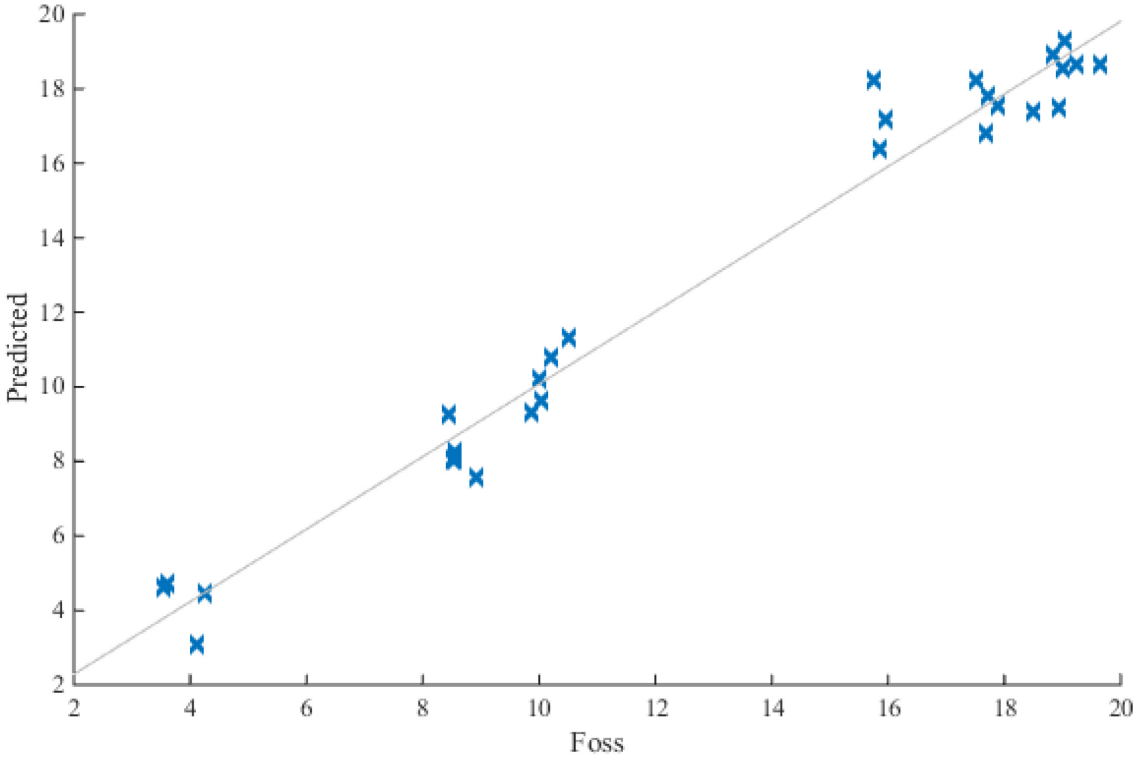

Fig. 70. Predicted versus actual percent protein in ground beef and ground pork.

A neural network was then trained on the data as an alternative to the linear regression. The slope and offset of the cutoff and passband line fits as well as temperature were used as inputs to a multilinear regression. The topology of the neural net has five inputs, two hidden layers of seven and five nodes, and a single output. The network was trained with the Levenberg-Marquardt backpropagation algorithm [36]. One replicate from each of the batches was withheld for verification and another one for validation. This left only eighteen replicates or 57% of the data for training, which is lower than ideal. The correlation for the prediction of percent fat is shown in Fig. 71, with percent moisture in Fig. 72, and percent protein in Fig. 73. The r-squared values for each calibration are 0.99, 0.99, and 0.98 respectively.

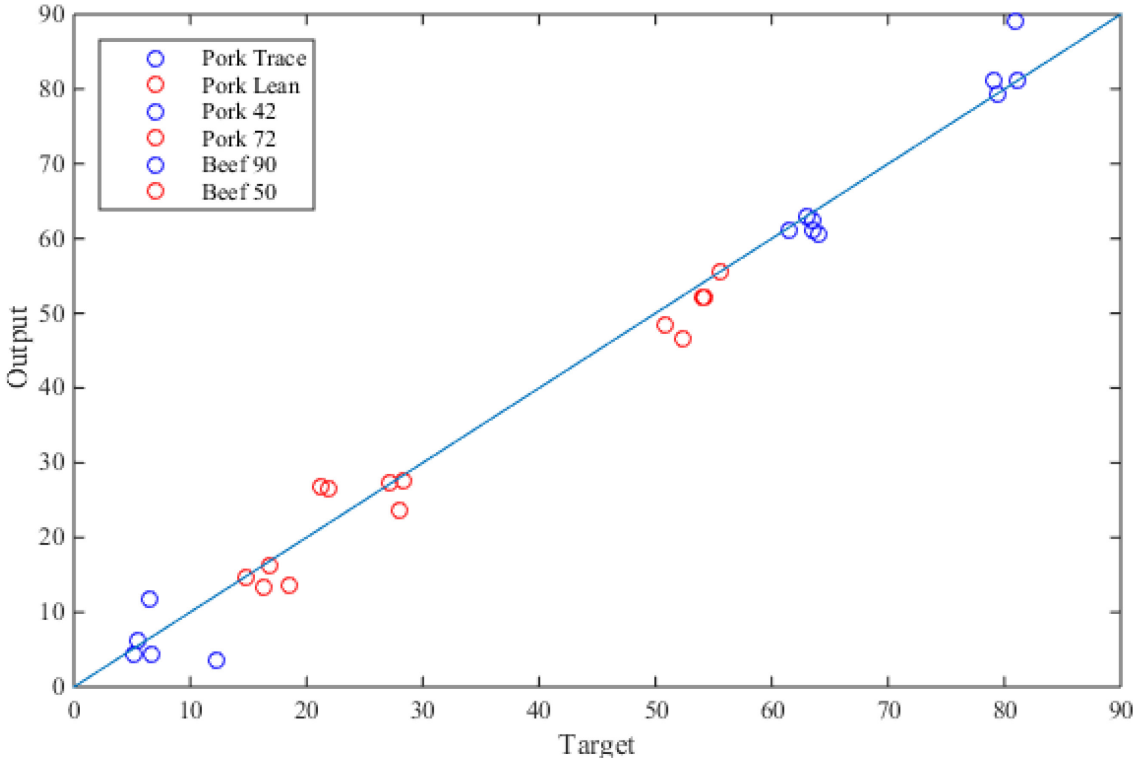

Fig. 71. Fat prediction using a neural network.

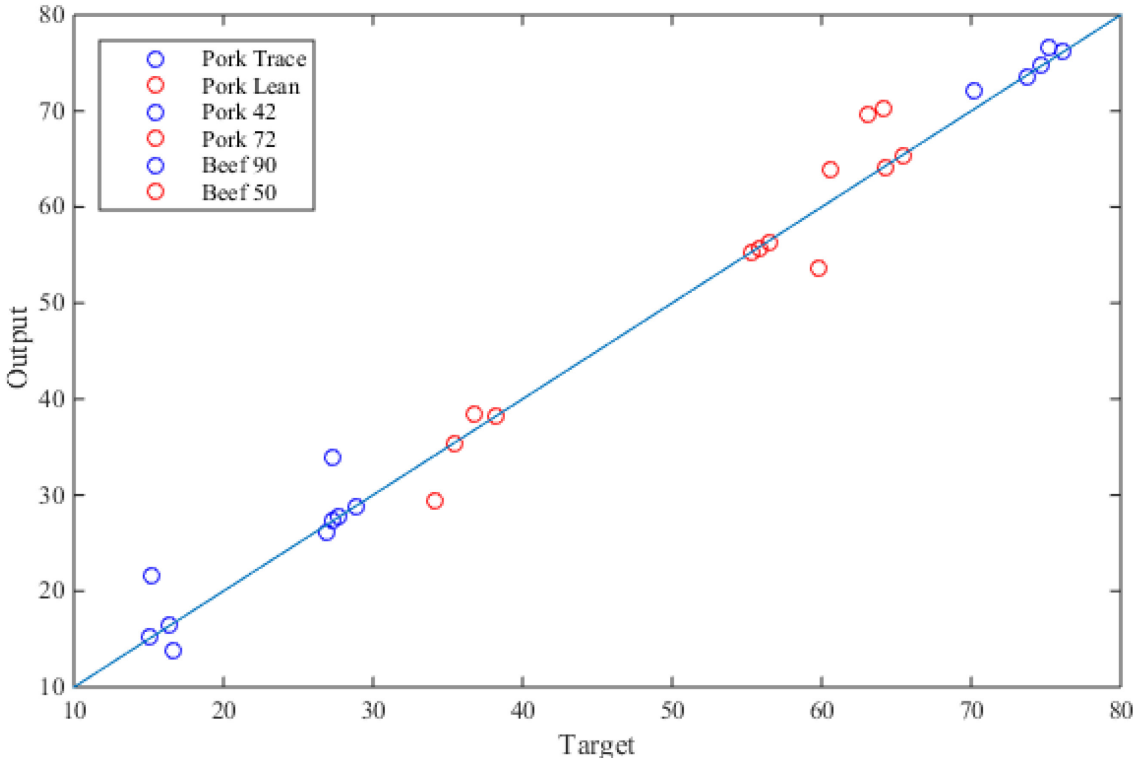

Fig. 72. Moisture prediction using a neural network.

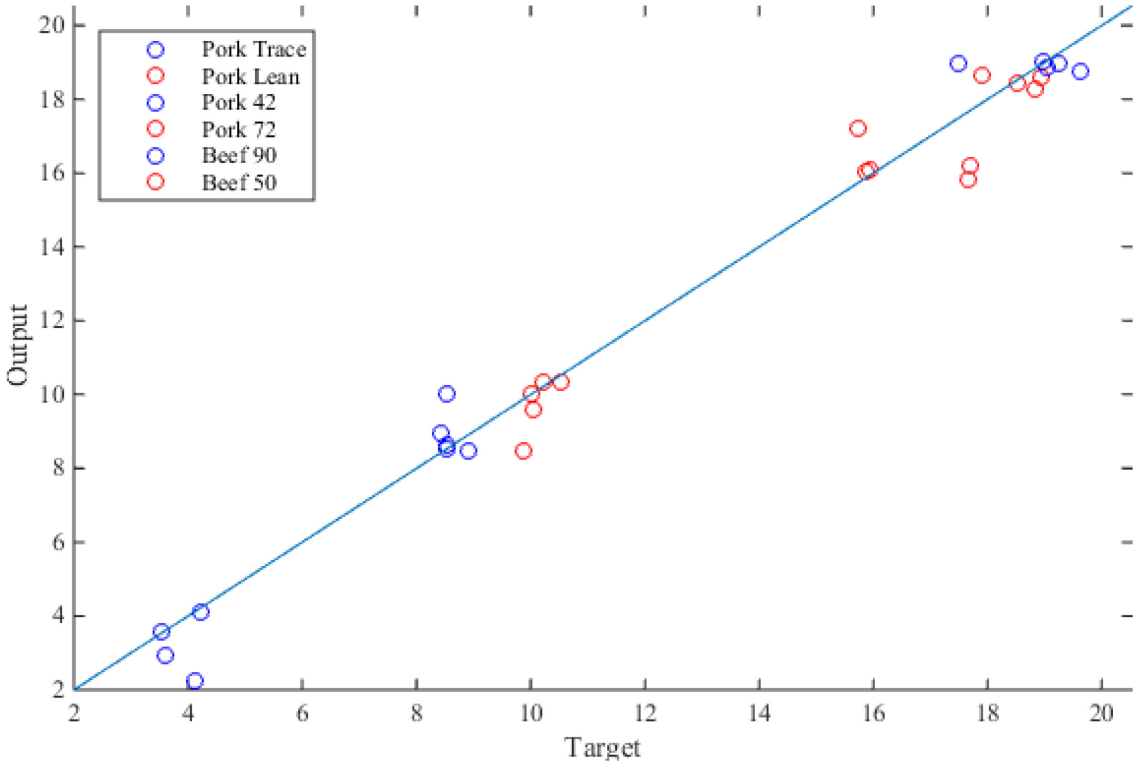

Fig. 73. Protein prediction using a neural network.

Table 5 provides the R2 and average error for percent fat, protein, and moisture of both the linear regression and the neural net. The neural net improved the average error by seventeen to thirty-two percent.

Table 5. R–squared values of the multi-linear regression and neural network.

Component	L.R. R^2	L.R. AVG Error	N.N. R^2	N.N AVG Error
Fat	0.9719	3.32 %	0.9915	2.57 %
Moisture	0.9709	2.65 %	0.9901	1.78 %
Protein	0.9703	0.74 %	0.9884	0.61 %

Further Work

Over the wide permittivity range, the linear regression offers adequate performance, but needs the accuracy increased to less than one percent. While the neural

network calibration improved the accuracy, the analysis was conducted on a limited set of data. The neural network needs to be thoroughly evaluated for stability before it can be used in a feedback control system.

Caloric Estimation

The development of a microwave sensor for caloric estimation is in joint collaboration with GE Global Research. GE's estimation algorithm requires percent fat and percent water in addition to weight. This can be accomplished with liquids through the waveguide cutoff analysis technique with a GMS system shown in Fig. 74 [37]. However, a system targeting consumers would have larger commercial success if the measurement could be made in open air without a waveguide.

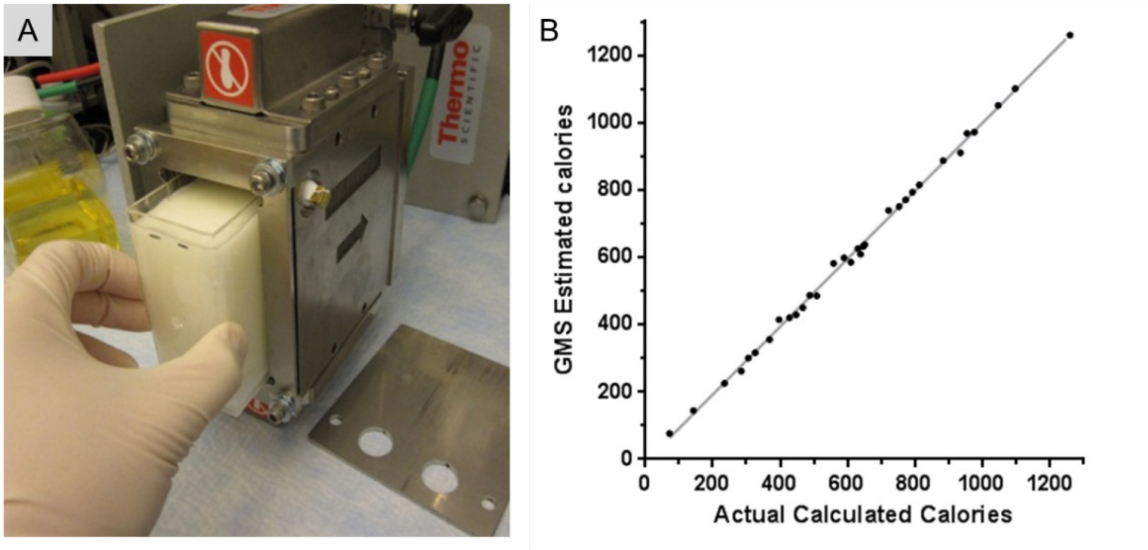

Fig. 74. Caloric estimation by GE using GMS.

Theory and Experimental Setup

An open air measurement system requires a different modality of measurement. Previous work, dubbed transit time tomography, used the time delay from UWB pulses

for image reconstruction in an open air system [38]. The time delay can be expressed mathematically as group velocity (20). There will be some dispersion as permittivity is not constant over frequency, but measuring the time delay can lead to an inferred permittivity measurement.

$$v_g = \frac{1}{\sqrt{\frac{\mu\varepsilon'}{2}\left[\sqrt{1+\left(\frac{\sigma}{\omega\varepsilon'}+\frac{\varepsilon''}{\varepsilon'}\right)^2}+1\right]}} \tag{20}$$

The test setup in Fig. 75 was constructed using three sheets of plastic with adjustable spacing between each [39]. Two antennas were mounted to the outer sheets while the material under test was placed on the middle sheet. The investigation was still limited to liquids in a fixed geometric structure, but introducing variable volume.

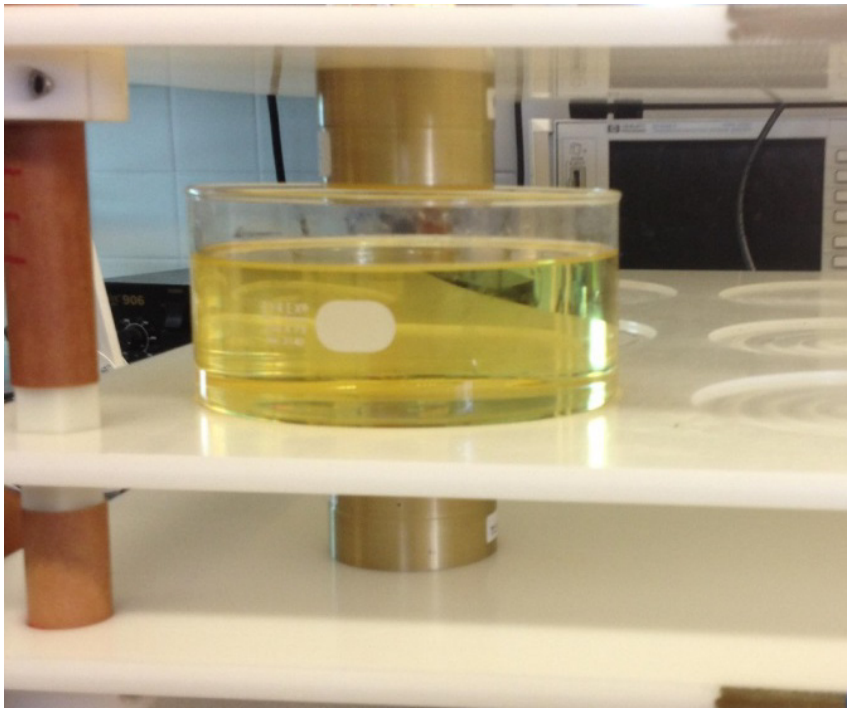

Fig. 75. Circular antenna test setup for caloric estimation.

Multiple antennas were also tested including circularly polarized spirals, horns, bowtie, planar bowtie, and optimized planar bowtie antennas. The following data was taken with the optimized planar bowtie antennas from Fig. 76.

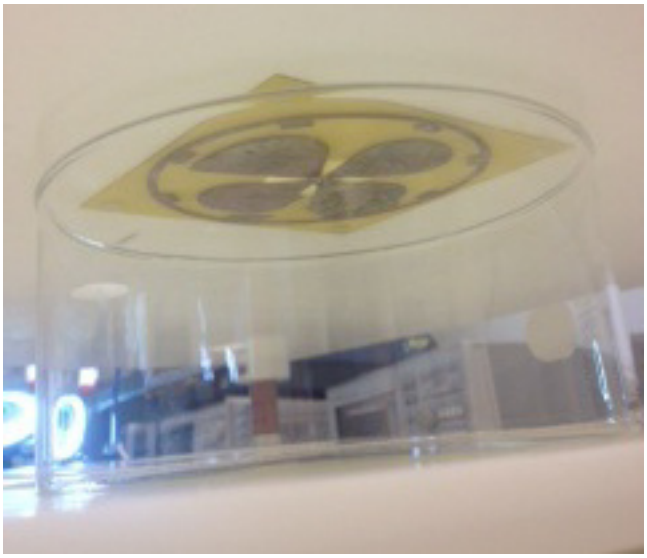

Fig. 76. Optimized planar bowtie antennas for caloric estimation.

Measurement Results and Analysis

The first experiment involved mixing water and vegetable oil at 0, 25, 50, 75, and 100 percent ratios while varying the volume from 20 mL to 850 mL in 10 mL increments. The frequency response of the test setup with an empty container was used as a calibration reference. This experiment involved the optimized bowtie antennas as close as possible to the cylindrical glass container, where the material under test is within the near field of the antenna. The liquid was stirred in between each measurement and a small amount of an emulsifying agent was used. Water temperatures were not recorded as it was assumed room temperatures would not vary by an influential amount.

Several metrics were identified which provided separation of the data: the mean, variance, skewness, and kurtosis for both amplitude and time, the time and amplitude of

the signal maximum, the slope of the phase, and the 3dB pulse width. The two most influential features are pulse delay and the slope of the phase. Fig. 77 shows the delay of pulses as from when the maximum occurs in time. An alternative calculation for the pulse delay is to use the phase information in the frequency domain. The derivative of the phase is group delay and the slope of a linear regression on that phase over the frequencies of interest, provides a better approximation of the group velocity for dispersive materials as each frequency has an equal weight regardless of its magnitude. The results of the slope are shown in Fig. 78 and illustrate much better linear correlation with increasing volume than the time domain approach. A source of error was found to be a focusing lens effect caused by the material under test at certain permittivities and dielectric depth.

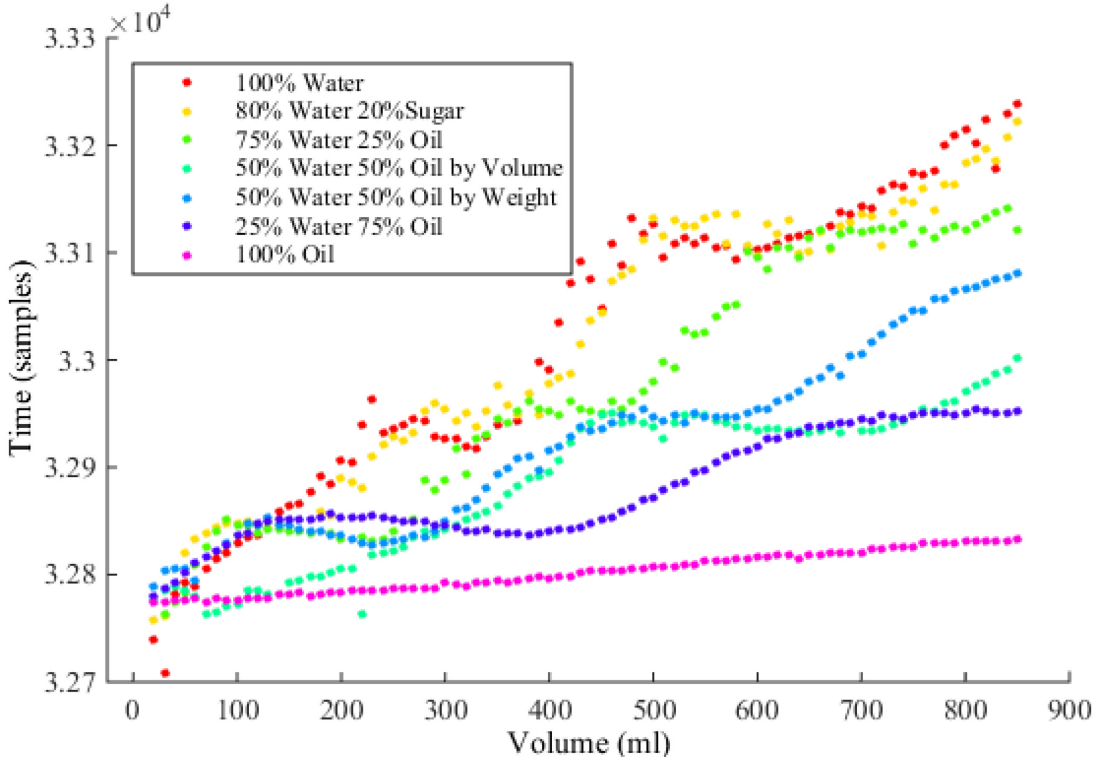

Fig. 77. Delay time of the pulse maximums for varying mixtures versus volume.

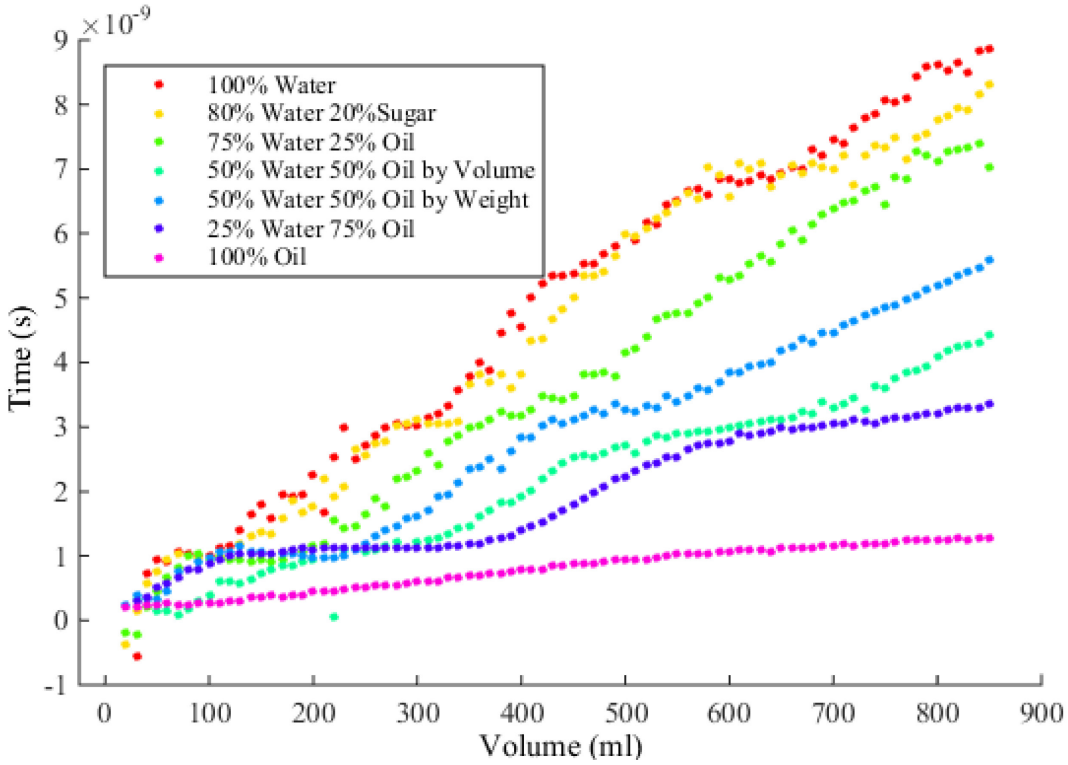

Fig. 78. Average group delay of the varying mixtures versus volume.

A single output feed forward neural network was used to perform a calibration on the data. The previously mentioned metrics were used as inputs to the neural net along with temperature and weight. Three hidden layers were used with thirteen, eight, and four nodes in each respective layer. Neural network training is accomplished with the Levenberg-Marquardt backpropagation algorithm [36]. The training algorithm used 15% of the data for validation and 15% of the data for verification. Two separate neural networks were trained, one for volume prediction and one for oil prediction. The results for the volume and oil prediction from each neural net are shown in Fig. 79 and Fig. 80. Their excellent correlation is summarized by Table 6 with r-squared values of 0.99 and average error under one percent.

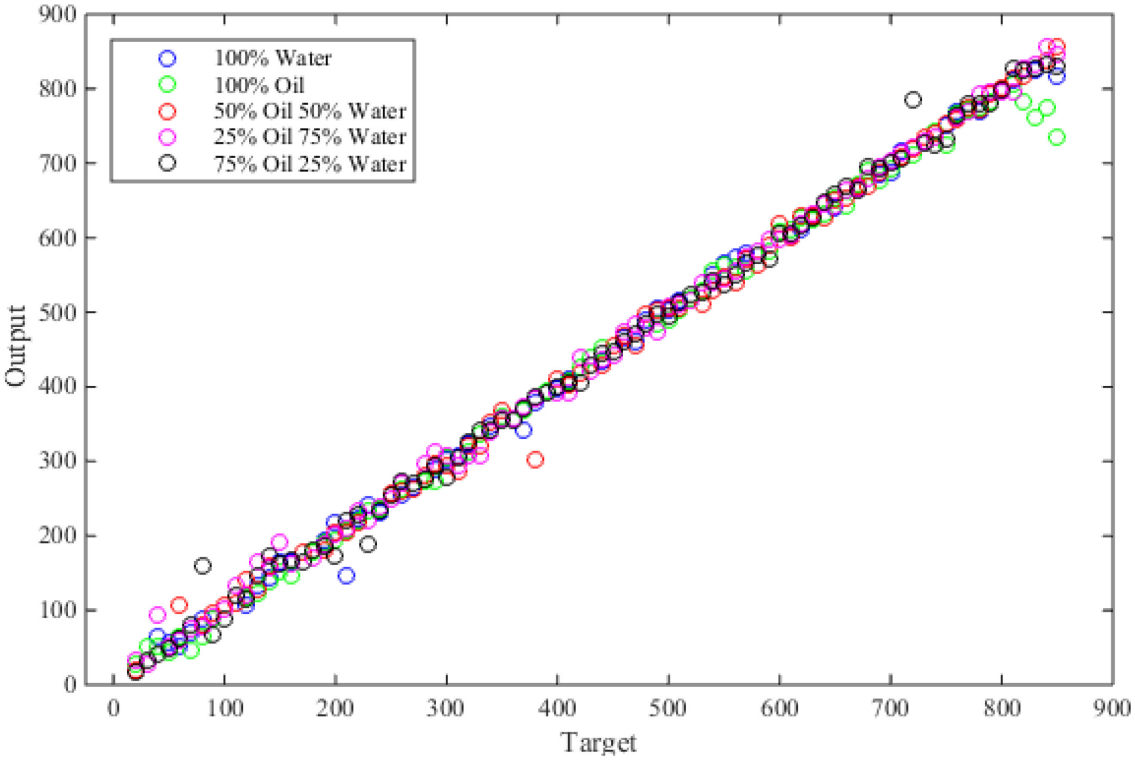

Fig. 79. Prediction of volume by a neural network on the various mixtures.

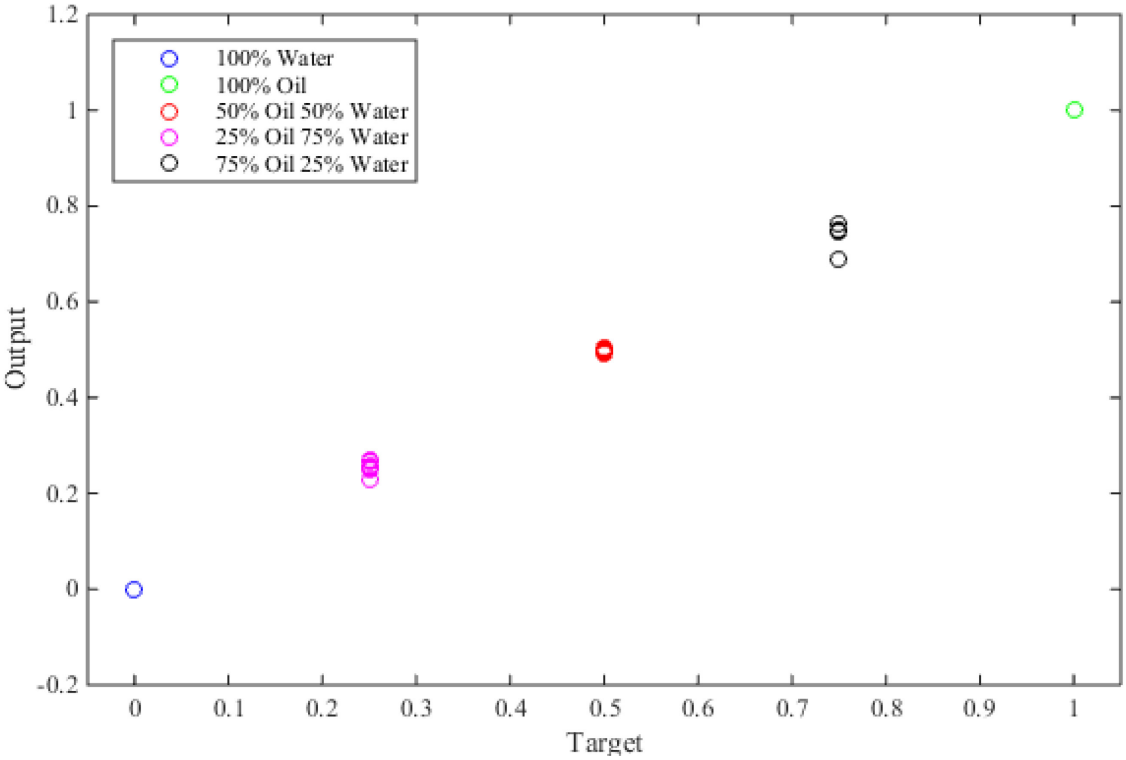

Fig. 80. Prediction of percent oil by neural network on the various mixtures.

Table 6. Neural net performance of volume and percent oil prediction.

Predictor	Max Error	Average Error	R-Squared
Volume	112.9 mL	8.42 mL	0.9965
Oil	5.96%	0.76%	0.9999

To further evaluate the system's ability to predict calories, mixtures were measured containing sugar, vegetable oil and water. The percent sugar and oil were varied in 5% increments from 0% to 30% to give a total of 49 sample points. Each of these samples was measured in two different weights, 550 grams and 1100 grams. Additionally salt and starch were used to individually and combined to perturb the samples. A few of the metrics were not used as inputs to the neural net to reduce the curse of dimensionality, but temperature and weight were added. Fig. 81 shows the correlation for caloric estimation.

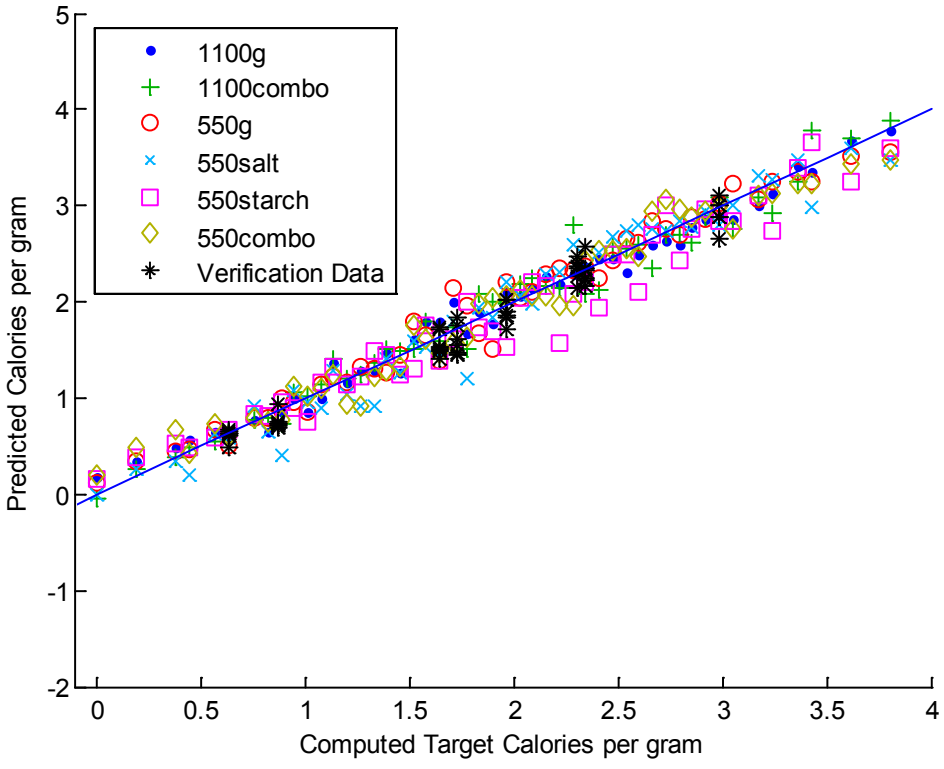

Fig. 81. Prediction of calories per gram by a neural network.

Further Work

Good performance has been demonstrated measuring liquid mixtures of differing volumes in an open air system with a fixed glass container. The next step is to measure liquids with solid inclusions as well as pure solids in a fixed container. Non-homogeneity must be investigated with layering of different materials. Once performance is achieved on consumer foods with uneven vertical distribution, radial distribution poses the last major challenge. A solution to this problem could involve tomographic reconstruction with an additional antenna lying in the radial plane. This solution would also require an additional coherent RF receiver or RF switch.

CHAPTER FIVE

Conclusions

The completed Pulse Dispersion Network Analyzer is shown in Fig. 82 mounted inside the Adalet XDHM explosion proof enclosure. This chapter contains a few performance comparisons with an Agilent E5071b network analyzer used for laboratory measurements, which carries an MSRP near $60,000. The system's costs are presented along with examples of its time and frequency domain resolution. A few strategies for improving the PDNA's performance are also offered along with final thoughts.

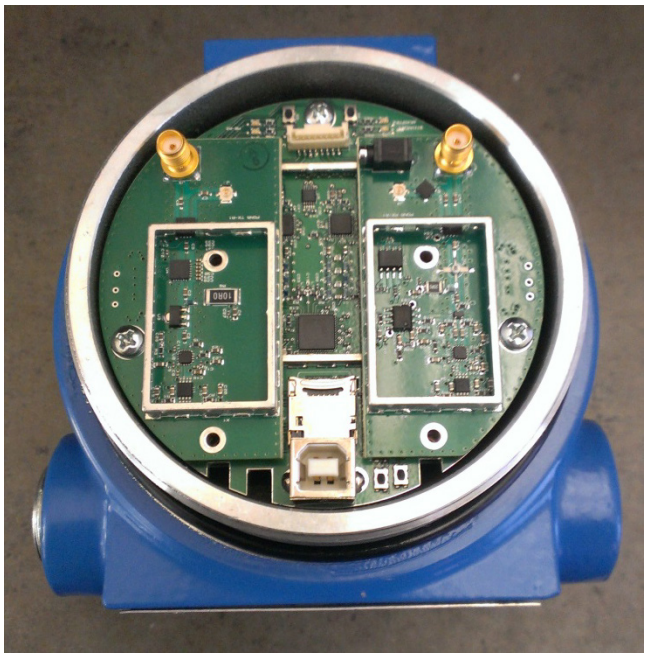

Fig. 82. The Pulse Dispersion Network Analyzer mounted inside the Adalet enclosure.

Performance and Accuracy

To evaluate system accuracy, the spectrums produced by the PDNA are compared to those of a VNA. Fig. 83 shows a spectrum comparison of water in a GMS rectangular

waveguide. Absolute correlation with the VNA is quite good out to 2.5 GHz with some inaccuracies beginning to appear at 2 GHz. A low pass filter was also measured and the spectral comparison is in Fig. 84. The low pass filter passband response is nearly perfect to the VNA and the PDNA's noise floor can be clearly seen at -50 dB.

For a time domain measurement, a material or structure with a narrow frequency response is the most difficult to capture. As the bandwidth decreases, the time domain signal lengthens, resulting in a much longer time of acquisition. A bandpass filter was measured with both the PDNA and VNA with the frequency magnitude displayed in Fig. 85. The time domain capture window for the PDNA was over 100ns, which results in a much longer acquisition time.

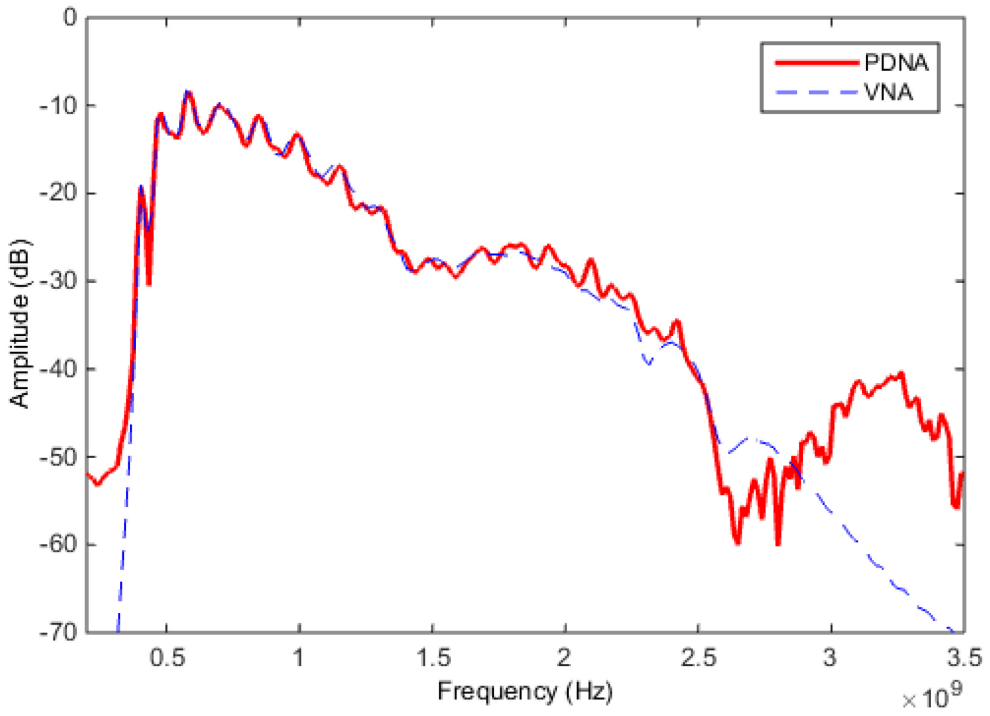

Fig. 83. Comparison of PDNA spectrum against a VNA for a water filled GMS waveguide.

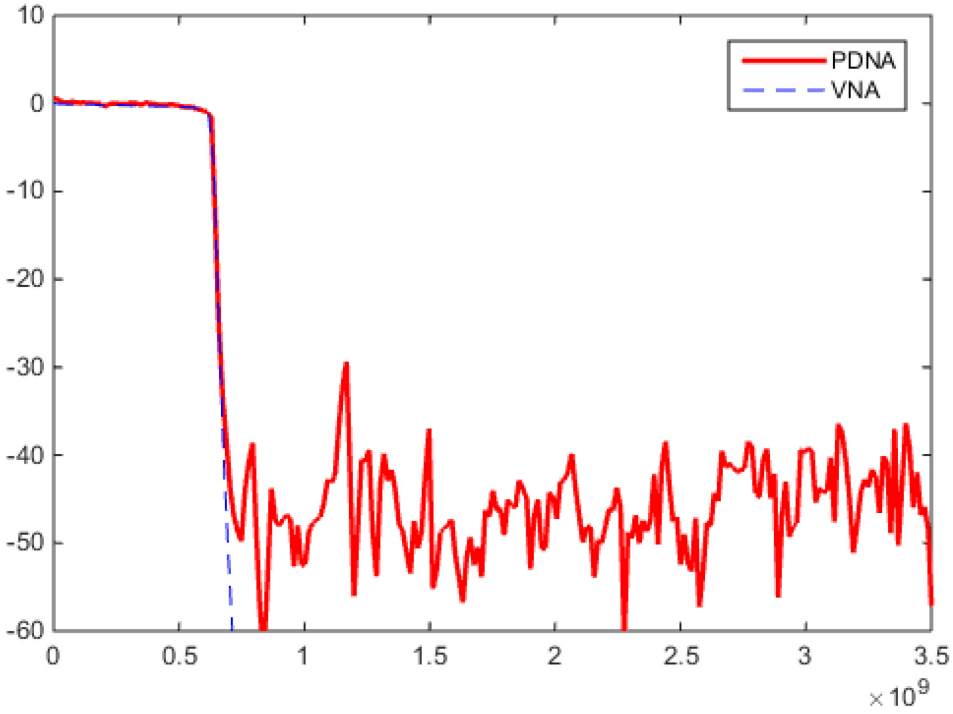

Fig. 84. Comparison of PDNA spectrum against a VNA for a low pass filter.

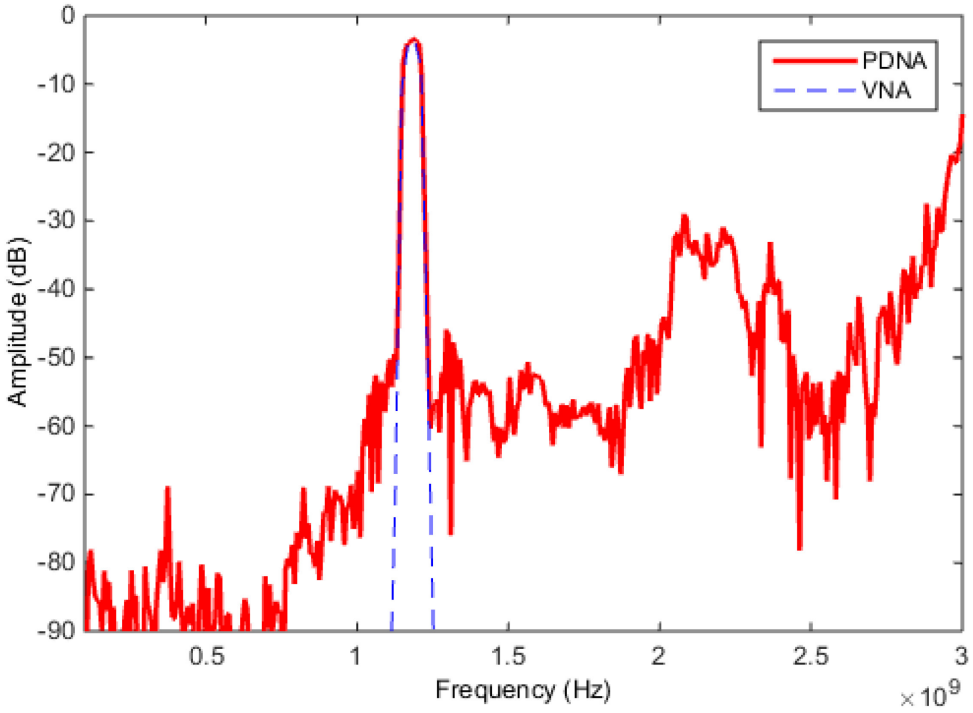

Fig. 85. Comparison of PDNA spectrum against a VNA for a bandpass filter.

Several different variable settings were used to illustrate the wide range of frequency and time domain resolutions achievable for the system. The performance is shown by Table 7. The first two rows target frequency resolution, while the second two rows target time domain resolution.

Table 7. Acquisition time of various time and frequency resolutionsc

Frequency Resolution	Time Resolution	Dispersion Window	Acquisition Time
0.8 MHz	40 ps	80 ns	95 ms
3 MHz	40 ps	80 ns	29 ms
15 MHz	4 ps	80 ns	94 ms
15 MHz	2 ps	80 ns	143 ms
15 MHz	2 ps	40 ns	94 ms

Table 8 shows the PDNA costs for the components when purchased from third party suppliers such as Digikey and Mouser. These costs do not include any extras to meet assembly kitting requirements. Also the enclosure was omitted since the enclosure will vary based on the application. For reference, the Adalet enclosure cost ranges from $230 to $155 with quantities of 1 to 50. Depending upon volume, manufacturing and assembly can constitute a large percentage of total costs. As an example, a small production of 10 units increased costs by 65% for manufacturing and 77% for assembly.

Table 8. PDNA component costs.

Unit Quantity	1	10	100
RF Transceiver	$130	$116	$92
Mainboard	$191	$170	$138
Powerboard	$112	$96	$75
PhyCore AM335x	$199	$199	$170
Total	$632	$581	$475

While the system architecture was developed for low cost, costs were secondary considerations for several portions of the design. Successful operation became

paramount leaving cost reduction for a second generation design. The clock generation circuit represents the largest cost of any subsystem in the PDNA, since clock jitter and frequency accuracy are designated as key parameters. The largest cost savings could be found in the power supply board, where relaxed specifications might not adversely affect operation. Minimal reductions could be made in the RF Transceiver, but would constitute the most expensive subsystem for reevaluation of design changes. Since a significant portion of development time was invested in the software, it is not recommended to change processors.

Continuing System Improvements

Several improvements to the USB communication can be made. The data rate could be increased by enabling the USB module to directly access the memory for the large spectrum data arrays. Also the continuously user displayed spectrum's could be sent using an isochronous transfer instead of a bulk transfer. Isochronous transfers have guaranteed bandwidth with higher priority than bulk transfers, but no guaranteed delivery. The real-time spectrums displayed to the user will be faster and less sporadic as they are not impacted as much by the bandwidth on the USB bus. The current bulk transfers are only guaranteed 20% of the high speed USB frame. Microsoft just added isochronous transfer support in their WinUSB driver with Windows 8.1. Note the WinUSB update was not included for Windows 7 greatly reducing compatibility.

The sub-sampling circuit in the RF Receiver has not been completely optimized. There are three passive component values for adjustments: two capacitors and one resistor. Conversion loss and 0.1 dB compression are two critical performance metrics,

which could be improved. The sub-sampling circuit contains a 50 Ω matching resistor, but the circuit's impedance has not been taken into account.

Final Thoughts

A low cost embedded vector network analyzer has been developed and evaluated for industrial processes. This Pulse Dispersion Network Analyzer fulfills the specifications required for several possible industrial applications. Sensors for the measurement of percent fat, moisture, and protein in ground meat; enthalpy of steam; caloric estimation; and water to cementitious ratio in fresh concrete were presented along with preliminary calibrations. While some of these applications require various amounts of further research, the microwave electronics and embedded software are ready for commercialization.

BIBLIOGRAPHY

[1] W. Jensen, C. Devine, and M. Dikeman, *Encyclopedia of Meat Sciences*. 2004.

[2] A. Leyzerovich, *Wet-steam Turbines for Nuclear Power Plants*. PennWell, 2005.

[3] Energy and Environmental Analysis, "Technology Characterization: Steam Turbines," Environmental Protection Agency, 2008.

[4] ASTM C143 / C143M-12, "Standard Test Method for Slump of Hydraulic-Cement Concrete," ASTM International, 2012.

[5] I. Soroka, *Concrete in Hot Environments*. London, UK: E & FN Spon, 2004.

[6] K. Basen-Engquist and M. Chang, "Obesity and Cancer Risk: Recent Review and Evidence," *Current Oncology Report*, vol. 13, pp. 71-76, Feb. 2011.

[7] D. B. Allison and M. Downey, "Obesity as a Disease: A White Paper on Evidence and Arguments Commissioned by the Council of The Obesity Society," *Obesity*, vol. 16, no. 6, pp. 1161-1177, Jun. 2008.

[8] J. Kruger, H. M. Blanck, and C. Gillepsie, "Dietary and physical activity behaviors among adults successful at weight loss maintenance," *Internation Journal of Behavioral Nutrition and Physical Activity*, vol. 3, Jul. 2006.

[9] J. M. Webster and V. B. Neculaes, "System and Method for Measuring Calorie Content of a Food Sample," U.S. Patent 2012/0053426, Mar. 1, 2012.

[10] L. Urban, "The Accuracy of Stated Energy Contents of Reduced-Energy, Commercially Prepared Foods," *Journal of the American Dietetic Association*, vol. 110, no. 1, pp. 116-123, Jan. 2010.

[11] J. D. Menczel and R. B. Prime, Eds., *Thermal Analysis of Polymers: Fundamentals and Applications*. United States of America: Wiley, 2009.

[12] A. Sihvola, "Mixing Rules with Complex Dielectric Coefficients," *Subsurface Sensing Technologies and Applications*, 2000.

[13] R. Birchak, G. Gardner, J. Hipp, and J. Victor, "High Dielectric Constant Microwave Probes for Sensing Soil Moisture," *Preceedings of the IEEE*, vol. 62, no. 1, pp. 93-98, Jan. 1974.

[14] H. Looyenga, "Dielectric constants of heterogeneous mixtures," *Physica*, vol. 31, pp. 401-406, 1965.

[15] F. T. Ulaby, R. K. Moore, and A. K. Fung, *Microwave Remote Sensing - Active and Passive*. Norwood, Massachusetts: Artech House, 1986.

[16] O. Levy and D. Stroud, "Maxwell Garnett theory for mixtures of anistropic inclusions: Application to conducting polymers," *Physical Review*, vol. 56, no. 13, pp. 8035-8046, Oct. 1997.

[17] F. Kremer and A. Schonhals, Eds., *Broadband Dielectric Spectroscopy*. New York: Springer, 2003.

[18] B. R. Jean, G. L. Waren, and F. L. Whitehead, "Meter and method for in situ measurement of the electromagnetic properties of various process materials using cutoff frequency characterization and analysis," US Patent 5455516, Oct. 3, 1995.

[19] D. M. Pozar, *Microwave Engineering*, 3rd ed. United States of America: John Wiley & Sons, 2005.

[20] B. R. Jean, "Process Composition Monitoring at Microwave Frequencies: A Waveguide Cutoff Method and Calibration Procedure," *IEEE Tranasctions on Instrumentation and Measurement*, vol. 55, no. 1, p. 180,186, Feb. 2006.

[21] C.-S. Lee and C.-L. Yang, "Complementary Split-Ring Resonators for Measuring Dielectric Constants and Loss Tangents," *IEEE MICROWAVE AND WIRELESS COMPONENTS LETTERS*, vol. 24, no. 8, pp. 563-565, Aug. 2014.

[22] J. D. Baena, "Equivalent-Circuit Models for Split-Ring Resonators and Complementary Split-Ring Resonators Coupled to Planar Transmission Lines," *IEEE TRANSACTIONS ON MICROWAVE THEORY AND TECHNIQUES*, vol. 53, no. 4, pp. 1451-1461, Apr. 2005.

[23] B. J. Herrera, "A Low-Cost Pulsed Fourier Transform Network Analyzer," M.S. thesis, Dept. E.C.E., Baylor University, TX, 2011.

[24] B. J. Herrera and B. R. Jean, "A low cost ultra-wideband pulse transceiver," in *42nd Southeastern Symposium on System Theory*, Tyler, TX, 2010, pp. 72-74.

[25] B. Herrera and B. R. Jean, "A tunable UWB pulse transceiver for microwave applied metrology applications," in *IEEE International Conference on Ultra-Wideband*, Syracuse, NY, 2012, pp. 324-327.

[26] C. Zhang, A. E. Fathy, and M. Mahouz, "Performance Enhancement of a Sub-Sampling Circuit for Ultra-Wideband Signal Processing," *IEEE Microwave and Wireless Components Letters*, vol. 17, no. 12, pp. 873-875, Dec. 2007.

[27] J. Han and C. Nguyen, "Coupled-slotline-hybrid sampling mixer integrated with step-recovery-diode pulse generator for UWB applications," *IEEE Transactions on Microwave Theory and Techniques*, vol. 53, no. 6, pp. 1875-1882, Jun. 2005.

[28] Analog Devices, "Low Jitter Sampling Clock Generator for High Performance ADCs," Circuit Note CN-0109.

[29] L. N. Trefethen and D. B. III, *Numerical Linear Algebra*. Philadelphia, United States of America: Society for Industrial and Applied Mathematics, 1997.

[30] W. S. Cleveland, "Robust Locally Weighted Regression and Smoothing Scatterplots," *Journal of the American Statistical Association*, vol. 74, no. 368, pp. 829-836, Dec. 1979.

[31] W. S. Cleveland and S. J. Devlin, "Locally Weighted Regression: An Approach to Regression Analysis by Local Fitting," *Journal of the American Statistical Association*, vol. 83, no. 403, pp. 596-610, Sep. 1988.

[32] F. W. J. D. Buford Jean, "Microwave Sensor Having Improved Sensitivity," U.S. Patent 6614238, Sep. 2, 2003.

[33] C. Faulkner, "An In-Line Microwave Steam Quality Sensor," M.S. thesis, Dept. E.C.E., Baylor University, 2014.

[34] S. H. Kosmatka, *Design and Control of Concrete Mxtures*. Portland Cement Association, 2011.

[35] U. M. Carthy, et al., "Permittivity of Meat Fish and their Components at UHF RFID Frequencies and Industry Relavant Temperatures," *Agricultural Engineering International: CIGR Journal*, vol. XI, Dec. 2009.

[36] D. W. Marquardt, "An Algorithm for Least-Squares Estimation on Nonlinear Parameters," *Journal of the Society for Industrial Applied Mathematics*, vol. 11, no. 2, pp. 431-441, Jun. 1963.

[37] B. R. J. V. B. N. S. K. J.M. Webster, "Enabling Automated Calorie Counting at the Touch of a Button," The 29th Annual Scientific Metting of the Obesity Society poster presentation, 2011.

[38] M. L. T. R. J. M. I. Buford Randall Jean, "A New Modality for Microwave Tomographic Imaging: Transit Time Tomography," *International Journal of Tomography & Statistics*, vol. 11, no. Winter, 2009.

[39] S. Gibbs, "Estimation of Multi-Component Mixture Proportions using Regression Machine Analysis of Ultra-Wideband Spectroscopic Measurements," in *IEEE International Conference on Ultra-Wideband*, 2013, pp. 66-71.